

ABSTRACT

SUI, NI. Sound-proof Sandwich Panel Design via Metamaterial Concept. (Under the direction of Dr. Fuh-Gwo Yuan and Dr. Yun Jing).

Sandwich panels consisting of hollow core cells and two face-sheets bonded on both sides have been widely used as lightweight and strong structures in practical engineering applications, but with poor acoustic performance especially at low frequency regime. Basic sound-proof methods for the sandwich panel design are spontaneously categorized as sound insulation and sound absorption. Motivated by metamaterial concept, this dissertation presents two sandwich panel designs without sacrificing weight or size penalty: A lightweight yet sound-proof honeycomb acoustic metamaterial can be used as core material for honeycomb sandwich panels to block sound and break the mass law to realize minimum sound transmission; the other sandwich panel design is based on coupled Helmholtz resonators and can achieve perfect sound absorption without sound reflection.

Based on the honeycomb sandwich panel, the mechanical properties of the honeycomb core structure were studied first. By incorporating a thin membrane on top of each honeycomb core, the traditional honeycomb core turns into honeycomb acoustic metamaterial. The basic theory for such kind of membrane-type acoustic metamaterial is demonstrated by a lumped model with infinite periodic oscillator system, and the negative dynamic effective mass density for clamped membrane is analyzed under the membrane resonance condition. Evanescent wave mode caused by negative dynamic effective mass density and impedance methods are utilized to interpret the physical phenomenon of

honeycomb acoustic metamaterials at resonance. The honeycomb metamaterials can extraordinarily improve low-frequency sound transmission loss below the first resonant frequency of the membrane. The property of the membrane, the tension of the membrane and the numbers of attached membranes can impact the sound transmission loss, which are observed by numerical simulations and validated by experiments. The sandwich panel which incorporates the honeycomb metamaterial as the core material maintains the mechanical property and yields a sound transmission loss that is consistently greater than 50 dB at low frequencies. Furthermore, the absorption property of the proposed honeycomb sandwich panel was experimentally studied. The honeycomb sandwich panel shows an excellent sound absorbing performance at high frequencies by using reinforced glass fiber without adding too much mass. The effect of the panel size and the stiffness of the grid-like frame effect of the honeycomb sandwich structures on sound transmission are discussed lastly.

For the second sound-proof sandwich panel design, each unit cell of the sandwich panel is replaced by a Helmholtz resonator by perforating a small hole on the top face sheet. A perfect sound absorber sandwich panel with coupled Helmholtz resonators is proposed by two types: single identical Helmholtz resonator in each unit cell and dual Helmholtz resonators with different orifices, arranged in each cell arranged periodically. The sound-proof sandwich panel is modelled as a panel embedded in rigid panel and assumed as a semi-infinite space with hard boundary condition. The net/mutual impedance model is first proposed and derived by solving Kirchhoff-Helmholtz integral by using the Green's function. The thermal-viscous energy dissipation at the thermal boundary layer dominates the total energy consumed.

Two types of perfect sound absorber sandwich panel are designed in the last part. Two theoretical methods: the average energy and the equivalent surface impedance method are used to predict sound absorption performance. The geometry for perfect sound absorber sandwich panel at a target frequency can be obtained when all the Helmholtz resonators are at resonance and the surface impedance of the sandwich panel matches the air impedance. The bandwidth for the identical sandwich panel mainly depends on the neck radius. The absorptive property of the dual Helmholtz resonators type of sandwich panel is studied by investigating the coupling effects between HRs. The theoretical results can be verified by numerical simulations through finite element method. The absorption bandwidth can be tuned by incorporating more HRs in each unit cell.

Both sound-proof sandwich panel designs possess extraordinary acoustic performance for noise reduction at low frequency range with sub-wavelength structures. The sound absorber panel design can also achieve broadband sound attenuation at low frequencies.

© Copyright 2017 Ni Sui

All Rights Reserved

Sound-proof Sandwich Panel Design via Metamaterial Concept

by
Ni Sui

A dissertation submitted to the Graduate Faculty of
North Carolina State University
in partial fulfillment of the
requirements for the degree of
Doctor of Philosophy

Mechanical Engineering

Raleigh, North Carolina

2017

APPROVED BY:

Dr. Fuh-Gwo Yuan
Co-Chair of Advisory Committee

Dr. Yunjing
Co-Chair of Advisory Committee

Dr. Larry Silverberg

Dr. Jingyan Dong

DEDICATION

To my dearest Husband, Xiang Yan,
my lovely daughter and son, Annie Yan and Aaron Yan
and my devoting parents and parents-in-law.

BIOGRAPHY

Ni Sui earned her bachelor's degree in automotive engineering at Jiangsu University in China in 2009. After graduation, she was directly admitted to continue her master's program without examination in automotive engineering in the same university and worked on noise control of a mini-electric car for three years. In 2012, she began her studies as a PhD student in Mechanical Engineering at North Carolina State University under Dr. Fuh-Gwo Yuan and Dr. Yun Jing. She conducted research on acoustic metamaterials, noise control, and acoustic sandwich panels.

ACKNOWLEDGMENTS

First and foremost, I would like to express my deepest gratitude to my advisor and committee chair, Dr. Fuh-Gwo Yuan, for the time and efforts that he spent on me in helping me pursuing my Ph.D. degree. His guidance, knowledge, patience, and enthusiastic encouragement have been an invaluable source of inspiration throughout my Ph.D. study. It is him who makes me understand there is no shortcut for research but hard working; It is him who gives me enough freedom so that I can step into new research directions; It is him who makes me realize exploring unknowns is key to research and the process for exploring is always important than the outcomes.

I also would like to express my sincere gratitude to my co-advisor Dr. Yun Jing for his continuous support and help for my Ph.D. study and research. He also gave me freedom to pursue different project and open my mind with new area for my research which helped me a lot to build my research ability and interest of exploring the unknowns. I can never have earned my doctoral degree without his patience and insightful discussions.

It is my great honor, fortune, and pleasure in having the opportunity working with Dr. Yuan and Dr. Jing to develop my research base and skills and independent research ability. Thank you all Dr. Yuan and Dr. Jing for their candid, pertinent, and beneficial suggestions on my career and life planning. They are not only an academic advisor, but also a mentor for life. They gave me lots of confidence and encouragement in my spare life to support for my family and my two kids. Thanks very much!

I would also like to thank all my other committee members, Dr. Larry Silverburg and Dr. Jingyan Dong, who have offered me superb classes, and invaluable suggestions for my

dissertation research explorations. Special thanks to Dr. Ying Luo and Dr. Zhongxing Li who were my graduate academic advisors when I was in Jiangsu University, China. It was their encouragement and continuous support so that I was able to pursue my Ph.D. degree in the states.

I would also like to thank all my current and former colleagues in the Smart Structures and Materials Lab and Acoustic lab for their help, invaluable suggestions, comments and discussions during my study. I would acknowledge these individuals as Dr. Chen Shen, Dr. Tarry Huang, Dr. Rui Zhu, Dr. Yuling Liu, Dr. Jiaze He, Dr. Sri Vikram Palagummi, Dr. Mohammad Harb, Mr. Chao Wan, Mr. Che-Yuan Chang, Mr. Ningyi Zhang, Mr. Ruiyu Fong, Mr. Dingjie Suo and Ms. Juanjuan Gu. Especially thanks to Dr. Shaorui Yang, who is always ready to answer me any theoretical questions on wave propagation in solid structures.

Finally, I would like to express my deep gratitude to my parents, parents-in-law, and my Husband, without their love and care, encouragements and supports I would not be able to pursue my Ph.D. degree. Especially, to my husband, Xiang! I love you so much! I cannot make such big progress with my research without you; I cannot balance well with my life without you; I cannot be a good mom with our children without you! I would also like to thank my five-year old daughter, Annie Yan, who is also accompanied me with my Ph.D. I would like to thank my little son Aaron Yan, who also inspires and supports me. Mommy loves you all! Last but not least, I would like to express all my gratitude to my mother, Liming Liang, who devoted all her time in taking care of my daughter and my son and travel back and forth between China and USA. Best wishes to my families and wish them healthy and happy every day. I can only try harder to reward you.

TABLE OF CONTENTS

LIST OF FIGURES	viii
Chapter 1	1
Introduction.....	1
1.1 Noise reduction methods for sandwich panels.....	4
1.1.1 Sound insulation method in sandwich panel design	4
1.1.2 Sound absorption method in sandwich panel design	7
1.2 Acoustic metamaterials for noise reduction.....	8
1.2.1 Membrane-type (plate-type) AMs with mass attached on for noise reduction.	12
1.2.2 Membrane-type AMs without mass attached on for noise reduction	15
1.2.3 Active AMs for noise reduction.....	17
1.3 Perfect sound absorber design in sub-wavelength range	18
1.3.1 Perfect sound absorber for noise control	18
1.3.2 Classic HRs based sound absorber	19
Chapter 2	22
Basic theory for the honeycomb acoustic metamaterial.....	22
2.1 Mechanical properties of honeycomb structures	24
2.2 Mechanism of low-frequency sound insulation – negative effective mass density..	32
2.2.1 The classic one dimensional mass-spring infinite periodic system model	32
2.2.2 The effective mass density and impedance match for a clamped membrane...	36
2.2.3 Negative-mass effect illustrated through wave propagative and evanescent modes	38
2.3 Sound reflection and transmission of the clamped membrane in a tube.....	40
2.4 Summary	43
Chapter 3	45
A lightweight yet sound-proof honeycomb acoustic metamaterial.....	45
3.1 Honeycomb acoustic metamaterial for low frequency noise reduction.....	46
3.2 Experimental study on honeycomb acoustic metamaterial using sound absorbing materials.....	63
3.3 Discussion.....	73

3.4	Summary	77
Chapter 4	78
The Helmholtz resonator in a semi-infinite panel	78
4.1	The single Helmholtz resonator in a semi-infinite rigid panel	80
4.2	Coupled dual Helmholtz resonators in a semi-infinite rigid panel	90
4.3	Summary	97
Chapter 5	99
Perfect sound absorption panel using periodic arranged Helmholtz resonators		99
5.1	Identical Helmholtz resonators in the panel.....	101
5.1.1	Absorption coefficient calculation-Energy Method.....	103
5.1.2	Absorption coefficient calculation-Surface Impedance Method	105
5.1.3	Perfect sound absorption for the sandwich panel	106
5.1.4	Finite element simulation for numerical analysis	115
5.2	Two different Helmholtz Resonators as a unit cell in the panel	118
5.2.1	Absorption coefficient calculation-Energy Method.....	121
5.2.2	Absorption coefficient calculation - Surface Impedance Method	122
5.2.3	Perfect absorption for sandwich panel.....	124
5.2.4	Finite element simulation for numerical analysis	131
5.3	Summary	140
Chapter 6	142
Conclusions and Future Work	142
6.1	Conclusions and Contributions beyond Previous Work.....	143
6.1.1	Coclusions.....	143
REFERENCES	146

LIST OF FIGURES

Figure 1.1 Honeycomb sandwich panels applied on airplane.....	4
Figure 2.1 Configuration of acoustic metamaterial applied in sandwich panel.....	24
Figure 2.2 A honeycomb with hexagonal cells.....	25
Figure 2.3 Honeycomb cell deformation under extension or compression: (a) the undeformed cell; (b) loading in x_1 direction; (c) loading in x_2 direction.....	28
Figure 2.4 The mechanical properties of the honeycomb are derived under the loading normal to x_3	29
Figure 2.5 Honeycomb with non-uniform thickness cell walls.	31
Figure 2.6 The unit oscillator with negative effective mass.	34
Figure 2.7 An infinite periodic mass-spring system.	35
Figure 2.8 The infinite mass-spring system and its unit.	36
Figure 2.9 A clamped membrane inside the tube.	40
Figure 3.1 Metamaterial prototype used for the acoustical test.....	47
Figure 3.2 (a) Unit cell of the honeycomb membrane-type metamaterial. (b) An equivalent composite composed of a linearly isotropic membrane and a homogenized, transversely orthotropic material for the calculation of effective Young's modulus of the metamaterial in in-plane and out-of-plane directions.	48
Figure 3.3 Experimental and simulation STL results for honeycomb core only and the proposed metamaterial (honeycomb core with membranes).	52
Figure 3.4 Effective dynamic mass density of the membrane AM as a function of frequency.	53

Figure 3.5 STL curves of two metamaterial samples with membrane thicknesses at $h_m = 0.25$ mm and $h_m = 0.2$ mm, respectively..... 56

Figure 3.6 The STL of two 0.2 mm thick membranes with one of the samples having pretension applied (approximately 5 N/m). 57

Figure 3.7 Comparison of the STL for the metamaterial sample with two membranes attached on the top and bottom surfaces of the honeycomb walls and the metamaterial sample with a single membrane. Each membrane had a thickness of $h_m = 0.25$ mm. 59

Figure 3.8 Comparison of the STL for a sandwich panel with membranes and a sandwich panel without membranes. The inset figure shows the structure of the sandwich panel with membranes. 61

Figure 3.9 Sketch of the metamaterial prototype (left). A photo of the prototype (right). 61

Figure 3.10 STL experimental results of the prototype. 63

Figure 3.11 Test sample is 29 mm in diameter: (a) Glass fiber is trimmed and inserted in the honeycomb core. (b) The configuration of honeycomb metamaterial with the glass fiber inserted. 64

Figure 3.12 STL test tube (four microphones)..... 65

Figure 3.13 SAC test tube (two microphones)..... 66

Figure 3.14 STL and SAC experimental results: (a) membrane; (b) glass fiber; (c) face sheets; (d) membrane and glass fiber; (e) membrane and face sheets; (f) glass fiber and face sheets; (g) membrane, glass fiber and face sheets. 70

Figure 3.15 STL experimental results of different component arrangements of the structure. 71

Figure 3.16 SAC experimental results of different component arrangements of the structure.	72
Figure 3.17 The STLs of the 10×10 panel with different Young’s modulus of frame (a) without damping case; (b) with damping case.....	74
Figure 3.18 The STLs of the 30×30 panel with different Young’s modulus of frame (a) without damping case; (b) with damping case.....	75
Figure 3.19 The STLs of the 50×50 panel with different Young’s modulus of frame (a) without damping case; (b) with damping case.....	75
Figure 3.20 The STL comparison of the 10×10 and 30×30 panel with different Young’s modulus of frame (a) $E_f=69000$ MPa; (b) $E_f=2000$ MPa; (c) $E_f=200$ MPa; (d) $E_f=20$ MPa.	76
Figure 4.1 Classic single Helmholtz resonator: (a) resonator sketch; (b) vibration analogy model.....	80
Figure 4.2 A single HR is embedded in the panel with plane wave incidence.....	81
Figure 4.3 One-dimensional vibration system analogy to the single HR on a rigid plane.	90
Figure 4.4 The coupled dual HRs embedded in the semi-infinite panel.....	91
Figure 5.1 The sandwich panel with periodically arranged identical HRs.	101
Figure 5.2 wave propagation of the perfect sound absorber sandwich panel with identical unit cells	107
Figure 5.3 (a) Geometrical parameters required for designing perfect sound absorber sandwich panel at different frequencies, (b) the bandwidth of as a function of neck radius, (c) cavity length as a function of neck radius, (d) neck length as a function of neck radius. The cavity radius is 30 mm.	109

Figure 5.4 (a) Geometrical parameters required for designing perfect sound absorber sandwich panel at different frequencies, (b) the bandwidth as a function of neck radius, (c) cavity length as a function of neck radius, (d) neck length as a function of neck radius. The cavity radius is 10 mm. 110

Figure 5.5 (a) Absorption spectrum of the proposed sound absorber sandwich panel, (b) resistive part of the sandwich panel, (c) reactive part of the sandwich panel with neck radius, neck length, cavity length and cavity radius to be 1.63 mm, 1.6 mm, 7.847 mm, and 30 mm, respectively. 114

Figure 5.6 (a) Absorption spectrum of the proposed sound absorber sandwich panel, (b) resistive part of the sandwich panel, (c) reactive part of the sandwich panel with neck radius, neck length, cavity length and cavity radius to be 1 mm, 7.218 mm, 12.21 mm, and 10 mm, respectively. 115

Figure 5.7 (a) Comparison of theoretical and numerical results of absorption coefficient spectrum, (b) comparison on resistance, (c) comparison on reactance. The neck radius, neck length, cavity length and cavity radius are 1 mm, 7.218 mm, 12.21 mm, and 10 mm, respectively. 117

Figure. 5.8 Energy conservation of the sound absorber panel. 118

Figure 5.9 the sandwich panel with periodically arranged dual HRs. 119

Figure 5.10 Wave propagation of the perfect sound absorber sandwich panel with dual HR as a unit cell..... 125

Figure 5.11 The absorption spectrum of the sandwich panel consisting periodical arrangement of dual HRs unit cells. The neck radius a_1 , neck lengths (l_1 and l_2) and the cavity length are selected as 1 mm, 3.5 mm, and 30 mm, respectively..... 127

Figure 5.12 Absorption coefficient with the variance of frequency and neck radius a_2 with the neck radius a_1 , neck length l and cavity length are 1mm, 3.5 mm, and 30 mm, respectively: (a) The cavity radius is 10 mm; (c) The cavity radius is 20 mm; (e) The cavity radius is 30 mm; (b), (d) and (f) The corresponding ‘half-absorption’ spectrum..... 128

Figure 5.13 Absorption spectrum with the variance of frequency and cavity radius a_c with the neck radius a_1 , neck length l and cavity length l_c are 1mm, 3.5 mm, and 30 mm, respectively: (a) The neck radius a_2 is 1 mm; (c) The neck radius a_2 is 1.2 mm; (e) The neck radius a_2 is 1.4 mm; (b), (d) and (f) The corresponding ‘half-absorption’ spectrum. 129

Figure 5.14 Absorption spectrum as a function of neck radius a_2 and cavity radius a_c : (a) 300 Hz; (b) 400 Hz; (c) 500 Hz; (d) 600 Hz..... 130

Figure 5.15 Absorption coefficient of the sandwich panel with different neck radius a_2 131

Figure 5.16 The perfect absorber sandwich panel I: (a) Absorption coefficient where $a_1=2.5$ mm, $a_2=2.85$ mm, $l=6$ mm, $l_{c1}=l_{c2}=40$ mm, $d=7$ mm, and the panel size is $l_x=44$ mm and $l_y=22$ mm; (b)The impedance with respect to the resistance and reactance (c) Energy balance verification 133

Figure 5.17 The perfect absorber sandwich panel II: (a) Absorption coefficient where $a_1=1$ mm, $a_2=1.38$ mm, $l=6$ mm, $l_{c1}=l_{c2}=10$ mm, $d=22$ mm, and the panel size is $l_x=44$ mm and $l_y=22$ mm; (b)The impedance with respect to the resistance and reactance (c) Energy balance verification 136

Figure 5.18 The perfect absorber sandwich panel III: (a) Absorption coefficient where $a_1=1.1$ mm, $a_2=1.2$ mm, $l=5$ mm, $l_{c1}=l_{c2}=30$ mm, $d=22$ mm, and the panel size is $l_x=44$ mm and $l_y=22$ mm; (b)The impedance with respect to the resistance and reactance (c) Energy balance verification 139

Chapter 1

Introduction

Lighter weight materials are always more desirable in real-world applications and therefore have been actively pursued in recent years ^{[1][2]}. One critical shortcoming of these materials, however, is their suboptimal acoustical performance: they allow sound to pass through rather easily and therefore yield a low sound transmission loss (STL). This phenomenon can be in part explained by the mass law, which states that the transmission of the noise through the material is inversely proportional to the product of the thickness, the density of the material and the frequency ^[3]. In other words, a lightweight material in theory translates to a high sound transmission (i.e., low STL), particularly at low frequencies. The optimal design of lightweight and high STL of the structure would therefore usually require design trade-offs.

Sound insulation by reducing sound transmission is one approach for noise control. On the other hand, sound absorption that takes in sound energy by reducing sound reflection is another sound-proof method. The proper absorbing materials/structures design requires the desirable sound absorption coefficient as a function of frequency of interest to fulfill the structure size or weight requirement with minimum cost. The sound energy is converted to heat due to friction induced by the motion of the sound particle and the sound absorbers. The sound absorber should be sizable enough to allow the incident acoustic energy dissipated inside the absorber before the sound wave reflecting back from the rigid end to the incident surface. Otherwise, the rest of the acoustic energy will transmit through the absorber. Therefore, it is challenging to design a sound absorber with a minimum thickness, especially at low frequency regime. In order to achieve perfect sound absorption at sub-wavelength

scale, the thickness of the sound absorber needs to be much less than one quarter of the wavelength to break to quarter wavelength limit.

Sandwich panels, which feature hollow cells (typically in hexagonal shape) formed between thin vertical walls and two high-modulus laminate sheets bonded on top and bottom sides have been widely used in constructing lightweight yet strong structures. The honeycomb sandwich panels, shown in Figure 1.1, with various actual applications such as aircrafts, satellite launch vehicles, navy joiner panels, fast-speed trains or buildings are well known to possess not only lightweight but high stiffness-to-weight ratio [4]-[8]. However, such panels are notorious for the poor acoustic performance at low frequencies due to their lightweight structures [9]. Blocking sound for such sandwich panel to improve the low-frequency sound transmission without using bulky, heavy treatment or strength sacrificing remains to be a big challenge. On the other side, sound absorbing panel should be sizable enough in order to dissipate sound energy into heat. For both designs, the properties of the sandwich panel must be maintained with minimum geometrical modifications. In this study, two sound-proof sandwich panels were designed and the major mechanisms can be categorized into two groups via metamaterial concept.

Inspired by recent development of no-mass-attached membrane-type acoustic metamaterials for low frequency sound blocking, a lightweight yet sound-proof honeycomb acoustic metamaterial was designed, theoretically studied and experimentally validated in the first part. By inserting a membrane inside honeycomb core, the sound transmission can be improved significantly in low frequency range with minimum weight-penalty. The honeycomb metamaterial can be used to build the core material of the sandwich structures

which are experimentally proven to be significantly more sound-proof. In the second part, a perfect sound absorbing panel with coupled Helmholtz resonators (HRs) was theoretically and numerically demonstrated. Each unit cell of sandwich panels can be used as a Helmholtz resonator by perforating a small hole on the top face sheet. The cavity of the HR is replaced by the panel core and the length of the orifice is determined by the thickness of the face sheet. The sound can be completely absorbed at a hybrid mode when two Helmholtz resonators coupled strongly with each other. Moreover, designing more Helmholtz resonators to create proper coupled hybrid modes can enable a broadband sound absorption.

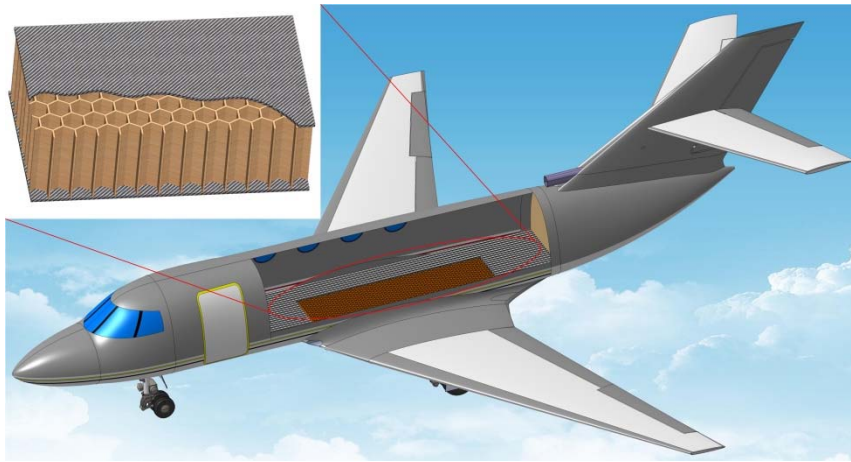


Figure 1.1 Honeycomb sandwich panels applied on airplane.

1.1 Noise reduction methods for sandwich panels

1.1.1 Sound insulation method in sandwich panel design

Acoustic optimization can be achieved by changing structural variables such as panel geometry, panel mass and elastic properties of materials. Acoustic optimization of sandwich structure is challenging and has been studied by a few researchers ^{[10]-[12]}, by considering core

and skin thickness, and core and skin material properties. Rajaram et al. ^[13] gave an overall study on the effects of different panel parameters, such as core density, core material, cell size, cell structures, skin modulus and skin density on the influence of sound transmission loss (STL) of honeycomb sandwich panels. STL was improved 4-5 dB at higher frequencies by reducing strength and increasing weight. Ruzzene ^[14] studied the vibration and sound radiation by proposing different layouts of honeycomb pattern. Denli and Sun ^[15] mainly focused on optimizing the shape change of cellular cores to minimize sound radiation. The radiated sound power varies with respect to the shape of unit cells, and narrowband noise reduction and broadband sound radiation can be achieved. However, such sandwich panel suffers from weight penalty and is constrained at its fundamental frequency. Ng et al. ^[16] ^[17] investigated the effect of stiffness and damping on the noise reduction of honeycomb sandwich panels. Huang ^[16] developed a fiber reinforced concrete panels as add-on honeycomb stiffened structure and used damping material to reduce noise. Ng designed a new sandwich panels using fiber reinforced plastic materials and developed new core fabrication techniques. Both of them got effective results to reduce the noise transmission below 500 Hz. However, such honeycomb sandwich panel designs require particular add-on materials and increase the panel mass. Therefore, the application and fabrication requirements hinders its practical application.

Noise insulation methods aiming at achieving noise reduction with minimum weight penalties were also traditionally employed by using porous materials ^[18]^[19], perforated media ^[20]^[21], or acoustic blankets with mass inclusions ^[22]^[23]. They have shown excellent performance in high frequency region but fail at low frequencies. Palumbo and Klos ^[24]

designed a reinforced/recessed panel with a 6 dB STL increase than the solid core panel while maintaining the strength requirement. They created areas in the honeycomb panel by adding voids and recesses to the core. However, the reinforced panels were 10% -15% greater than solid core panels. The configuration did not encompass the entire space, so it can only be used for particular application requirements. Kumar^[25] increased the loss factor for the honeycomb sandwich panels by adding a damping layer between the skin sheet and the honeycomb core. The sound insulation was improved at the critical frequency where the transmission is resonant when the damping treatment was applied.

To utilize the impedance mismatch between air and other gases, noise reduction is realized with weight penalty for honeycomb sandwich panels. Researchers ^{[26][27][28]} uses air and other gas to reduce transmitted noise by exploiting different acoustic impedance. Some studies ^{[29][30]} have shown that the application of a single gas layer is capable of reducing noise with helium or other gasses. This approach can be applied to sandwich panels by enclosing a gas layer on either side of the panel. Peters and Nutt ^[31] combined different honeycomb core materials, two skin materials and a mid-plane damping layer in Nomex core to examine the damping properties of the skin and mid-plane damping layer wave speed and core materials. The application for such design can be used as a lightweight acoustic insulation but the mechanical performance is bad. Naify et al. ^[32] focused on extending the impedance mismatch using different gasses to a sandwich panel. The sound transmits through multiple gas layers and the interfaces between gas layers increase the transmission loss due to impedance mismatches. as the STL is about 17 dB in mid-to-high frequency range (above 700 Hz) with 10 cm thick gas layers on either side of the panel. Although the

negligible mass of gas exhibits an promising application for lightweight panel structures, the gas layer introduced can increase the sound transmission loss at mid-to-high frequencies and mildly improve the low frequency range. Moreover, it is extremely difficult to build such lightweight panel with different gasses for practical applications, such as the gas storage, the geometric requirement, and cost of the sandwich panel.

Noise reduction of low-to-mid frequencies (50-1600Hz) has been studied by changing the geometrical or mechanical properties of the honeycomb sandwich panels without adding additional mass by Naify and Nutt^[33]. They inserted Nylon mesh septa into the honeycomb cells of the sandwich panels. The results showed 2 dB in STL improvement by using single septa and additional 2 dB in STL increase with double layers of septa.

1.1.2 Sound absorption method in sandwich panel design

Conventional porous materials e.g. foams, fibers and wools that rely on the viscous and thermal losses show excellent sound absorbing performance only at high frequencies. Since the low frequency absorption remains a big concern for porous materials and there are other drawbacks for the use of the porous materials in industry ^[34], the perforated or even microperforated panel (MMP) absorbers were developed several decades ago ^{[35][36][37]}. The MMP was first theoretically proposed by Maa ^{[38][39][40]}. The basic MMP absorber consists of a thin panel with sub-milimeter perforated holes laying in front of a rigid backing wall with an air gap cavity between them ^[41]. Numerous research works have been done to enhance the low frequency sound absorbing or broaden the bandwidth by adjoining new structure ^[42] or stacking MMP panels in parallel. Fan et al. ^[43] coated multi-layer membrane on perforated plates to achieve sound absorption below 500 Hz. Zhao and Fan ^[44] proposed a MMP backed

with mechanical impedance plates that has very good performance for sound absorption with adding total thickness of the structure. Gai et al.^[45] and Park ^[46] integrated Helmholtz resonators (HR) together with the MPP and improved the sound absorption of single layer MPP. MMP absorbers usually are very bulky compared with the wavelength and hard to perfectly match the impedance with the incident sound wave. However, as the honeycomb sandwich panel is the object of this study for noise control, optimal design of sound absorber honeycomb panels is another way to achieve the research goal. A micro-perforated honeycomb panel based on the theory of MMP has been studied by lots of researchers ^{[47]-[50]}. One of the face sheets can be replaced by the MMP and the other one is just treated like the back rigid panel resulting in the air cavity by the honeycomb core. The micro-perforated honeycomb panels can absorb low frequency sound without sacrificing the weight penalty and the high-stiffness property. However, the MMPs need to be doubled in order to achieve nearly perfect sound absorption ^[47]. Most MMPs are limp panel thus the MMPs need to be reinforced by some other materials ^[49]. The thickness of the honeycomb panel is almost 1/8 of wavelength or thicker if the design frequency is below 750 Hz ^[50]. Most recently, Tang et al. ^[51] proposed a hybrid acoustic metamaterial with broadband absorption in low frequencies, manipulating by a lightweight sandwich plate with perforated honeycomb-corrugation hybrid core. The face sheets can be used as MMP and rigid backing panel. The corrugation inserted inside honeycomb core with perforations served as MMP. This new kind of acoustic metamaterial exhibits promising engineering applications. But the corrugation core can induce the complexity for fabrications and will add additional weight.

1.2 Acoustic metamaterials for noise reduction

Metamaterials are artificial structures that made of sub-wavelength units and the material properties can't be obtained in nature. When the effective medium is used, the metamaterials are required to have unit cells much smaller than the wavelength. The most forward steps in metamaterial's field were derived from the electromagnetic area. Base on Maxwell's equations for electromagnetic wave ^[52], the electromagnetic (EM) metamaterial design requires negative values for electric permittivity ϵ and magnetic permeability μ . Veselago demonstrated the EM metamaterial for the first time in 1967 that the negative permittivity exhibited in certain frequencies. However this is not the case for permeability ^[53]. Pendry et al. ^{[54][55]} developed a wire structure with negative permittivity and split ring resonator with a negative permeability. Later on, Smith et al. ^[56] successfully combined the two structures and realized an EM metamaterial with negative index of refraction.

The implementation to develop EM metamaterials that have the material properties impossible to be obtained from nature brings the interest for a new material: acoustic metamaterials (AMs). Compared to the EM metamaterials, intensive theoretical and experimental studies have been devoted to design structures with negative values of bulk modulus and mass density. In 2000, locally resonant sonic materials were first proposed and exhibited as AMs by Liu et al.^[57] They demonstrated that a slab of material with embedded soft-coated lead balls acting as resonators in audible low frequency ranges. The dynamic mass density with a negative or extremely large value breaks the mass law to achieve a low transmission loss at 400 Hz with one or two magnitude smaller than corresponding wavelength. Two contrasting arrangements of resonators were studied: randomly dispersed resonators ^[58] and a periodic lattice arrangement of resonators ^[59]. These sonic crystals could

effectively block sound transmission due to the action of negative effective mass density in low frequency range. By using a spring-mass-damper model, Kin et al. [60] experimentally observed characteristics in the sound transmission loss. The STL experiment was conducted using a standing wave tube. The high STL at certain frequencies was observed that the peak STL occurred at an anti-resonant frequency and between two resonance frequencies of the structure.

Researchers have been studied this engineered materials with negative or near zero value of effective density and/or negative bulk modulus for couples of years [61]-[64]. Various applications for such AMs have been included : the acoustic superlens for imaging [65], the acoustic magnifying hyperlens [66], acoustic cloaking using near-zero index phononic crystal [67], sound attenuation at high frequencies by negative bulk modulus[68], energy tunneling [69], angular filtering [70] and acoustic attenuation panels [71] with higher transmission loss and lighter weight than conventional noise reduction methods especially in low-to-medium frequency range. The two critical material properties describing acoustic wave are density ρ and bulk modulus B . The acoustic wave equation and sound pressure in homogeneous medium are given as:

$$\nabla^2 p - \frac{\rho}{B} \frac{\partial^2 p}{\partial t^2} = 0 \quad (1.5)$$

$$p = P_0 e^{i(kx - \omega t)} \quad (1.6)$$

where P_0 is the amplitude of sound pressure, k is the wave number. The acoustic wave velocity c , which is defined as $\sqrt{B/\rho}$, will be imaginary when either density or bulk

modulus becomes negative. From $k=\omega/c$, the wave number also becomes imaginary and can be written as

$$k = \omega \sqrt{\frac{\rho}{B}} = ik_0 \quad (1.7)$$

where k_0 is a scalar number of wave vector. The Eq. (6) can be written as

$$p = P_0 e^{-k_0 x} e^{-i\omega t} \quad (1.8)$$

Therefore the acoustic wave will exponentially decay and become evanescent wave. The sound can eventually be attenuated when it transmits through the AMs with negative value of density and bulk modulus especially in low frequencies. The size of each unit cell of AMs is required to be sufficiently smaller than the wavelength in certain homogeneous mediums (typically about ten times smaller).^[72] Compared with the locally resonant structures, the non-resonant units may exhibit extreme material properties since they have wider bandwidth of frequency of interest for noise reduction.

Extensive efforts have been made to develop AMs as novel materials nowadays. Negative bulk modulus has been explicitly studied by Fang et al.^[73] using an array of Helmholtz resonators. These materials had a negative effective dynamic modulus near the resonant frequency. The structure consisted of a cavity of volume with rigid walls and a small hole in on side. A pressure variation caused the fluid in the hole to oscillate in and out acting like an inductor-capacitor circuit. Lee et al.^[74] developed a one dimensional tube AM with an array of side holes that exhibited a negative effective modulus in low frequencies from 0 to 450 Hz.

The appearance of AMs opened up the possibility to achieve excellent noise reduction particularly at low frequencies with minimum weight sacrifice. Compared with other types of AMs, membrane-type (or plate-type) acoustic metamaterials are tremendously preferred. Because membrane-type AMs have relatively simple geometries to achieve the lightweight structures and the negative effective density can be obtained by the resonance of each unit cell. Most importantly they are able to reduce to broadband noise reduction by tuning their unit cells if properly designed. Thus, the membrane-type AMs attract much attention for researchers to develop their mechanism and applications. There are three types of membrane-typed AMs for noise reduction: the membrane with mass attached on, the membrane with no mass attached on and active AMs that can actively tune the resonant frequency or other parameter.

1.2.1 Membrane-type (plate-type) AMs with mass attached on for noise reduction

The first membrane-type AM for low frequency noise insulation was proposed by Yang et al. ^[75]. By attaching a small mass onto the membrane with clamped boundaries, a narrow-band negative dynamic effective mass was tuned located between the first two resonance frequencies which resulted in near-zero total reflection, therefore breaking the mass law. The dynamic effective negative density occurred at the dip in sound transmission curve where it showed the anti-resonant frequency. The average displacement was minimum so that it gave the low transmission. The transmission curve can be tailored by tuning the attached mass on the membrane. Noise reduction in broad-band can be simply achieved by stacking up several membrane panels ^[76] and the total mass per unit area was only around 15 kg/m². An average sound transmission loss is over 40 dB in 50-1000Hz frequency range. Naify et al. ^{[77]-[80]}

theoretically and experimental elaborated the membrane-type AMs with mass attached on to achieve a lightweight structures for sound attenuation. The STL can be tuned by the weight of the mass on the membrane and the tension of membrane. They further presented the scale-up effect by arranging multiple elements in arrays and the frame compliance effect. The multiple configuration with different mass distributed on each membrane cell resulted in a multipeak STL profile. And the rigidity of the frame can weakened the ST if more and more unit cells are introduced. Later on, they changed the centered attached masses to coaxial rings, which broadened the bandwidth of the STL peaks or increased the multiple STL peaks. They finally predicted the STL by stacking the AMs and multi-celled arrays. Zhang et al. ^{[81][82]} developed the membrane-type AMs carrying different masses at adjacent cells. The STL was improved compared with the same structures but carrying identical masses at each cell. They also analyzed that the mass magnitude had more influence on the first TL dip and peak frequency, while the second TL dip frequency was strongly dominated by the membrane properties. The position of the mass on each unit cell didn't significantly impact the frequency range. Tian et al. ^[83] also adapted the membrane-center-mass configuration for their locally resonant acoustic metamaterial design. Increasing the inner radius of the circular membrane-ring or decreasing the weight of the ring can increase the resonance frequencies

Most recently, Chen et al. ^[84] and Langfeldt et al. ^[85] developed membrane-type AMs composed of a pre-stretched elastic membrane attached multiple rigid masses with arbitrary shape. The former investigated the effect such as weight, size, and eccentricity of the attached mass, pretension and thickness of the membrane on transmission peak and dip frequencies. They also analyzed the microstructure effects including the attached masses, the

depth, thickness, and loss factor of the membrane on sound absorption peak values ^[86]. The later employed the concept of the effective surface mass density to calculate the low-frequency STL by eigenvalue method. Ma et al. ^[87] presented a flexible lightweight membrane-type AM that obtain a full band gap below 500 Hz and even an ultra-low-frequency bending wave band gap below 100 Hz. The shapes of the mass block played an important role for affecting band structures. Ma et al. ^[88] exploited a membrane-type AM composing four membranes with fixed on disk masses under fully clamped boundary condition. There is a sizable orifice at the center so that air can flow freely through the AM. The interaction of the resonating membrane-type AM with the sound wave passing through the orifice results in a narrow-band low-frequency STL. Their design allows the air flow through the device, which breaks the utility limitations: air ventilation, heat exchange and weight reduction of a panel.

Lots of researchers developed membrane-type AMs with mass as sound absorbers since the mass on the vibrating membrane increase the damping and the sound energy can be dissipated by the membrane. Mei et al. ^[89] applied asymmetric rigid platelets on the membrane aiming to totally absorption at low frequencies from 100-1000 Hz resonance range. They also name it dark AMs since the 100% absorption. The acoustic energy can be converted into elastic energy by flapping the platelets and the energy totally dissipated by the membrane. The resonant frequency inhibits the peak absorption and can be tuned by adjusting the weight of the platelets and varying the distance between the asymmetric semi-circular platelets. Increasing the weight of the platelets or decreasing the distance between the platelets can absorb sound at even lower frequencies. Yang et al. ^[90]^[91] worked on sound

absorption in low frequencies by using elastic membrane with small rigid platelets fixed on top. The average amplitude of incoming sound wave pressure over the membrane area must be equal to the outgoing waves if the thickness of the membrane can be negligible. Thus, the maximum absorption can achieve 50% for one-side incidence and 100% with a back-reflecting surface. They experimentally realized the perfect sound absorption using the decorated membrane resonators. Ma et al ^[92] developed a metasurface for super-absorption at certain frequencies. This AM is composed of an ultrathin circular membrane with a centered platelet attached on and the membrane is fixed on a rigid circular frame in which there is filled with gas. This full absorption results from the impedance match with the air at certain frequencies due to hybrid resonances. The application of this metasurface can be set with magnet wires and magnet to obtain 23% conversion efficiency from acoustic energy to electrical energy.

Unlike membrane-type AMs which mainly manipulate the transmission, reflection, and absorption of acoustic waves, plates with attached masses could control either acoustic waves or elastic waves propagating within the plates (e.g., flexural and lamb waves) ^[93]. The configuration of plate-type AMs are mainly composed of a periodic arrangement of composite stubs deposited on a plate. They can prohibit low frequency structure-borne sound at their resonance frequencies ^{[94]-[100]}. The mechanism for negative effective material parameters induced by the resonant effect have been studied: negative effective mass density^{[101][102][103]} and negative values of mass density and bulk modulus ^{[104][105]}.

1.2.2 Membrane-type AMs without mass attached on for noise reduction

Shortly after, other researchers showed that no-mass-attached membranes or plates clamped at boundaries could also introduce high STL at low frequencies. Liu et al. ^[106] investigated an acoustic dual filter which can produce two sound transmission peaks and a sound blocking below 3000 Hz. The two peaks are the resonant vibrations of two membrane-air and metal-elastomer systems. Importantly, two transmission peaks can be controlled independently. Mahesh and Nair ^[107] designed an acoustic demultiplexer that is reconfigured into an array of semi-flexi-walled membrane-based Helmholtz resonators to compose a 4 port device. The stop band is attributed to the reflective negative bulk modulus and the frequency and bandwidth can be tuned by changing the sub-wavelength periodicity of the unit cells and the tension of the membrane. Fan et al. ^[108] demonstrated an AM composed of multi-layer membrane-coated perforated plates that can achieve a low frequency sound attenuation below 500 Hz even covering the lower audio frequency limit, 20 Hz. Csulyuszka et al. ^[109] created a novel resonant unit cell of one-dimensional AM that exhibits negative effective mass density. The acoustic unit cell is a thin elastic membrane placed in a short tube coaxial with an acoustic duct. This design is particular applied for acoustic superlensing and cloaking. Varanasi et al. ^[110] proposed that a panel consisting of an array of cellular unit structures can possess a high STL with a specified low frequency range without an undue mass penalty. This cellular AM can yield enhanced STL if the unit cell mass is apportioned appropriately between the unit cell plate and the surrounding grid-like frame. Varying the material and geometry parameters, the panel was treated from a heavy and stiff cell wall which significantly increased STL in low frequency range to a homogeneous solid of equal area mass in the form of a limp panel. Yao et al. ^[111] theoretically and experimentally

illustrated the negative mass phenomena occurring below a cut-off frequency. The model is derived from a mass-spring structure and the transmission dip is induced by negative effective mass. They further investigated a rectangular solid waveguide with clamped boundary conditions and analyzed that the dispersion relation confirm the band gap effect below the cut-off frequency related to the negative effective mass. This is experimentally verified by designing the steel grid and rubber panel. Lee et al. ^[71] used one-dimensional AM composed of an array of thin membranes to achieve negative density below 735 Hz. Although the no-mass-attached AMs could be potentially lighter in weight, the mass-attached, the locally resonant membrane-type AMs are the ones that have been predominately investigated by researchers.

1.2.3 Active AMs for noise reduction

Since active AMs are kind of passive metamaterials that actively tune their specific parameters to achieve the desired function such as the resonant frequency, inducing the electric circuit with piezoelectric is prevalent to control the properties of the AMs ^{[112][113][114]}. The electrical circuit with piezoelectric transducers can be applied in order to match the acoustic impedance as the incident sound wave reached the structure to reduce the noise. The acoustic energy can be transferred to the electrical energy so that the noise can be shielded. Pavel et al. ^[115] designed an active AM with a curved glass plate on which the electrical circuit was amounted. When the incident acoustic wave hit the glass plate, a part of the wave was reflected, which made the glass plate vibrate. The actuators were adjusted to suppress the vibration amplitude of the vibration mode of the frequency. As a result, the noise shielding efficiency can be enhanced by 3dB – 6dB in a narrow frequency range. Zhang et al. ^[116]

attached shunted piezoelectric patches on both sides of a thin plate. The higher STL given by this active plate-type AM compared with un-shunted case can be broadened by negative capacitance shunting circuits.

1.3 Perfect sound absorber design in sub-wavelength range

1.3.1 Perfect sound absorber for noise control

During the last decade, more advanced materials or structures were developed to magnify low frequency sound absorption in sub-wavelength range. The membrane-typed acoustic metamaterial as illustrated above is one of the success approaches resulting in perfect sound absorption at low frequencies ^[84]. Another resonating membrane absorber with sub-wavelength dimension was proposed by Yang et al^[117]. Perfect sound absorption was achieved by combining a pair of degenerate monopole and dipole resonators. The sound absorption can be enhanced by embedding HRs in porous materials ^{[118][119]}. The viscous and thermal losses of porous materials coupling with resonance absorption mechanism exhibited high absorption coefficient. The induced HR with tuned neck lengths can enlarge the amplitude and the bandwidth of the absorption coefficient under a range of frequencies. Enlightened by electromagnetic principles, the concept of coherent perfect absorption (CPA) was first proposed in optical domain by Chong et al. ^[120] Wei et al. ^[121] extended CPA mechanism into the acoustic domain by designing acoustic metamaterial structures with resonating effective bulk modulus or density and the complete absorption was achieved in the forward and backward input directions. Similarly, Merkel et al. ^[122] developed a kind CPA with two indirect coupled HRs which were used to tune the inherent losses. A perfect sound absorption can be obtained by matching the system impedance with the impedance of

background medium perfectly. The deep-subwavelength coplanar HR based sound absorber [123] and acoustic metasurface-based perfect absorber [124] are two examples for the impedance match concept. The coplanar spiral tubes formed coiled cavities that acted as Helmholtz resonating chambers to reduce the thickness of the panel. The metasurface-based perfect absorber was composed of a perforated plate and a coiled coplanar air chamber. These two designs can absorb low frequency sound within a narrow band. Labyrinthine acoustic metamaterials (LAMMs) composed of curled perforations have great potential applications since they maintain diverse properties such as double negativity, nearly zero density and large refractive index [125]-[127]. Zhang and Hu [128] developed a LAMM with curled perforations with one end closed and appropriate loss inside, which can perfectly absorb sound in low frequencies. Both position and bandwidth can be tuned. Another perfect sound absorber was constructed by attaching the lossy resonant plate to a backed rigid wall closely. The resonant plate was made of porous material in which the acoustic split ring resonator was embedded. The mechanism is the coupling the resonant plate to an air cavity in front of the rigid wall to achieve broad band absorption [129]. The similar idea of lossy resonant structure coupling with air was proposed by Starkey et al. [130]. They used rigid perforated plate separated from a rigid wall by a deep-subwavelength channel of air. This structure can be used as robust sound absorbing panels.

1.3.2 Classic HRs based sound absorber

The HR, well known as the sound absorber, has been widely used in noise reduction technology applications and studied extensively [131]-[135]. The acoustic HR is composed of an air cavity connected with outside space with a orifice or neck. The basic mechanical model of

the HR consists an air spring (the cavity), a mass (together with two parts: the air mass in the orifice or neck + vibrating mass) and a damper resulting from the radiation and the viscous forces. This spring mass damper model was first proposed by Ingrad ^[136]. The sound can be absorbed at the resonance frequency. The shape and geometry effect on the HR was studied and optimized ^[137]. Most recently, Cai et al. ^[138] developed a spiral neck of the HR which increased the neck length while can be used for space limitation application. The coupled HRs or HR array has been studied in order to increase the absorption efficiency at low frequency range ^{[139][140][141]}. Kim ^{[142][143]} theoretically illustrated the basic physical phenomena of the broadband sound absorption HR array and experimentally verified the absorptive characteristics. Each unit couples with each other and can achieve better sound absorption than single unit cell^[144], which induces the mutual acoustic impedance between radiators^[145]. Griffin et al. ^[146] proposed the coupled HRs for acoustic attenuation with addition duct or membrane which increase the coupling performance compared with only two HRs. However, it used add-on structures and only a narrow bandwidth was obtained.

HRs which are used as perfect sound absorber have been investigated in the last few years. Jimenez et al. ^{[147][148]} designed a thin panel with perforated thin closed slits and the upper wall is loaded by HRs. Strong dispersion caused by the slits below the resonance frequency of the HR resulted in cavity resonances accumulating at the limit of the band gap. The structure is stacked by several layers of such kind of thin panel with air gap between each panel. This kind of configuration is complex and not easy to fabricate. The test sample was made of three layers of thin panel with 3 HRs in each layer. The bandwidth above 50% sound absorption is not wide enough (approximately 30 Hz bandwidth) round the resonance

frequency 350 Hz. Li et al. ^[149] proposed a sound absorbing metasurface with coupled HRs. A hybrid resonance mode was generated by coupling different resonators. Over 99% energy was absorbed at central frequency with 50% absorption bandwidth of 140 Hz. The perfect HR sound absorber with 1/20 subwavelength has a simple structure configuration. However, the proposed design was only demonstrated by experiment results. Our perfect sound absorber panel is designed by inspiring Li's work.

Chapter 2

Basic theory for the honeycomb acoustic metamaterial

As the honeycomb sandwich panels are often used for weight-saving priority applications, they are required minimum stiffness as long as they can bear some maximum service loading and most of all, they must be as light as possible. Therefore, our goal based on honeycomb sandwich panel design is the structure with minimum weight and meets the constraints on stiffness and strength. Moreover, the honeycomb acoustic metamaterial keeps the integrity of the honeycomb panel. Thus the design focuses on the honeycomb core. Developing the mechanical properties of the honeycomb structure is the first step to design the honeycomb acoustic metamaterial.

Noise and vibration levels are the main comfort parameters for passengers in transportation system. Honeycomb sandwich panels process very poor noise barriers due to the high flexural stiffness in high frequency ranges and light weight in low frequency range. No-mass-attached on AMs are introduced in honeycomb acoustic metamaterial design, which produce the negative effective mass density at resonant frequency, where it breaks the mass law. The membrane is applied on honeycomb structures processing a perfect clamped boundary condition on each honeycomb core. The basic configuration of the acoustic metamaterial applied on sandwich panel is shown in Figure 2.1 This design can be taken as super lightweight and reduce the low-frequency noise.

Each unit cell of the honeycomb acoustic metamaterial can be treated as a tube with rigid walls of the honeycomb core. The acoustic impedances and transmission coefficients of each unit cell tube are obtained with impedance theory. The transmission characteristics of this impedance tube are going to be studied at the resonant frequency with the negative effective density. The impedance theory is going to be studied due to the impedance mismatch

between the membrane and the air. The basic theory of sound transmission through a limp panel is also illustrated in this part.

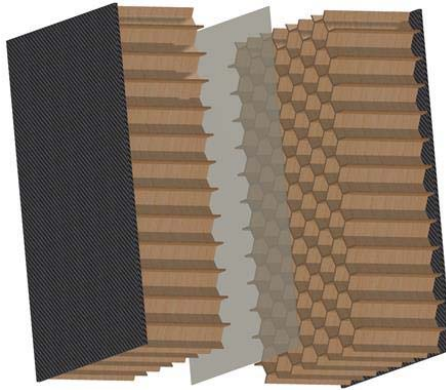


Figure 2.1 Configuration of acoustic metamaterial applied in sandwich panel.

2.1 Mechanical properties of honeycomb structures

Honeycombs employed to skis, aircraft, and space vehicles, are often used as cores in sandwich panels since they exhibit light, stiff properties. Lightweight structures made of two stiff, strong thin face sheets separated by a hollow lightweight honeycomb core are known as honeycomb sandwich panels. The materials of two face sheets are typically aluminum or fiber-reinforced composites, the cores are aluminum or paper-resin honeycombs, which have a cellular structure. The whole configuration of honeycomb panels increases the moment of inertia of the panel with little add-on weight, which processes an efficient structure for resisting bending and buckling loads. The mechanical behavior of a sandwich structures depends on the geometry and materials of both face sheets and cores. Our acoustic metamaterial design is required to maintain the mechanical properties of sandwich panels and focus on the honeycomb core structure.

Honeycomb core structures, shown in Figure 2.2, are two-dimensional cellular materials, which has two-dimensional array of hexagonal cells of the bee packing to fill a plane area. The cell shapes may vary for both isotropic and anisotropic. The most important structural characteristic of such a cellular solid is its relative density, ρ^*/ρ_s . ρ^* is the density of the honeycomb core and ρ_s is the material density of the solid which the honeycomb is made of. Relative density is relative to the porosity of cell structures, which is simply written as $1 - \rho^*/\rho_s$. The cells are usually hexagonal in section, and can also be triangular, or square, or rhombic as well. The regular array of prismatic hexagonal cells are simply shown as $l=h$.

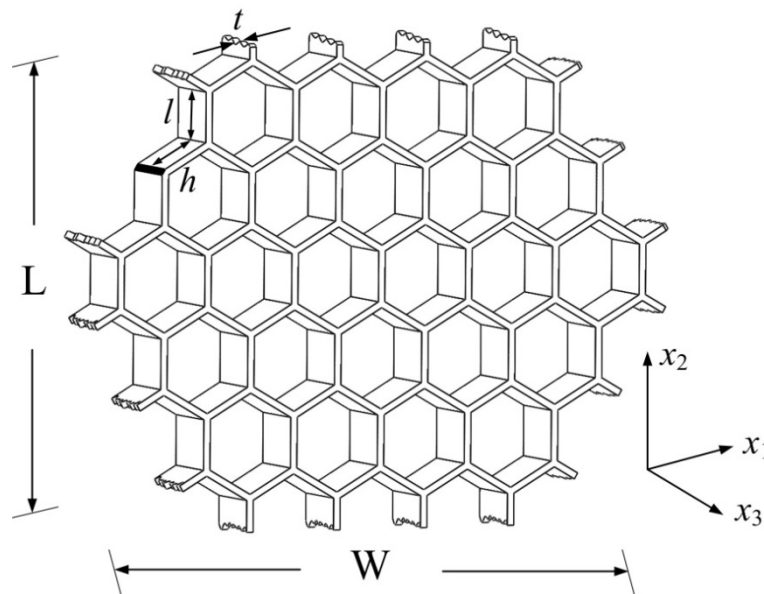


Figure 2.2 A honeycomb with hexagonal cells.

The materials for honeycomb product are now available as paper-resin polymer, metal and ceramic. The polymer and metal ones are used as cores of sandwich panels with a variety of applications from cheap construction building walls to advanced aerospace components.

The metal ones can also be used as energy-absorbing materials. Both the polymer and metal ones can be manufactured by corrugated process ^[102]; the expanded polymer or metal sheets are trimmed to desired L dimension and W dimension which are defined as ribbon direction and transverse direction respectively.

Understanding the mechanical properties of the honeycomb core is very important if such structure is to be used as loading bearing structure. It is also crucial to guide the honeycomb acoustic metamaterial structural design. The honeycomb is loaded in-plane (that is in x_1 - x_2 plane) including compression and tension. If the honeycomb is compressed, the cell walls deform from bending and follow the linear elastic deformation at the beginning. After bending beyond a critical strain, the cells collapse by elastic buckling, plastic yielding and creep fracture as the normal process of beam structure. But by the end of the cell collapse, the neighbor cell walls get closer and begin to touch each other, which densifies the structure and increase the stiffness simultaneously and rapidly. The only difference from compression progress is that the elastic buckling doesn't exist if the cell walls are under tension loading. Depending on the cell wall material, the honeycomb exhibits extensive plasticity if the cell wall material deforms plastically; the honeycomb will fractures easily if the material itself is brittle. When the honeycomb is on out-of-plane loading (that is the cell wall suffers extension or compression in x_3 direction.) the collapse stress are much larger.

The in-plane stiffness and strengths (in x_1 - x_2 plane) are lowest and out of plane stiffness and strengths (in x_3 direction) are much larger. Because the stress in this plane make the cell wall bend while they need additional axial extension or compression to deform ^[103]. The

honeycomb sandwich panel possesses strong property not only due to the high-moduli composite face sheets, also because the out-of-plane property gives the additional stiffness.

The in-plane mechanical properties are related to loads applied in x_1 - x_2 plane. The in-plane properties are isotropic if the hexagon is regular and all cell walls have the same thickness. There are two independent elastic moduli which are Young's modulus and shear modulus, and one stress. However, the properties are anisotropic when the hexagon is irregular or the cell walls in one direction are thicker than those in other directions. The elastic moduli are listed as the Young's modulus parallel to x_1 direction E_1^* ; the Young's modulus parallel to x_2 direction E_2^* ; shear modulus G_{12}^* ; and two Poisson's ratio ν_{12}^* , ν_{21}^* . The reciprocal relation, written as:

$$E_1^* \nu_{21}^* = E_2^* \nu_{12}^* \quad (2.1)$$

makes these five moduli to four independent ones.

The honeycomb is studied as a general case and the relative density can be derived based on the geometry parameters with arbitrary values: t , h , l and θ , shown as

$$\frac{\rho^*}{\rho_s} = \frac{t/l(h/l+2)}{2 \cos \theta (h/l + \sin \theta)} \quad (2.2)$$

where t/l is small.

When the honeycomb is loaded as linear elastic extension or compression, the cell walls are deformed by the bending caused by loads in x_1 direction and x_2 direction. The unit cell deformation is shown from Figure 2.3(a). The stress σ_1 is applied parallel to x_1 causing the

cell walls with length l to bend, and the cell shrinks along W direction, shown in Figure 2.3(b). Based on the beam theory, the Young's modulus E_1^* parallel to x_1 can be obtained as:

$$\frac{E_1^*}{E_s} = \left(\frac{t}{l}\right)^3 \frac{\cos \theta}{(h/l + \sin \theta) \sin^2 \theta} \quad (2.3)$$

Similarly, loading in x_2 direction causes the cell walls with length l to bend, and the cell shrinks along L direction, shown in Figure 2.3(c). The Young's modulus E_2^* parallel to x_2 can be written as:

$$\frac{E_2^*}{E_s} = \left(\frac{t}{l}\right)^3 \frac{(h/l + \sin \theta)}{\cos^3 \theta} \quad (2.4)$$

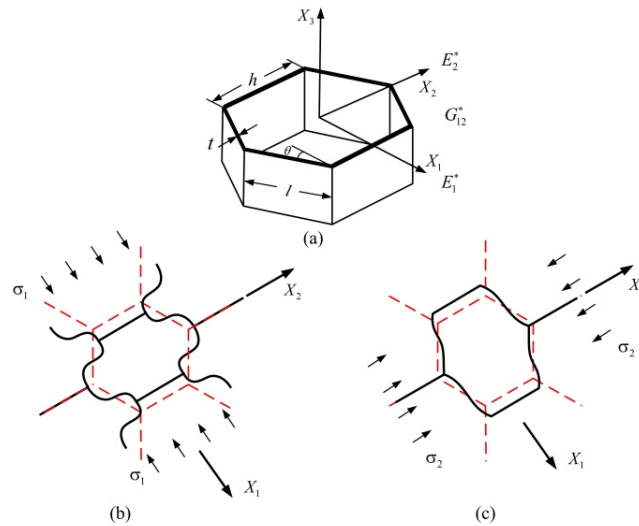


Figure 2.3 Honeycomb cell deformation under extension or compression: (a) the undeformed cell; (b) loading in x_1 direction; (c) loading in x_2 direction.

The Poisson's ratios under two directions' loading are calculated by taking the negative ratio of the strains. Compared with the two moduli above, they are obtained by loading parallel to x_1 direction and x_2 direction respectively as:

$$v_{12}^* = \frac{\cos^2 \theta}{(h/l + \sin \theta) \sin \theta} \quad (2.5)$$

$$v_{21}^* = \frac{(h/l + \sin \theta) \sin \theta}{\cos^2 \theta} \quad (2.6)$$

The shear modulus G_{12}^* can be calculated from shear stress divided by strain:

$$\frac{G_{12}^*}{E_s} = \left(\frac{t}{l}\right)^3 \frac{(h/l + \sin \theta)}{(h/l)^2 (1 + 2h/l) \cos \theta} \quad (2.7)$$

The out-of-plane properties of honeycomb structure can be used to describe the deformation of the honeycomb structures when they are loaded by normal or shear stress in planes containing the axis of the x_3 direction, shown in Figure 2.4.

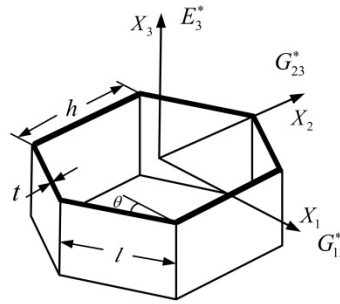


Figure 2.4 The mechanical properties of the honeycomb are derived under the loading normal to x_3 .

The extension or compression loading in x_3 direction, and of course the moduli are much larger for honeycomb cores than these values in-plane.

The Young's modulus E_3^* under the normal loading in x_3 direction can be calculated by:

$$\frac{E_3^*}{E_s} = \frac{t}{l} \frac{(h/l + 2)}{2(h/l + \sin \theta) \cos \theta} \quad (2.8)$$

The two Poisson's ratios ν_{31}^* and ν_{32}^* are equal to each other due to the cell solid itself:

$$\nu_{31}^* = \nu_{32}^* = \nu_s \quad (2.9)$$

The reciprocal relations give the Poisson's ratios ν_{13}^* and ν_{23}^* :

$$\nu_{13}^* = \frac{E_1^*}{E_3^*} \nu_s, \quad \nu_{23}^* = \frac{E_2^*}{E_3^*} \nu_s \quad (2.10)$$

The shear moduli are not easy to obtain by analyzing the stress distribution since all cell walls are under the non-uniform deformation. Because each cell attached by neighbors constraints with each other. The numerical method is possible for calculations ^[104]. The two shear moduli can be obtained by the upper and lower bounds, listed as:

$$\frac{t}{l} \frac{\cos \theta}{h/l + \sin \theta} \leq \frac{G_{13}^*}{G_s} \leq \frac{t}{l} \frac{\cos \theta}{h/l + \sin \theta} \quad (2.11)$$

$$\frac{t}{l} \frac{h/l + \sin \theta}{(1 + 2h/l) \cos \theta} \leq \frac{G_{23}^*}{G_s} \leq \frac{1}{2} \left(\frac{t}{l} \right) \frac{h/l + 2 \sin^2 \theta}{(h/l + \sin \theta) \cos \theta} \quad (2.12)$$

Commercial honeycombs normally have double thickness vertical wall due to the manufacturing technique. The resulting cells have four walls of length l with thickness t and two walls of length h with thickness $2t$. The cell with double thickness walls is shown in Figure 2.5. Since the in-plane uniaxial deformation is controlled by the wall thickness, the

Young's moduli E_1 and E_2 and the Poisson's ratios ν_{12} and ν_{21} are the same as those values for the honeycomb with uniform thickness walls (Eq. 2.3, Eq. 2.4, Eq. 2.5 and Eq. 2.6). There is a moderate difference for out-of-plane properties.

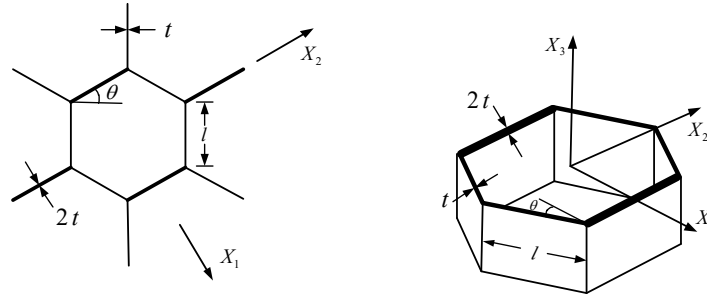


Figure 2.5 Honeycomb with non-uniform thickness cell walls.

The honeycomb core used for our metamaterial design is such kind of double thickness wall and the core material is aramid fiber/phenolic resin. The type can be found as Plascore PN2-1/4-2.0 or under Hexcel HRH-10-1/4-2.0. The effective elastic properties of such honeycomb core are listed in table 2.1.

Table 2.1 The effective elastic properties of aramid fiber/phenolic resin honeycomb

Parameter	Value
E_1	5.47×10^{-5}
E_2	5.47×10^{-5}
E_3	0.076
G_{12}	4.18×10^{-6}
G_{13}	0.014
G_{23}	0.029
ν_{12}	1
ν_{13}	0.14×10^{-4}
ν_{23}	0.14×10^{-4}

Unit: *GPa* (for modulus)

2.2 Mechanism of low-frequency sound insulation – negative effective mass density

Acoustic waves have large wavelength in audible regime from centimeters to meters. Phononic crystals, which enlighten the concept of acoustic metamaterial, have to on the order of the relevant wave length so they are mostly used in ultrasonic regime. AMs solve the size problem for lower frequencies sound attenuation without using bulky samples. AMs are composed of a class of structures in which each unit cell functionalizes its resonant property and used for manipulating acoustic waves. The acoustic waves that can be tuned on resonant frequency of a unit cell depend on its inner mass and restoring force, such as the spring. The resonant unit cell can be orders of magnitude smaller than the wavelength at the resonant frequency. Thus, membranes with the subwavelength characteristic have the application potentials for noise reduction in the effective frequency of interest from 50 to 2000 Hz in audible range. Most attracting aspect of the membranes is that they are lightweight and thin.

The negative effective mass density has implemented significantly subwavelength sound attenuation in the audible regime by breaking mass density law. It maintains the metamaterial characteristics that can effectively reduce the noise at low frequency broad band, which is the most difficult regime for noise attenuation due to the mass law. The effective negative mass density induced by a fully clamped subwavelength membrane has been theoretically and numerically studied in the section.

2.2.1 The classic one dimensional mass-spring infinite periodic system model

The dynamic effective mass can be mathematically analyzed by a simple one-dimensional mass-spring infinite periodic oscillator system under an external time harmonic

excitation force $F(\omega)$, where ω is the angular frequency. One basic unit is shown in Figure 2.6. A rigid mass m_1 with a cavity connects with a rigid sphere of mass m_2 by a massless and elastic spring with the constant G . The equation of motion for mass m_1 and m_2 under the exerted force can be written as

$$F(\omega) + G(x_2 - x_1) = m_1 \cdot \ddot{x}_1 \quad (2.13)$$

$$-G(x_2 - x_1) = m_2 \cdot \ddot{x}_2 \quad (2.14)$$

where x_1 and x_2 are the displacements of m_1 and m_2 respectively; the double overdo denotes a second-order time derivative and can be equated as the term $-\omega^2 x_{1,2}$; $G(x_2 - x_1)$ is the term resulting from the fixed spring which acts on mass m_1 and mass m_2 . The mass m_2 undergoes the harmonic oscillation. The displacement relation between the two mass can be calculated from Eq. 2.14.

$$\frac{x_2}{x_1} = \frac{G}{G - \omega^2 m_2} \quad (2.15)$$

If mass m_2 is considered inside of mass m_1 to compose a whole solid object with an effective mass M_{eff} , the whole solid with mass M_{eff} allows Newton's second law to be a new form:

$$F(\omega) = M_{\text{eff}} \cdot \ddot{x}_1 \quad (2.16)$$

The dynamic effective mass can be obtained by combining Eq. 2.13~Eq. 2.16:

$$M_{\text{eff}}(\omega) = m_1 + \frac{m_2 \omega_0^2}{\omega_0^2 - \omega^2} \quad (2.17)$$

where $\omega_0 = \sqrt{G/m_2}$ is the resonant frequency of mass m_2 . Eq. 2.17 gives the negative effective mass in frequency band from ω_0 to $\omega_0\sqrt{(m_1+m_2)/m_1}$. This unit configuration indicates the relative motions between the constituent components and a dynamic effective mass density ρ_{eff} can be defined as

$$\rho_{\text{eff}} = \langle f \rangle / \langle x \rangle \quad (2.18)$$

where f the force density, x is the displacement of the unit cell and the angular brackets denote averaging over the surface area of the unit cell.

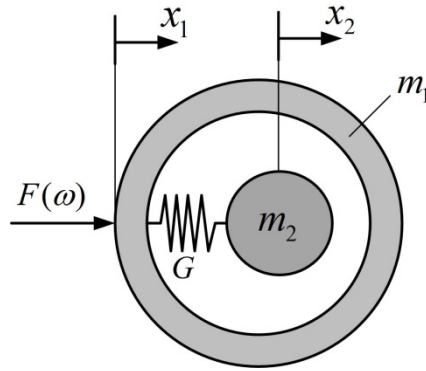


Figure 2.6 The unit oscillator with negative effective mass.

As the subwavelength unit cells are arranged periodically in AMs, the infinite one dimensional periodic mass-spring system with the unit cell components is used to describe the previous unit model connected with equal springs of constant K . Any two adjacent unit cells connect with a distance d as shown in Figure 2.7. The equilibrium equation for the n th mass is shown by the displacement X_n .

$$-\omega^2 M_{\text{eff}} X_n = K(X_{n+1} - X_n) + K(X_{n-1} - X_n) \quad (2.18)$$

Based on Bloch's theorem ^{[105][106]}, the displacement of each unit cell can be obtained by $X_{n+1} = X_n e^{iqd}$ with Bloch wave vector q . The dispersion relation for infinite periodic system is derived from Eq. 2.18 to be

$$\omega^2 M_{\text{eff}} = 4K \sin^2 \frac{qd}{2} \quad (2.19)$$

Assuming a finite periodic system has N unit cells, the transmittance T of the system can be defined as \bar{X}_N / \bar{X}_0 , where the bar denotes the amplitude of the time harmonic displacement. The displacement written as $X_n(t) = \bar{X}_n e^{-i\omega t}$ gives the relations:

$$(2K - \omega^2 M_{\text{eff}}) \bar{X}_n = K(\bar{X}_{n+1} + \bar{X}_{n-1}), \quad n=1, 2, \dots, N-1 \quad (2.20)$$

$$(K - \omega^2 M_{\text{eff}}) \bar{X}_n = K \bar{X}_{n-1}, \quad n=N \quad (2.21)$$

From the Eq. 2.20 and Eq. 2.21, the transmittance of the finite periodic system is

$$T = \left| \prod_{n=1}^N T_n \right| \quad (2.22)$$

where $T_n = \bar{X}_n / \bar{X}_{n-1}$ is calculated by the following relation,

$$T_n = \frac{K}{K(2 - T_{n+1}) - M_{\text{eff}} \omega^2}, \quad \text{with } T_{N+1} = 1. \quad (2.23)$$

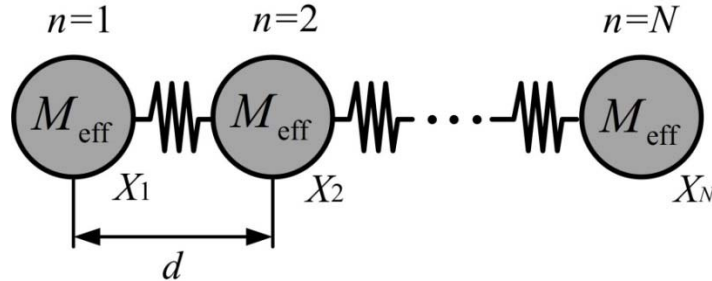


Figure 2.7 An infinite periodic mass-spring system.

S. Yao et al. [107] further studied the transmittance of the mass-spring system and experimentally verified the transmission properties of the finite periodic system. The model design and relevant results are helpful for a better understanding of the dynamic effective mass and the resonance of the membrane-type AMs.

2.2.2 The effective mass density and impedance match for a clamped membrane

The classic dynamic effective mass model of the metamaterials based on one dimensional periodic mass-spring units enlightened the studies on the mechanism of the membrane-type AMs. The flexible membranes stretched with a perfectly fixed boundary can achieve low-frequency sound blocking because the negative effective density occurs below a cut-off frequency at low frequencies. The clamped membrane as resonators can also be modeled as periodic mass-spring system: the membrane unit only contains one inertial mass but it is constrained by the fixed boundary which gives the unit mass additional stiffness. The one dimensional periodic mass-spring infinite model and its unit cell model can be shown in Figure 2.8.

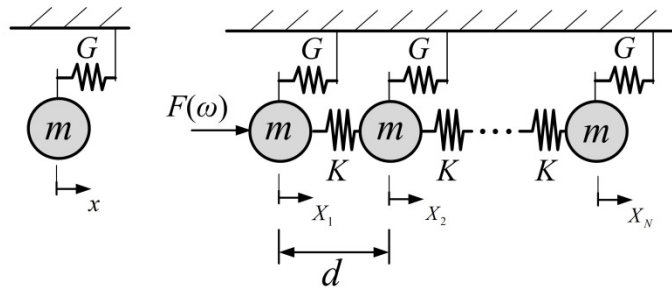


Figure 2.8 The infinite mass-spring system and its unit.

For a single unit cell, the mass m with a displacement x is under a harmonic excitation $e^{-i\omega t}$ and the excitation force is written as $F(\omega)$ with the angular frequency ω . Similarly

compared with the classic 1D model, Newton's law gives the motion of equation for the mass m :

$$F(\omega) = -m\omega^2 x + Gx \quad (2.24)$$

When the unit with a stiffness G is considered to be a solid mass that is connected with each other of a spring K , the solid mass is the effective mass m_{eff} . The motion equation is similar to Eq. 2.16, given by

$$F(\omega) = -m_{\text{eff}}\omega^2 x \quad (2.25)$$

Combining Eq. 2.24 and Eq. 2.25 gives the dynamic effective mass as:

$$m_{\text{eff}}(\omega) = m\left(1 - \frac{\omega_0^2}{\omega^2}\right) \quad (2.26)$$

where $\omega_0 = \sqrt{\frac{G}{m}}$. From Eq. 2.26, the system processes a broadband negative effective mass below the frequency ω_0 . The infinite periodic mass-spring system is composed of the effective mass units by spring K with a distance d . Compared with Eq. 2.18 and Eq. 2.19, The equilibrium equation for the n th mass and dispersion relation of the system are shown as

$$m \frac{d^2 X_n}{dt^2} = K(X_{n-1} - X_n) - K(X_n - X_{n+1}) - GX_n \quad (2.27)$$

$$\left(m - \frac{G}{\omega^2}\right)\omega^2 = 4K \sin^2 \frac{qd}{2} \quad (2.28)$$

The effective mass can also be obtained from Eq. 2.28 with the equation as Eq. 2.26.

S. Yao et al. [93] studied the transmittance of such a mass-spring system similar to this model and experimentally verified the results. It showed the transmission dropped at the cut-off frequency where all the unit cells had the same motion and the springs didn't deform. The

negative effective mass is below the cut-off frequency and equal to zero at the cut-off frequency. They also developed the negative mass effect for a membrane clamped in a solid waveguide. The effective mass density ρ_{eff} of the clamped waveguide can be theoretically predicted as:

$$\rho_{\text{eff}} = \rho_0 \left(1 - \frac{\omega_c^2}{\omega^2}\right) \quad (2.29)$$

where ρ_0 is the mass density of the membrane and ω_c is the lowest cut-off frequency which depends on the first eigenfrequency of the resonant membrane.

When a plane wave transmits through a clamped membrane, the effective mass density ρ_{eff} is also defined by the equation with a relation to the average force and acceleration, shown as

$$\bar{\rho}_{\text{eff}} = -\frac{1}{\omega^2 \bar{d}} \frac{\langle P \rangle}{\langle X \rangle} \quad (2.30)$$

where $\langle P \rangle$ the average value of surface pressure difference between two sides of the membrane, $\langle X \rangle = -\omega^2 \langle X \rangle$ is the average surface acceleration and \bar{d} thickness of the membrane. The averaged force and acceleration [57] demonstrated opposite in phase on the induced membrane at such resonant frequency will be emphasized later.

2.2.3 Negative-mass effect illustrated through wave propagative and evanescent modes

Another explanation for the negative-mass effect is given by the wave propagation through the object or system. It is known that wave vector is used to characterize the field distribution and spatial dispersion propagating waves. For the one dimensional spring-mass

periodic system, we can find that the effective mass will be zero when the wave vector q in Eq. 2.19 is zero. The zero wave vector indicates that the wavelength turns to infinite and no disturbance occurs in the system. That changes the problem to a vibration phenomenon.

Comparably, Analysis the normal displacement properties and the wave vector is another way to illustrate the negative mass phenomena for membrane-type AMs by introducing the relationship with the propagative and evanescent modes of the acoustic waves.

The normal displacement $X(x)$ can be written as the summation of two components:

$$X(x) = \langle X \rangle + \delta X(x) \quad (2.31)$$

where $\langle X \rangle \equiv \frac{1}{\pi R^2} \int_0^{2\pi} \int_0^R X(r, \phi) r dr d\phi$ is the normal displacement averaged over the surface area.[108]. r is the in-plane radial coordinate and ϕ are azimuthal coordinate respectively. R is the radius of the membrane when the membrane is assumed in a circular shape. If the membrane vibrates under the excitation, $\langle X \rangle$ can be indicated as the piston-like motion and the other component $\delta X(x)$ is spatial variation in high spatial frequency. $\delta X(x)$ is related to the in-plane Fourier wave vector $\mathbf{k}_{//}$ of the membrane. The magnitude of the wave vector is required as $|\mathbf{k}_{//}| \geq 2\pi / R$ since the normal displacement keeps continuous across the entire interface of the membrane and air. The dispersion relation of the acoustic wave is given by

$$\mathbf{k}_{//}^2 + \mathbf{k}_{\perp}^2 = (2\pi / \lambda)^2 \quad (2.32)$$

where \mathbf{k}_{\perp} is the normal wave vector and λ is the wavelength. $\delta X(x)$ gives imaginary \mathbf{k}_{\perp} because $\lambda \gg R$ in the high-spatial-frequency range, which means $\delta X(x)$ only counts for evanescent waves. The evanescently decaying acoustic waves indicate that no acoustic

energy transmits through the membrane and sound can't be transmitted in this frequency range. In contrast, $\langle X \rangle$ is a constant and in-plane $k_{//}$ distributes with a peak at $k_{//} = 0$. That means that the propagating waves can be reflected and transmitted when the sound hits on the membrane.

2.3 Sound reflection and transmission of the clamped membrane in a tube

A circular membrane sets up in a tube with clamped boundary condition as shown in Figure 2.9. The reflection and transmission characteristics have been studied using fluid impedance theory in this part. The acoustic wave is generated at $x=0$ with the input acoustic impedance Z_0 , and transmits through the membrane with a clamped boundary at $x=L$ with the acoustic impedance Z_A . Z_{AL} and Z_{AR} represent the acoustic impedances on the left side and right side of the membrane respectively. The acoustic wave is assumed transmitting to the infinite end. The membrane has the radius r and the surface area S .

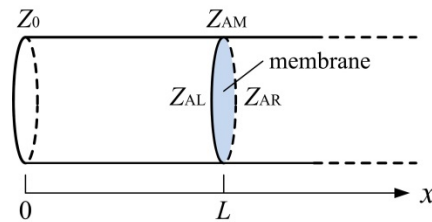


Figure 2.9 A clamped membrane inside the tube.

When the membrane isn't stretched, it can be modeled as a thin plate by the transverse displacement $x(r)$. The wave equation [108] is given by

$$D\nabla^4 x - \rho_M \omega^2 x = \Delta p \quad (2.33)$$

where $D = Eh^3 / 12(1-\nu^2)$ is the flexural rigidity and h , ρ_M , E , ν are the thickness, mass density per unit area of membrane, Young's modulus and Poisson's ratio. $\Delta p = p_{AL} - p_{AR}$ is the acoustic pressure difference of the left side and right side of the membrane. The incidence is assumed plane wave with uniform pressure on both sides. The general solution is obtained:

$$x(r) = -\frac{\Delta p}{\rho_M \omega^2} + AJ_0(k_M r) + BI_0(k_M r) \quad (2.34)$$

where J_n and I_n are the regular and modified Bessel's function of the first kind of the order n , respectively. Two constants A and B can be calculated by the clamped boundary condition of

the membrane [$x(r = a) = 0$, $\left. \frac{dx}{dr} \right|_{r=a} = 0$], shown as

$$\begin{aligned} A &= \frac{\Delta p}{\rho_M \omega^2} \cdot \frac{I_1(k_M a)}{J_0(k_M a)I_1(k_M a) + J_1(k_M a)I_0(k_M a)} \\ B &= \frac{\Delta p}{\rho_M \omega^2} \cdot \frac{J_1(k_M a)}{J_0(k_M a)I_1(k_M a) + J_1(k_M a)I_0(k_M a)} \end{aligned} \quad (2.35)$$

The mechanical response of the membrane driven by the force induced by acoustic pressure can be described by the mechanical impedance of the membrane Z_M , defined as the ratio of the force and the average surface velocity:

$$Z_M = \frac{\iint_S \Delta p(r) dS}{j\omega \bar{x}} \quad (2.36)$$

where $\bar{x} = (1/S) \iint_S x(r) dS$ is the average transverse surface displacement. The mechanical

impedance Z_M can be calculated from Eq. 2.34 and Eq. 2.35 as follows:

$$Z_M = -j\omega m_M \frac{I_1(k_M a)J_0(k_M a) + J_1(k_M a)I_0(k_M a)}{I_1(k_M a)J_2(k_M a) - J_1(k_M a)I_2(k_M a)} \quad (2.37)$$

where $m_M = \rho_M S$ is the mass of the membrane.

The incident acoustic pressure is loaded on the membrane, which induces the acceleration to the surrounding fluid. It is noticed that the normal velocity at any point on both sides of the membrane is continuous due to the velocity continuity so it can be written as $v_M = j\omega x$ that is particle velocity. The volume velocity u_V of the membrane is given by

$$u_V = \iint_S v_M(r) dS = \bar{v}_M S = j\omega \bar{x} S \quad (2.37)$$

Accordingly, the volume velocity on both sides of the membrane can be given by the velocity continuity as

$$u_V = u_L = u_R \quad (2.38)$$

The acoustic impedance can be defined by the pressure difference Eq. 2.36 divided by the volume velocity Eq. 2.37 as follows,

$$Z_{AM} = \frac{\Delta p}{u_V} = \frac{(Z_M / S) \cdot \bar{v}_M}{\bar{v}_M S} = \frac{Z_M}{S^2} \quad (2.39)$$

Thus the acoustic impedance of the membrane Z_{AM} is calculated by combing Eq. 2.37 and Eq. 2.39.

$$Z_{AM} = \frac{-j\omega m_M}{S^2} \frac{I_1(k_M a) J_0(k_M a) + J_1(k_M a) I_0(k_M a)}{I_1(k_M a) J_2(k_M a) - J_1(k_M a) I_2(k_M a)} \quad (2.40)$$

The membrane introduces a discontinuity in acoustic pressure field but continuity of acoustic velocity. The impedance relation between the membrane and the fluid in the tube can be expressed by acoustic pressure difference $\Delta p = p_{AL} - p_{AR}$ and the Eq. 2.38

$$\frac{\Delta p}{u_V} = \frac{p_{AL}}{u_L} - \frac{p_{AR}}{u_R} \Rightarrow Z_{AL} = Z_{AR} + Z_{AM} \quad (2.41)$$

where Z_{AL} and Z_{AR} represent the acoustic impedance of the fluid on both sides of the membrane. Assuming the fluid is air, since the waveguide tube goes to infinity, the impedance Z_{AR} that the plane wave generated behind the membrane is equal to $\rho_0 c_0 / S$, where ρ_0, c_0 are the air density and wave velocity in the air. The acoustic pressure reflection coefficient r_p can be expressed as [3]

$$r_p = \frac{Z_{AL} - \rho_0 c_0 / S}{Z_{AL} + \rho_0 c_0 / S} \quad (2.42)$$

The sound transmission coefficient T can be written as

$$T = 1 - |r_p|^2 \quad (2.43)$$

2.4 Summary

In the chapter, the mechanical properties of the honeycomb core have been studied, which leads the structural design of the honeycomb acoustic metamaterials in order to maintain the stiffness property of the honeycomb core. The metamaterials based on dynamic effective mass density has been first illustrated using a classic one dimensional mass-spring finite periodic system model; the effective negative density of membrane-type AMs can be analogically obtained and further modeled using the numerical method; By using acoustic wave propagation characteristics, the concept of the negative effective mass density of the membrane-type AMs was emphasized. Finally, the reflection and transmission characteristics

of the clamped membrane in a tube are presented and the interaction coupling between the air and impedance is studied by impedance theory.

Chapter 3

A lightweight yet sound-proof honeycomb acoustic metamaterial

A class of honeycomb acoustic metamaterial possessing lightweight and yet sound-proofing properties is designed, theoretically proven, and then experimentally verified. The proposed metamaterial can also be readily used as the core for constructing sandwich structures that could exhibit strong, lightweight, and sound-proofing properties simultaneously. The boundary condition with edge-constraint for each unit cell has great effect on STL of the panel. The effect on STL has been studied by changing the rigidity of the honeycomb core and the size of the metamaterial panel. Since the fibrous materials has good performance as absorbing materials in high-frequency sound attenuation. The sound transmission and absorption characteristics of honeycomb acoustic metamaterials are experimentally analyzed by adding glass fiber. Finally, the effect of panel size of the honeycomb sandwich structures on sound transmission is discussed.

3.1 Honeycomb acoustic metamaterial for low frequency noise reduction

Inspired by the wide-spread use of honeycomb structures and recent development of no-mass-attached membrane-type AMs, a honeycomb acoustic metamaterial was designed, theoretically studied and experimentally validated in this study. The basic configuration for the honeycomb acoustic metamaterial design has been shown in Chapter 1.

Figure 3.1 shows prototype of the honeycomb acoustic metamaterial where an isotropic membrane is adhered on the top of the honeycomb structure. The circular shape is also used as a sample for acoustical test. This inhomogeneous material is termed as a lightweight yet sound-proofing acoustic metamaterial. More importantly, as will be shown later, such a material can be readily implemented as the honeycomb core material and thus can potentially make honeycomb sandwiched structures possess simultaneously strong, lightweight and

sound-proofing properties. The honeycomb core is made of Aramid fiber, which is widely used in commercial areas and exhibits excellent flammability properties. It is manufactured from DuPont Nomex paper and coated with a heat resistant phenolic resin. The membrane is made of latex rubber.

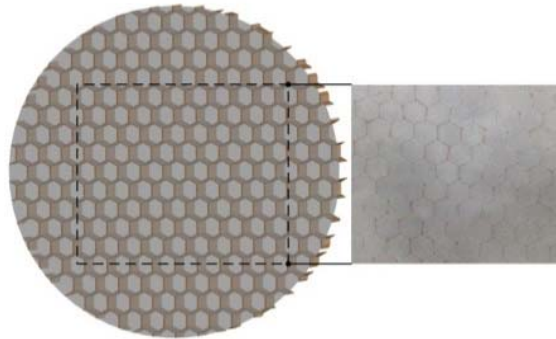


Figure 3.1 Metamaterial prototype used for the acoustical test.

Figure 3.2(a) shows a unit cell of the metamaterial where an isotropic membrane is fixed on the top surfaces of the honeycomb sidewalls. The hexagonal honeycomb core can be treated as a transversely orthotropic material, which is typically light in weight and its out-of-plane (x_3 direction) effective Young's modulus E_{c3} is considerably greater than the in-plane (x_1 - x_2) moduli E_{c1} and E_{c2} . Consequently, the proposed metamaterial can be modeled as a composite composed of an isotropic membrane and a homogenized, transversely orthotropic material, as shown in Figure 3.2(b).

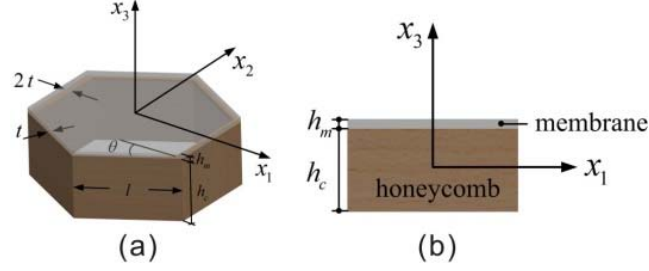


Figure 3.2 (a) Unit cell of the honeycomb membrane-type metamaterial. (b) An equivalent composite composed of a linearly isotropic membrane and a homogenized, transversely orthotropic material for the calculation of effective Young's modulus of the metamaterial in in-plane and out-of-plane directions.

Assuming the membrane and honeycomb core are linearly elastic and the membrane boundaries are perfectly clamped, as the composite is loaded along x_1 direction with a stress σ_1 , the membrane and honeycomb core deform the same (this is an approximation since there is a Poisson's ratio mismatch between the two materials). In addition, the force generated in the metamaterial is the sum of forces in the membrane and the honeycomb core. Thus

$$\varepsilon_1 = \varepsilon_{m1} = \varepsilon_{c1} \quad (3.1a)$$

$$\sigma_1 h = \sigma_{m1} h_m + \sigma_{c1} h_c \quad (3.1b)$$

where ε_1 , ε_{m1} , ε_{c1} , σ_1 , σ_{m1} , σ_{c1} are the normal strains and stresses for the metamaterial composite, membrane and honeycomb core, respectively. Unit thickness along the x_2 direction is assumed. Substituting the stress-strain relation ' $\sigma = E\varepsilon$ ' and Eq. 3.1 (a) into Eq. 3.1 (b), the effective Young's modulus for the metamaterial composite along the x_1 direction can be obtained as

$$E_1 = E_m \frac{h_m}{h} + E_{c1} \frac{h_c}{h}, \quad (3.2)$$

where E_m is the Young's modulus for the membrane. Since $E_{c1} = E_{c2}$, and using similar analysis, the effective Young's modulus E_2 will be equal to E_1 derived in Eq. 3.2. In contrast to being loaded in the x_1 direction, when the composite is loaded in the x_3 direction, the normal stress σ_3 in the composite must be identical to the normal stresses σ_{m3} and σ_{c3} produced in the membrane and the honeycomb core, respectively. The deformation δh for the metamaterial composite is attributed to the deformation of the membrane and honeycomb core, δh_m and δh_c , respectively. Thus

$$\sigma_3 = \sigma_{m3} = \sigma_{c3} \quad (3.3a)$$

$$\varepsilon_3 = \frac{h_m}{h} \varepsilon_{m3} + \frac{h_c}{h} \varepsilon_{c3} \quad (3.3b)$$

where ε_3 , ε_{m3} , ε_{c3} are the normal strains in the x_3 direction for the metamaterial composite, membrane and the honeycomb core, respectively. Substituting the stress-strain relation ' $\sigma = E\varepsilon$ ' and Eq. 3.3 (a) into Eq. 3.3 (b) yields

$$E_3 = \frac{E_m E_{c3}}{(h_m/h)E_{c3} + (h_c/h)E_m} \quad (3.4)$$

where $E_{c3} = 2E_0 t / [l(1 + \sin \theta) \cos \theta]$ [Appendix I] (E_0 is the Young's modulus for the honeycomb material) or can be directly measured through a compressional test. Eq. 3.4 gives the effective out-of-plane Young's modulus E_3 for the metamaterial composite. The effective static density for the metamaterial composite can be readily shown as

$$\rho = \frac{\rho_m h_m + \rho_c^* h_c}{h} \quad (3.5)$$

where $\rho_c^* = 2\rho_0 t / [l \cos \theta (1 + \sin \theta)]$ is the effective static mass density of the honeycomb core, ρ_m is the membrane density and ρ_0 is the mass density of the honeycomb material.

The honeycomb core of the proposed metamaterial has the dimensions as follows: $t = 0.08 \text{ mm}$, $l = 3.65 \text{ mm}$, $h_c = 25 \text{ mm}$ and $\theta = 30^\circ$. This θ essentially resulted in a regular hexagon. It is advantageous because the highest crush strength per unit mass can be obtained when cell shape is of regular hexagon ^[109]. Two side walls (one marked in the figure and the opposing one) had a thickness of $2t$. The other side walls had a thickness of t . This is common and is a result of the production method. The membrane material was latex rubber with a thickness $h_m = 0.25 \text{ mm}$. The Young's moduli E_{c3} was measured through a stabilized compressional test and was 76 MPa . E_{c1} and E_{c2} can be then estimated using $E_{c1} = E_0 (t/l)^3 \cos \theta / [(1 + \sin \theta) \sin^2 \theta]$ from Appendix I and both were 0.055 MPa . The density of the honeycombe core is $\rho_c^* = 32 \text{ kg/m}^3$. The Young's modulus, mass density and Poisson's ratio for the latex rubber were $E_m = 7 \text{ MPa}$, $\rho_m = 1000 \text{ kg/m}^3$ and $\nu_m = 0.49$, respectively. After substituting the relevant parameters to Eq. 3.2, it is found that the in-plane effective Young's moduli E_1 and E_2 of the metamaterial composite are about twice that of the effective Young's moduli of the honeycomb core E_{c1} and E_{c2} . In view of Eq. 3.4, since $h \gg h_m$, the out-of-plane effective modulus E_3 of the metamaterial is thereby $\approx E_{c3}$. Consequently, the proposed metamaterial retains the out-of-plane stiff property of the honeycomb core and in addition, could potentially improve the in-plane Young's modulus of the honeycomb core (by 100% in this specific case). The effective static density of the metamaterial composite was $\rho = 41.58 \text{ kg/m}^3$, which can be obtained from Eq. 3.5. The x_3 direction Young's modulus

to density ratio (stiffness to density ratio) was then $1.83 \times 10^6 \text{ m}^2/\text{s}^2$. The metamaterial composite thereby inherits the lightweight property of the honeycomb core and exhibits as a lightweight material. For the interest of acoustics, the mass per unit area of the metamaterial composite was $1.05 \text{ kg}/\text{m}^2$.

The metamaterial composite that was used for the acoustic test is shown in Figure 3.1. It had a diameter of 10 cm . The sound transmission measurements were conducted in the Bruel and Kjaer 4206 impedance tubes. The frequency range of the acoustical test was 50 Hz - 1600 Hz . The corresponding wavelengths range from 6860 mm to 214 mm . The wavelengths were at least two orders of magnitude larger than the cell dimensions. Numerical simulations were performed using the acoustic-structure interaction module of COMSOL multiphysics. Due to the periodic repetition of the honeycomb cells as well as to enable computationally feasible modeling, only a single unit cell was considered in the model. The membrane was assumed to be ideally clamped at cell boundaries. As will be shown below, in spite of these assumptions, the simulation results still capture major trends of the STL behavior.

Figure 3.3 shows the experimental and simulation STL results for honeycomb cell structure only and the proposed honeycomb metamaterial. The STLs are shown in unit decibel (dB). Since the honeycomb cell structure is holey and lightweight, as expected it exhibited very poor acoustical performance. As shown by the blue line in the figure, the sound can be almost 100% transmitted. With membrane added, the resulting structure showed distinct STL improvement over the entire frequency range under consideration as shown by the red solid line. The STL was especially high ($>25 \text{ dB}$) at low frequencies ($< 500 \text{ Hz}$) and decreased monotonically as the frequency increased before the STL dip at around

1100 Hz. The curve continued to rise up afterwards. The average STL is 21 dB over the 50 - 1600 Hz frequency range vs. 0.2 dB for honeycomb only. The simulated STL results by considering different loss factors for the membrane captured the same trend as experiment and the predicted STL at the STL dip frequency increased as the loss factor increased (a loss factor at 0.2 was chosen for the simulation thereafter as it yielded the best agreement at the STL dip frequency).

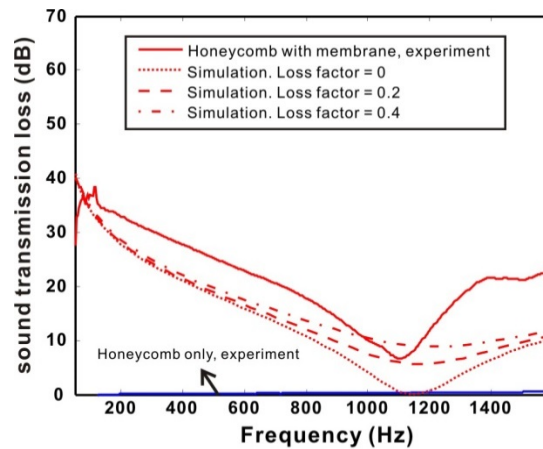


Figure 3.3 Experimental and simulation STL results for honeycomb core only and the proposed metamaterial (honeycombe core with membranes).

The anomalous STL is reminiscent of what was theoretically and experimentally described in the context of the plasmonic checkerboards ^[110] (broadband extraordinary transmission/absorption in the low frequency regime) and can be understood by the negative density induced by the membranes ^{[92][93][111]}. In this study, The theoretical effective dynamic mass density of the membrane can be estimated by considering the membrane subjected to a

time-harmonic excitation with boundaries clamped at the honeycomb walls and therefore reads from Eq. 2.29 in Chapter 2, which is rewritten using $\omega = 2\pi f$ as

$$\rho_{eff} = \rho_m \left(1 - \frac{f_r^2}{f^2}\right) \quad (3.6)$$

where f_r is the lowest eigenfrequency of the hexagonal shape membrane and was determined as $f_r = 1160$ Hz using the finite element analysis. This frequency corresponds to the dip frequency shown in Figure 3.4. On the other hand, by prescribing a time-harmonic boundary load at the membrane surface, the dynamic density can be numerically obtained by dividing the out-of-plane volume averaged stress by the product of the volume averaged acceleration and the membrane thickness, i.e., $\rho_{eff} = \bar{\sigma}_{zz} / \bar{a}_z h_m$, similarly shown as Eq. 2.30 in Chapter 2. Figure 3.4 shows the effective dynamic mass density of the membrane as a function of frequency both theoretically and numerically.

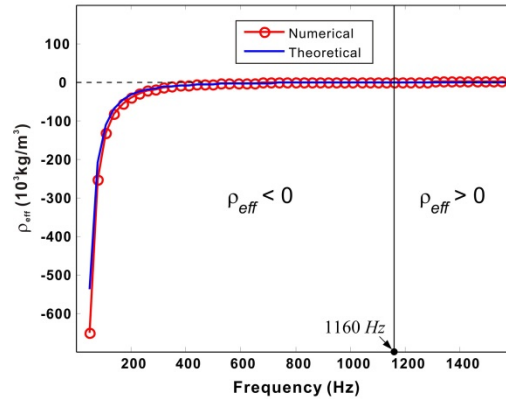


Figure 3.4 Effective dynamic mass density of the membrane AM as a function of frequency.

It is seen that the lowest eigenfrequency $f_r = 1160 \text{ Hz}$ separates the negative and positive effective density regions and has a zero effective density at which the membrane resonates and results in the STL dip.

The zero effective dynamic density indicates an infinite wavelength in the sample since $\lambda \propto \rho_{eff}^{-1/2}$ (λ is the wavelength). The high STL at low frequencies is attributed to the negative density which introduces exponentially decaying waves with a decaying length $\Delta d \propto |\rho_{eff}^{-1/2}|$. Since the magnitude of the effective density increases with decreasing frequency, the decaying length Δd of the evanescent wave reduces as the frequency deviates from the lowest eigenfrequency, leading to a greater STL. A simple model of a subwavelength size tube with a clamped membrane inside can also be utilized to interpret the high STL at low frequencies. As shown in Figure 2.9 in Chapter 2, the impedance of the membrane can be recalled from Eq. 2.36.

$$Z_M = \frac{\iint_S \Delta p(r) dS}{j\omega \bar{x}} = \frac{\langle P \rangle}{\langle X \rangle} \quad (3.7)$$

where $\langle P \rangle$ is the surface-averaged pressure difference on two sides of the membrane, $\langle X \rangle$ is the surface-averaged velocity. The negative effective density can be related to the impedance of the membrane by substituting Eq. 2.30 into Eq. 3.7, defined as

$$Z_M = \frac{\langle P \rangle}{\langle X \rangle} = \frac{\langle P \rangle}{j\omega \langle X \rangle} = j\omega \rho_{eff} \bar{d} \quad (3.8)$$

where \bar{d} the mean thickness of the membrane. Thus, the near-zero ρ_{eff} indicates the near-zero acoustic impedance of the membrane as $Z_{AM} = Z_M / S^2$ from Eq. 2.39. The effective impedance can be well matched to the acoustic impedance in air implying from Eq. 2.41, as $Z_{AL} = Z_{AR} + Z_{AM} \approx \rho_0 c_0 / S$ which means the clamped membrane perfectly couples with the incident sound. $\rho_0 c_0 / S$ is the air's impedance. Therefore, the acoustic pressure reflection coefficient $r_p \approx \frac{Z_{AL} - \rho_0 c_0 / S}{Z_{AL} + \rho_0 c_0 / S}$ (Eq. 2.42) is almost equal to zero, which would allow the perfect transmission without considering the damping of the membrane. At low frequencies (below the first resonance frequency of the clamped membrane), the acoustic impedance of the membrane Z_{AM} can be written as $Z_{AM} = 1 / (j\omega C_{AM}) + j\omega M_{AM}$ ^[108], where C_{AM} and M_{AM} indicate the compliance and acoustic mass respectively. Eq. 2.41 can be written as $Z_{AL} = \rho_0 c_0 / S + 1 / (j\omega C_{AM}) + j\omega M_{AM}$ and according to Eq.2.42, as ω approaches zero, r_p approaches 1, implying total reflection.

The STL curve can be effectively tuned by adjusting the location of the first resonance frequency. The analytical solution for clamped circular thin membrane plates is used for approximating the actual hexagonal plated to gain some insights, because the analytical solution for hexagonal plates is yet to be analytically known or not found. The lowest resonance frequency for a clamped circular thin plate is $f_r = 0.4694h\sqrt{E / [\rho(1-\nu)]} / a^2$, where a is the radius ^[108]. f_r is therefore proportional to the plate thickness h and stiffness. Figure 3.5 shows the STL curves from simulation and experiments of two metamaterial samples with membrane thicknesses at $h_m = 0.25 \text{ mm}$ and $h_m = 0.2 \text{ mm}$, respectively. The

experimentally obtained lowest resonance frequency for the 0.25 mm membrane (blue solid line) was 1100 Hz, and was reduced to 970 Hz for the 0.20 mm membrane (black solid line). The simulated STL results (dashed lines) matched quantitatively well with experimental results. The lowest eigenfrequencies calculated were 1160 Hz and 920 Hz for the 0.25 mm and 0.2 mm membranes, respectively. Although reducing the membrane thickness can give rise to a reduced weight-penalty, it is noticed from Figure 3.5 that a thinner membrane resulted in an overall reduction in STL possibly due to the reduced membrane mass.

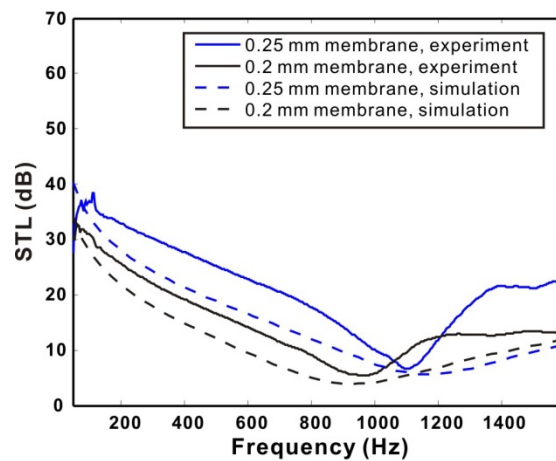


Figure 3.5 STL curves of two metamaterial samples with membrane thicknesses at $h_m = 0.25$ mm and $h_m = 0.2$ mm, respectively.

When the pretension effect is practically incorporated in the membrane induced from shrinkage during manufacturing, it could provide additional “apparent” stiffness to the membrane and thus increase the lowest resonant frequency of the membrane. Figure 3.6 shows the STL of two 0.2 mm thick membranes with one of the samples having pretension applied (approximately 5 N/m). The experimental results show that the pretensioned sample

(solid red line) has a higher lowest eigenfrequency (1104 Hz) than that of the sample (solid black line) without pretension (972 Hz). The simulation results confirmed this finding.

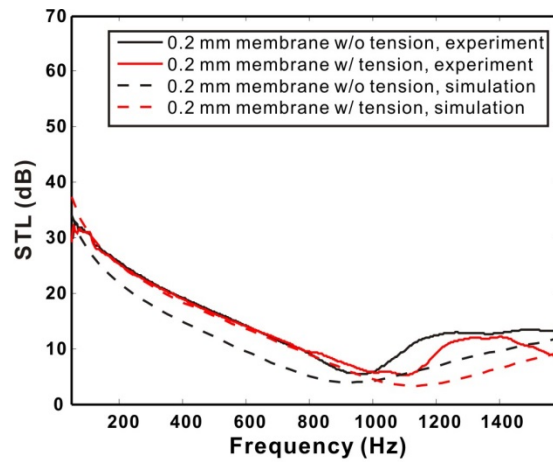


Figure 3.6 The STL of two 0.2 mm thick membranes with one of the samples having pretension applied (approximately 5 N/m).

To further improve the acoustical performance, the metamaterial with membranes adhered on both the top and bottom sides of the honeycomb structure was also explored. The effective static density of the metamaterial composite was increased to $\rho = 50.98 \text{ kg/m}^3$. Figure 3.7 shows that, comparing with the sample with only a single membrane, two membranes combined can enhance the STL by as much as another 20 dB. The STL at low frequencies ($< 500 \text{ Hz}$) was consistently greater than 45 dB. The average STL was 37 dB over the frequency range from 50 to 1600 Hz. This remarkable result was achieved at a very low mass per unit area (1.3 kg/m^2). The overall STL of the metamaterial with two membranes attached is not a simple summation of the STL of two single membrane metamaterials. This is due to the mutual interaction between the two membranes, as multiple reflections occur

between them. Naturally, standing waves could be generated. According to the normal mode theory, the lowest frequency normal mode would have a wavelength twice as long as the distance between the two membranes, such that the normal mode frequency will be around 6.8 kHz , considerably higher than the frequency range of interest. In fact, if there were a sufficient number of membranes arranged in series, Bragg scattering will prevail at this frequency and lead to a STL peak. It is also noticed that two hybrid modes can be seen for the double membranes system if no damping is considered, as shown by the black line in Figure 3.7, where the first STL dip frequency represents the two membranes vibrating in unison and the mode frequency (1160 Hz) is independent of the number of the membranes. This can be validated from the one membrane system as shown by the dotted red line in Figure 3.3, where the STL dip frequency occurs at the same frequency. The second STL dip frequency (1340 Hz) is for the case where the two membranes vibrate out of phase. However, when damping is taken into account which counteracts the resonances, the STL curve is smoothened as shown by the blue dashed line in Figure 3.7 and it appears that the first “resonance frequency” has shifted upwards compared with the one membrane system. It is anticipated that the overall STL can be further enhanced by stacking more membranes in series with the sacrifice of weight. Furthermore, the existence of the STL dip is not a critical issue. It occurred at a relatively high frequency (above 1 kHz) in this case as we intentionally designed and there are many low weigh-penalty solutions available in reducing the high frequency noise that is shown later. This STL dip frequency could be further shifted to an even higher value by reducing the unit cell size or increasing the membrane thickness. This, however, will increase the static density of the metamaterial. The low STL at this frequency

can be also improved by adopting a membrane material that has a high loss factor, as suggested by Figure 3.3.

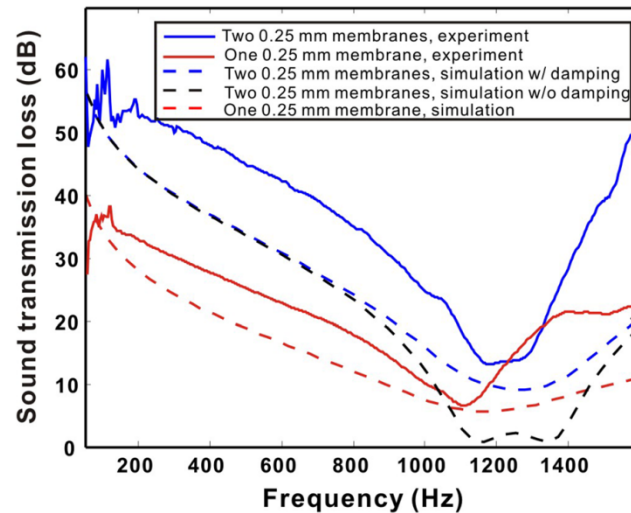


Figure 3.7 Comparison of the STL for the metamaterial sample with two membranes attached on the top and bottom surfaces of the honeycomb walls and the metamaterial sample with a single membrane. Each membrane had a thickness of $h_m = 0.25$ mm.

A great potential of the proposed acoustic metamaterial lies in that it can be readily modified to make honeycomb sandwich structures which could potentially be simultaneously strong, lightweight, and sound-proof. While conventional honeycomb structures comprise a honeycomb panel sandwich between two face sheets and are well known to have extremely high stiffness to weight ratios, a different sandwich structure would consist of two face sheets with one or more membranes sandwiched between honeycomb panels. Such a structure with one membrane incorporated was measured in comparison with a conventional sandwich panel for their STL and the results are shown in Figure 3.8. The two face sheets are made of

carbon fiber had a thickness of 1 *mm*. The total weight for the sandwich panel without the membrane was 29.2 g, whereas the sandwich panel with the membrane weighted 31 g which was 6% higher. Simulations were not performed for this set of experiments because the acoustical properties of the facesheets are unknown. The conventional sandwich panel (as shown in blue line) yields a STL dip frequency (around 820 *Hz*) which is due to the resonance in sandwich honeycomb structures. The presence of the membrane dramatically improved the STL, particularly in the low frequency region below the first resonance frequency of the membrane. The properties of the membrane seem to dominate the acoustical performance the sandwich panel. The STL at low frequencies (500 *Hz*) was consistently greater than 50 *dB*. The average STL over the 50-1600 *Hz* range was 40 *dB* (w/membrane) vs. 31 *dB* (w/o membrane). A higher STL is expected with more membranes added. It is also noted that the addition of the membranes is not expected to degrade the mechanical property of the honeycomb, which is crucial for the future applications.

Finally, experimental results of another simultaneously strong, lightweight, and sound proofing metamaterial are presented. The structure of this material is similar to that discussed in the main body of the paper. However, the membranes are located at the center, as opposed to the top or the bottom of the honeycomb core. A 3D printing technique was used to fabricate this metamaterial. The prototype is shown in Figure 3.9.

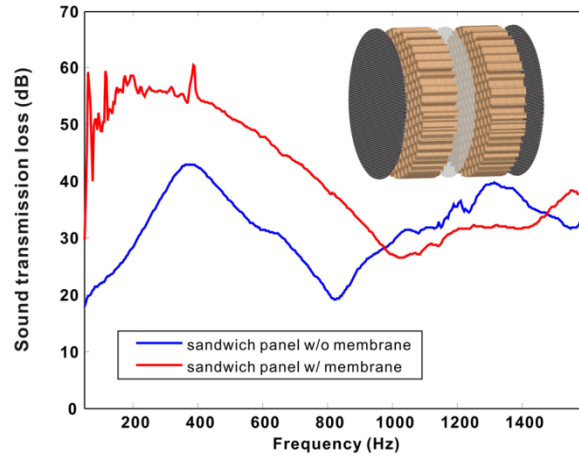


Figure 3.8 Comparison of the STL for a sandwich panel with membranes and a sandwich panel without membranes. The inset figure shows the structure of the sandwich panel with membranes.

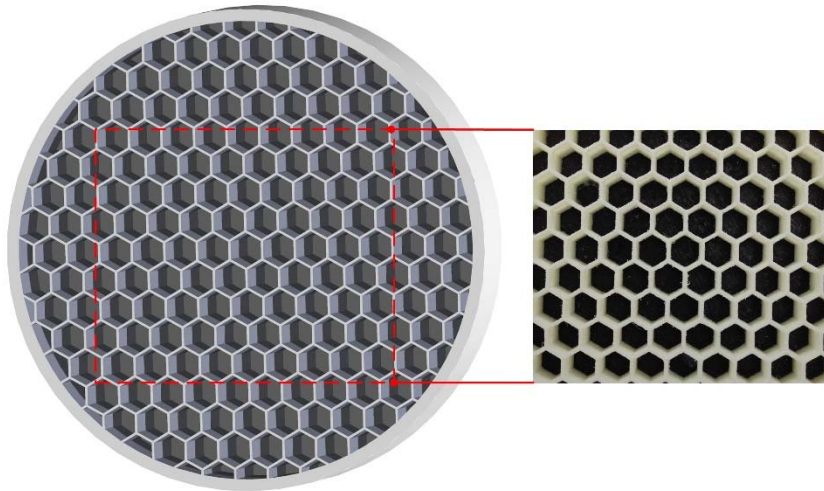


Figure 3.9 Sketch of the metamaterial prototype (left). A photo of the prototype (right).

The honeycomb material is rigid opaque photopolymer, which has a Young's modulus E_0 at around 3 GPa and a density ρ_0 at 1170 kg/m³. The membrane was printed using a rubber-like material with a thickness at $h_m=0.8$ mm. Other dimensions are as follows: $t = 0.5$ mm, $l = 3.65$ mm, $h_c = 25$ mm and $\theta = 30^\circ$. The membrane and wall thickness are relatively thick due to the limitation of the 3D printing resolution. In addition, in this structure, all cell wall thicknesses are identical and equal to t . The effective density and Young's modulus of the honeycomb core can be calculated using Eq. 2.8 and Eq. 2.2, and are 410 MPa and 185 kg/m³. Since the membrane cells were printed in a way that as if they were attached to the honeycomb walls, they are not expected to significantly alter the Young's modulus in the x_3 direction. Consequently, $E_3 \approx E_{3c}$. By recognizing that for a single unit cell,

$$Ah_m\rho_m + 3lt\rho_0h_c = \rho(A + 3lt)h_c \quad (3.9)$$

where A is the area of the hexagon, $A = 2l^2\cos(\theta)(1+\sin(\theta))$, the mass density of the metamaterial (honeycomb + membrane) ρ is estimated to be 187 kg/m³. The mass per unit area is 4.68 kg/m². The stiffness-density ratio is 2.19×10^6 m²/s². The experimental results of STL can be seen in Figure 3.10. The low frequency STL is consistently greater than 55 dB. The average STL over 50 – 1600 Hz is 50 dB. The resonance frequency of the membrane is estimated to be around 3 kHz, therefore the STL dip is not seen in the figure.

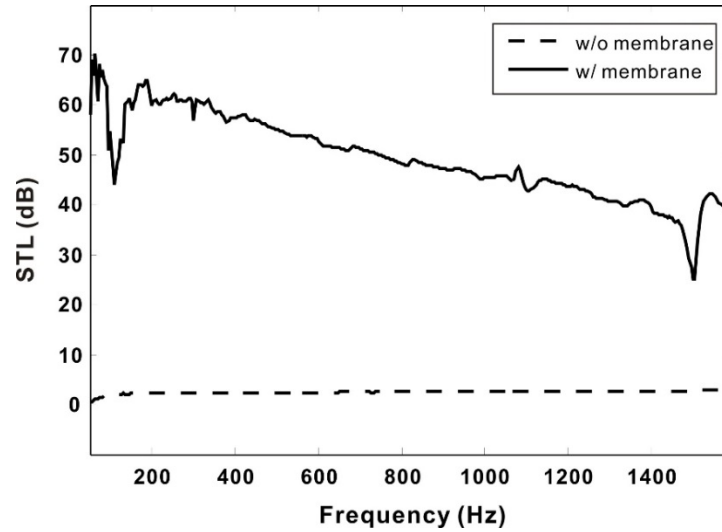


Figure 3.10 STL experimental results of the prototype.

3.2 Experimental study on honeycomb acoustic metamaterial using sound absorbing materials

Porous and fibrous materials are widely used in aerospace and buildings due to the excellent acoustic and thermal performance. It is well known as the sound insulating/absorbing layers inside the panels or walls to absorb sound energy in mid-to-high frequency range [112][113]. Porous materials are characterized by seven or more parameters, such as bulk density, Young's modulus, associated loss factor, Poisson's ratio, porosity, structure factor and flow resistivity and etc. [114]. The fiber diameter and porosity are the key factors that influence the acoustic absorption/insulation and vibration damping properties, thus many researchers mainly worked on the acoustic properties of the fibrous materials [115]-[118]. Glass fiber is one of the important fibrous materials for noise control in high frequency range with a little mass penalty. Therefore, the honeycomb metamaterial with

enforced glass fiber has been experimentally studied in this section. Characteristic results of sound transmission loss and absorption are compared respectively for different structural configurations from honeycomb core based structure to the whole sandwich panel.

Glass fiber is fabricated into layers with different thickness and properties, which is called glass fiber felts. It is made of pure glass fiber and phenol resin adhesive by centrifugal spinneret blow system. The acoustic waves interact with the fibers when the sound transmits through the glass fiber the sound energy dissipates due to the friction between the sound waves and glass fiber. The glass fiber felts are well trimmed to fit each unit cell of the honeycomb metamaterial, as shown in Figure 3.11.

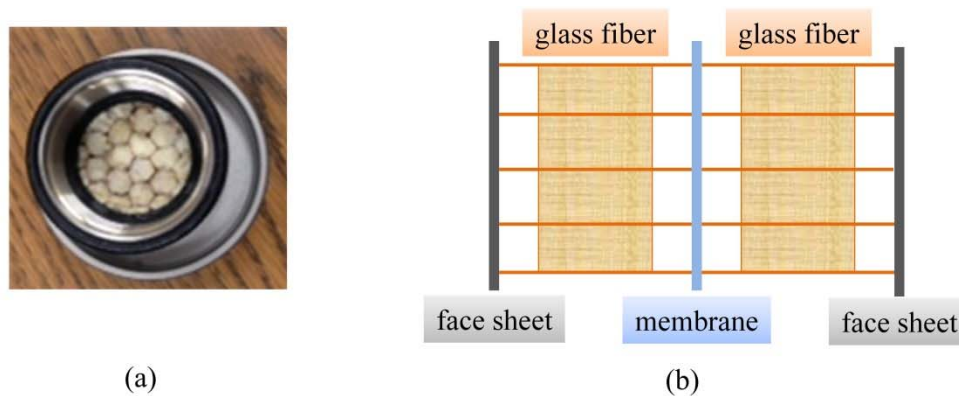


Figure 3.11 Test sample is 29 mm in diameter: (a) Glass fiber is trimmed and inserted in the honeycomb core. (b) The configuration of honeycomb metamaterial with the glass fiber inserted.

The test of STL and sound absorption coefficient (SAC) were conducted using B&K impedance tube with 29 mm in diameter and the acoustic measurements were carried out in the frequency range of 300 – 6400 Hz. The whole honeycomb configuration of the test

sample is composed of a membrane, two face sheets and trimmed glass fiber shown in Figure 3.11(b). The STL and SAC test were conducted for each component and any two components which were assorted in pairs. So there were six configurations in total and shown in Figure 3.14.

STL is the sound intensity decrease after the sound pressure wave propagates through a kind of material. In other words, it can test the ability of the material to block sound and defined as the ratio of the transmitted sound energy to incident sound energy. The measurement is conducted using impedance tube and based on the Transfer Matrix Method. The basic test bench includes a tube, four microphones and a frequency analysis system, shown in Figure 3.12. The loudspeaker is used to generate plane waves with a broadband noise signal. The test sample is mounted in the tube with two microphones on each side. The sound pressure at the four locations can be examined by their relative amplitude and phase and can be obtained as the summation of the sound pressure in two directions. The acoustic transfer matrix is written as

$$\begin{bmatrix} P_{x=0} \\ v_{x=0} \end{bmatrix} = \begin{bmatrix} T_{11} & T_{12} \\ T_{21} & T_{22} \end{bmatrix} \begin{bmatrix} P_{x=h} \\ v_{x=h} \end{bmatrix} \quad (3.10)$$

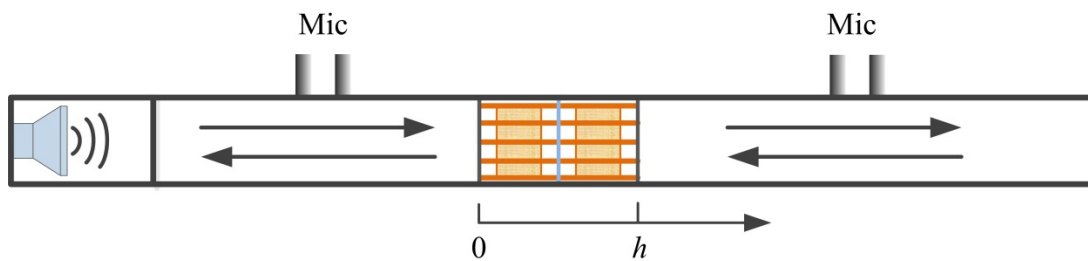


Figure 3.12 STL test tube (four microphones).

The transfer matrix elements can be calculated by the sound pressure and normal particle velocities at two ends of the sample. Therefore the sound transmission and reflection coefficients can be obtained with respect to the transfer matrix elements ^[119]:

$$T = \frac{2e^{ikd}}{T_{11} + (T_{12} / \rho_0 c) + \rho_0 c T_{21} + T_{22}} \quad (3.11)$$

$$R = \frac{T_{11} + (T_{12} / \rho_0 c) - \rho_0 c T_{21} - T_{22}}{T_{11} + (T_{12} / \rho_0 c) + \rho_0 c T_{21} + T_{22}}$$

The normal incidence STL can be written as

$$STL = 20 \log_{10} \left| \frac{1}{T} \right| \quad (3.12)$$

The normal incidence SAC is also based on transfer matrix method but the test sample is mounted adjacent to the hard termination at the end of the tube shown in Figure 3.13, which means the particle velocity at $x=h$ is equal to 0. Only two microphones are used for test.

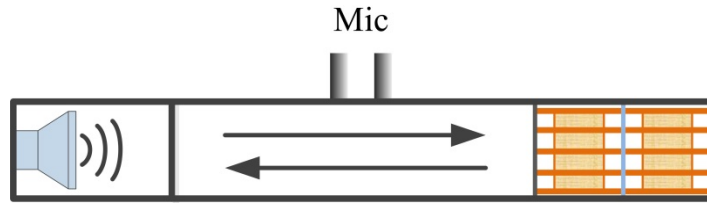


Figure 3.13 SAC test tube (two microphones)

The normal incidence reflection coefficient in two microphones method can be calculated as

$$R = \frac{T_{11} - \rho_0 c T_{21}}{T_{11} + \rho_0 c T_{21}} \quad (3.13)$$

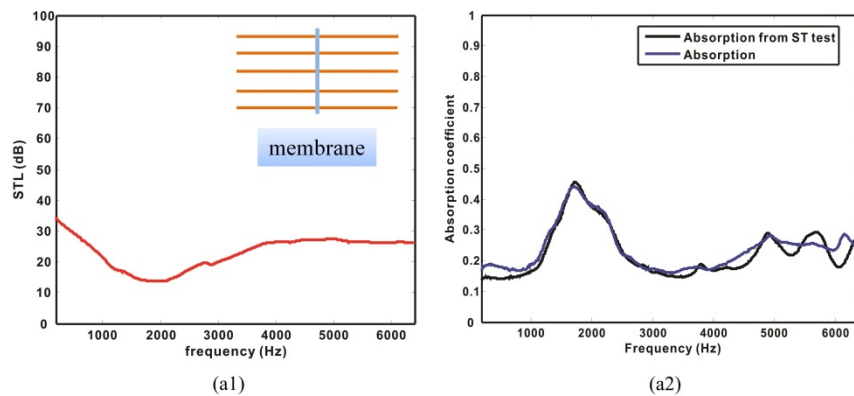
The SAC can then be written as

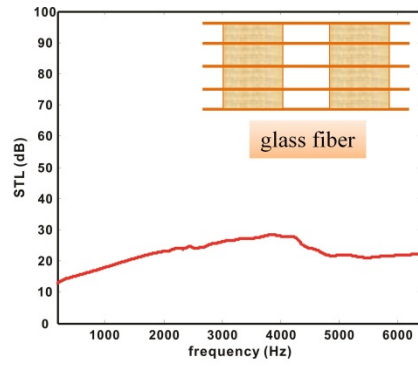
$$\alpha = 1 - |R|^2 \quad (3.14)$$

It can be noticed that the SAC can be obtained from both the STL (four microphones) method and hard termination method (two microphones). The sample can't move and is confined by the hard termination while for the STL method, the sample can move freely. So the results are more sensitive to the boundary condition which can shift the resonance of the sample if using STL method. The stiffer materials will increase the shearing resonance effect so that it can increase the discrepancy between the two methods [119]. Thus the SAC results can be affected by the circumferential boundary conditions and the stiffness of the sample itself.

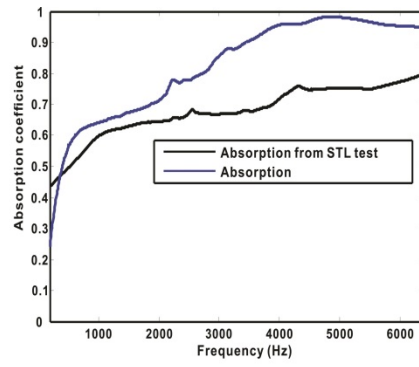
The SAC of the honeycomb metamaterial with the glass fiber inserted was tested under both methods. The STL and SAC results for different arrangements can be shown from Figure 3.14. The STL dip that indicates the resonant frequency can be found at almost 2000 Hz in Figure 3.14 (1a). The dip discrepancy between the high frequency and low frequency results from circumference boundary condition of the sample, which has been stated above that the STL result is sensitive to the boundary condition. Figure 3.14 (1b) shows the absorptive property of the membrane and it can be noticed that nearly 50% sound can be absorbed at the resonant frequency. The absorption coefficient of membrane-type acoustic metamaterial cannot exceed 50% when the incident wave comes from one side only [86], which indicates that only half of energy is available to dissipate. Since the most incoming energy transmission happened at the resonance, nearly half of it is absorbed by the membrane and half of it transmits through the membrane. Glass fiber which is used as excellent absorptive material shows perfect absorption performance especially in high frequency

range, shown in Figure 3.14 (1b). Because the glass fiber was trimmed and inserted into each cell of the honeycomb core and the boundary condition is induced from the rigid honeycomb sample results in the discrepancy from the two curves between the two methods. STL of the glass fiber shown in Figure 3.14 (1a) gradually increased with frequency^[120]. The dip frequency at round 4000 Hz due to the resonance denotes the STL dip and the SAC tip. The trimmed glass fiber configuration changes the position of the resonance. Face sheets are two rigid carbon fiber plates. The sound can be reflected extraordinarily when hitting on the rigid surface which gives excellent STL in Figure 3.14 (1a) and poor SAC in (1b). Two components were arranged in pairs and the corresponding results are shown Figure 3.14(d)-(f). Only 20% sound energy was absorbed when the face sheets were applied while the STL was improved due to glass fiber and the membrane. Figure 3.14(g) shows the whole configuration that the glass fiber is applied to the honeycomb metamaterial with face sheets. The STL can achieve to 75 dB which is great value for sound proof.

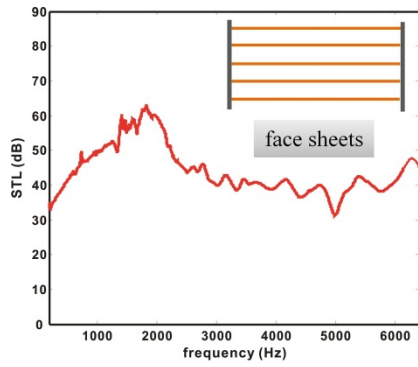




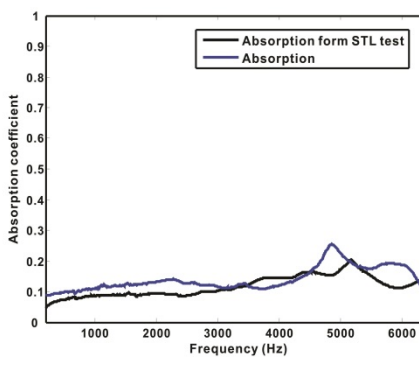
(b1)



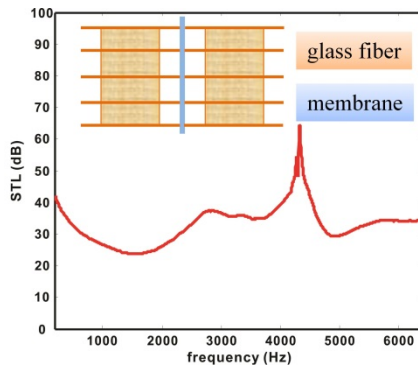
(b2)



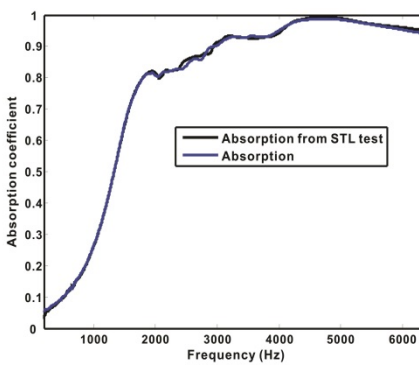
(c1)



(c2)



(d1)



(d2)

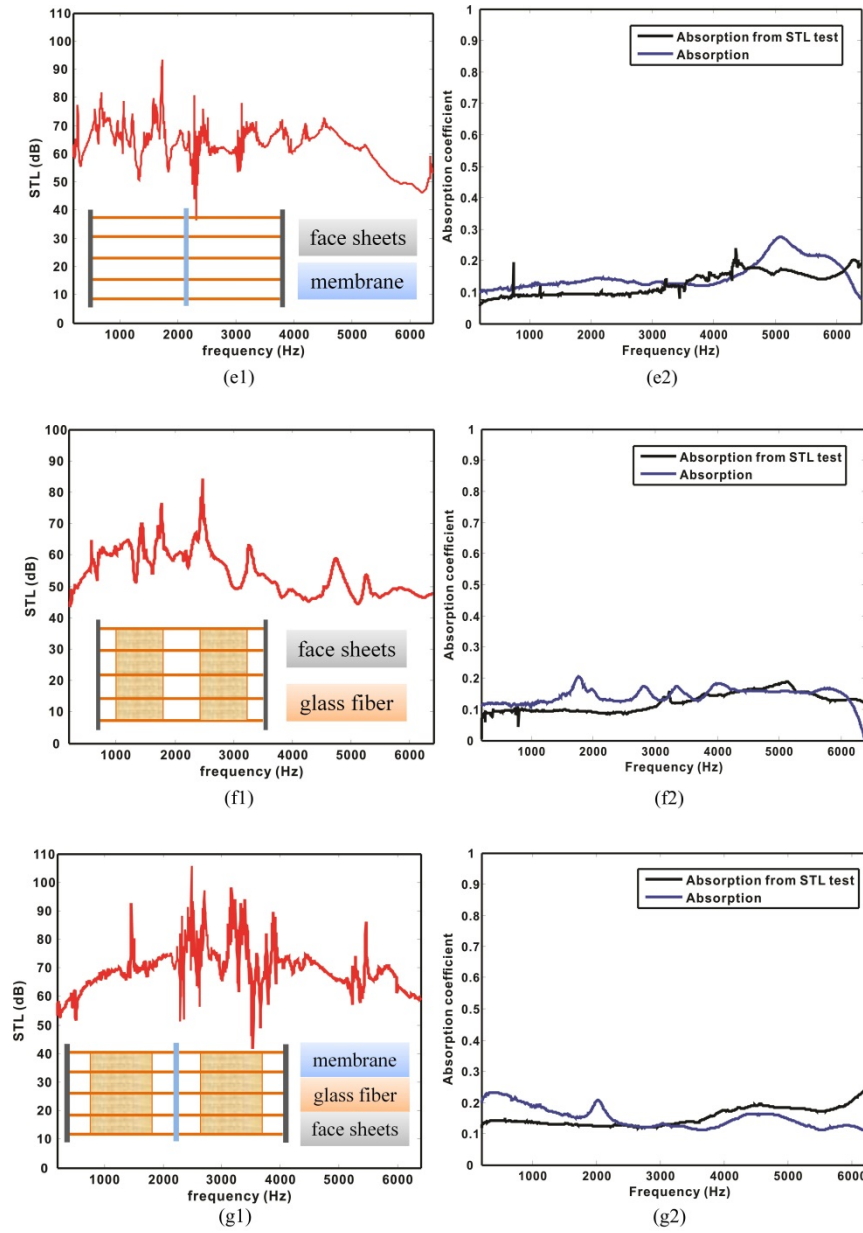


Figure 3.14 STL and SAC experimental results: (a) membrane; (b) glass fiber; (c) face sheets; (d) membrane and glass fiber; (e) membrane and face sheets; (f) glass fiber and face sheets; (g) membrane, glass fiber and face sheets.

The total STL and SAC results can be seen in Figure 3.15 and Figure 3.16, which shows contribution of different component arrangements to the sound proof properties in the structure. From Figure 3.15, the honeycomb metamaterial introducing the membrane can effectively improve the STL of the glass fiber inserted and it can achieve average 80 dB STL. The face sheets used as rigid surface dominated the sound reflection especially at low frequency range leading to high STL. The STLs of the membrane presented better results than that of the glass fiber below the first resonance of the membrane (round 2000 Hz) and above the resonance of the glass fiber (round 4000 Hz). The STLs were increased by 5- 15 dB and this was because the membrane reflected the large amount of sound energy leading to better STL. Based on the honeycomb sandwich panel, the membrane and/or the glass fiber can extremely increase STL without consuming much add-on weight.

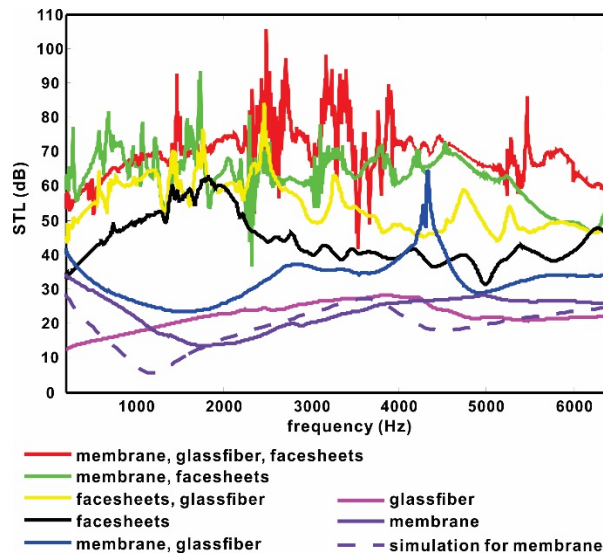


Figure 3.15 STL experimental results of different component arrangements of the structure.

Figure 3.16 shows the sound absorption performance of the structural components. The curves are all taken from the two microphone method that can provide more stable results of SAC. Only 20% sound can be absorbed once the face sheets were applied since the face sheets can block most of the sound energy easily due to the rigid surface. So there are less sound energy can transmit through the face sheet. If the face sheets are not considered in the structure, shown as the red, blue and black curves, the glass fiber has excellent absorptive property compared with membrane. Glass fiber increased the viscous losses of air and sound energy dissipated due to the frictional forces between the air and the fiber which converted the sound energy to heat. On the other hand, the sound waves transmitted only through the pores and decreased the passageways available to propagate. Therefore the glass fiber can efficiently dampen the sound. It is also noted that when membrane is applied with the glass fiber, the glass fiber has excellent sound absorption performance at low frequencies. This phenomenon resulted from the sound reflection of the membrane due to the negative effective mass density.

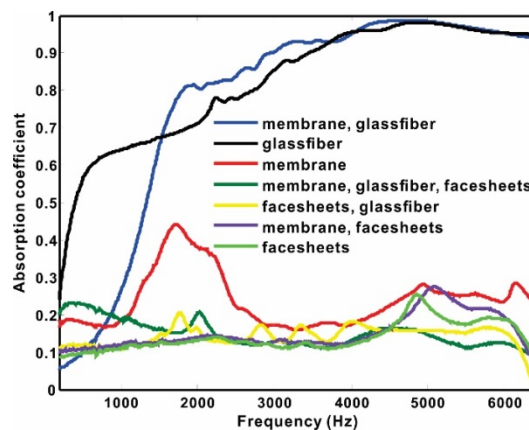


Figure 3.16 SAC experimental results of different component arrangements of the structure.

3.3 Discussion

The proposed honeycomb metamaterial consisting of an array of cellular units with membranes can possess a high STL particular at low frequency range with minimum mass penalty. Since the honeycomb core can be considered as relatively rigid material with respect to the membrane, each unit has a perfect boundary condition contributed by the hexagonal honeycomb core. The constraint boundary condition that is a perfectly clamped membrane all around its edges can produce the relatively strong resonance and yield enhanced STL below the resonant frequencies. However, if the panel is scaled up to a large size sample, the resonance frequency of the panel is dominated by the total mass. The high STL of small sample which can be observed at low frequencies (stiffness-control region) will disappear in the large sample since the resonance frequency reduces dramatically. In other words, if the grid frames become limp, the boundary condition cannot provide clamped edges. Thus the effect of the boundary condition on STL will be studied in this section.

The shape of the unit cell was changed from hexagon to square with the same side length of 3.65 mm in order to reduce the calculation complexity. The size of the panel was considered and designed as 10×10 , 30×30 and 50×50 unit-cell panel respectively. Each panel had been applied clamped boundary condition at the outer edge. The parameters were kept the same as the honeycomb metamaterial except by changing the stiffness of the frame. The material of grid-like frame was basically given as aluminum with 69000 MPa of Young's modulus and the value was decreased to 2000 MPa, 200 MPa and eventually 20 MPa. The damping was still included with 0.2 loss factor. All the simulations were conducted by COMSOL.

The STLs of the 10×10 , 30×30 and 50×50 unit-cell panels are shown in Figure 3.17, Figure 3.18 and Figure 3.19. From these figures, it is observed that more STL dips come out in lower frequency range with decreasing the Young's modulus of the frame. The stiffer material that introduced clamped boundary condition can achieve high STL in low frequencies. The limper the frame is, the more sound will transmit through the panel. As the panel scaled up from 100 unit cells to 2500 unit cells, the frame stiffness effect increases dramatically and the STL curves became unstable compared with small panel. The weaker constraints on each unit cell and the larger panel can induce more vibration modes so there are more resonance coming out in low frequencies. The damping had better effect on relatively high frequencies and can be observed by comparing Fig (a) with Fig (b) from Figure 3.17, 3.18 and 3.19.

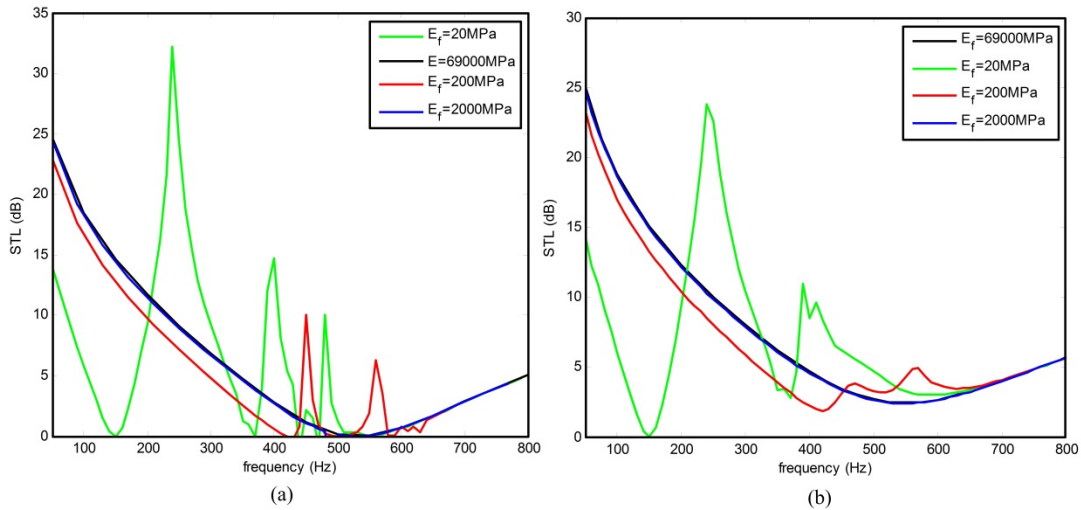


Figure 3.17 The STLs of the 10×10 panel with different Young's modulus of frame (a) without damping case; (b) with damping case.

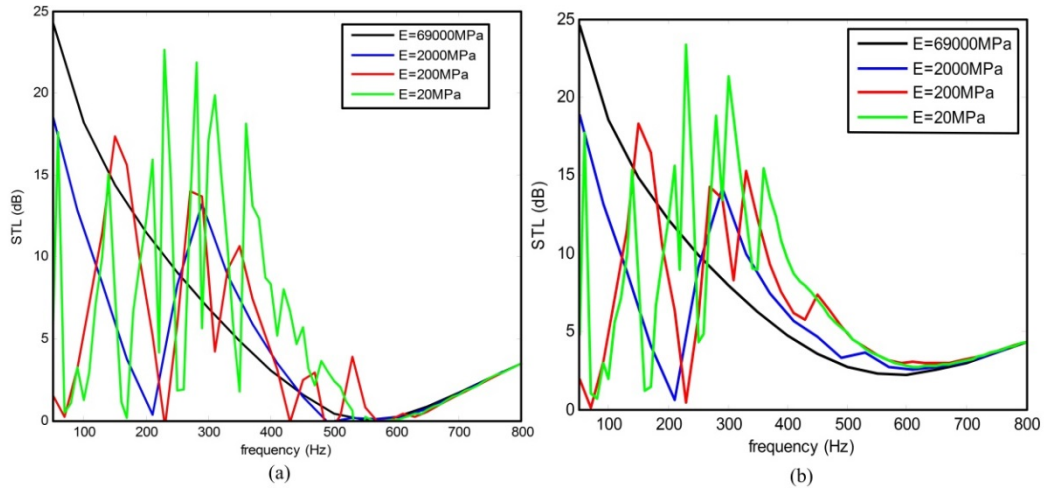


Figure 3.18 The STLs of the 30×30 panel with different Young’s modulus of frame (a) without damping case; (b) with damping case.

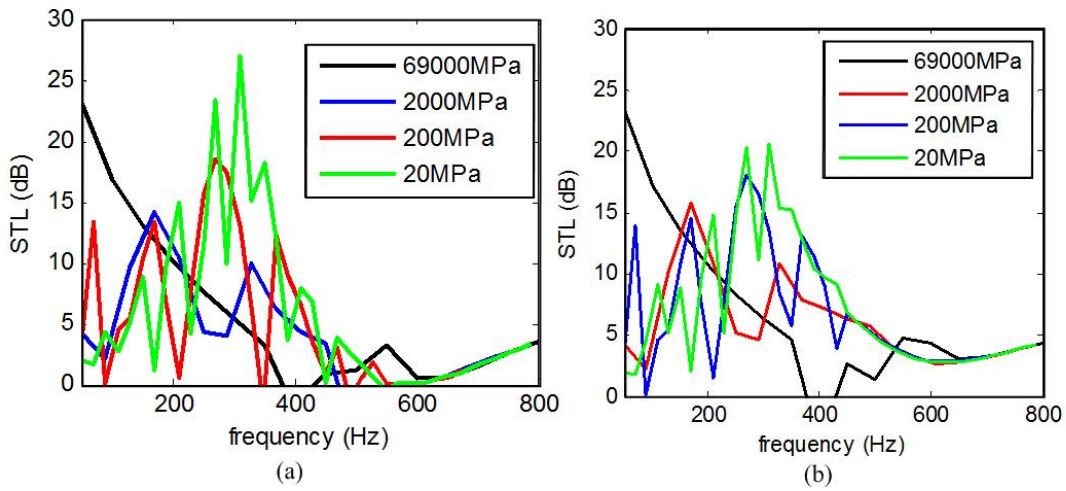


Figure 3.19 The STLs of the 50×50 panel with different Young’s modulus of frame (a) without damping case; (b) with damping case.

The STL with no damping applied are compared only between 10×10 and 30×30 samples because of the stable results and smoother curves shown in Figure 3.20. The STLs got good agreement when the Young’s modulus is 69000 MPa for both panels. This is because the

frame is rigid enough to constrain each unit cell. But as the Young's modulus decreased, more resonance happened in lower frequency which introduced poorer STL. Larger panel lead more resonance as well under the same value of Young's modulus. Therefore, the size of the panel and the stiffness of the frame have great effect on the STL of grid-like frame structures for sound attenuation.

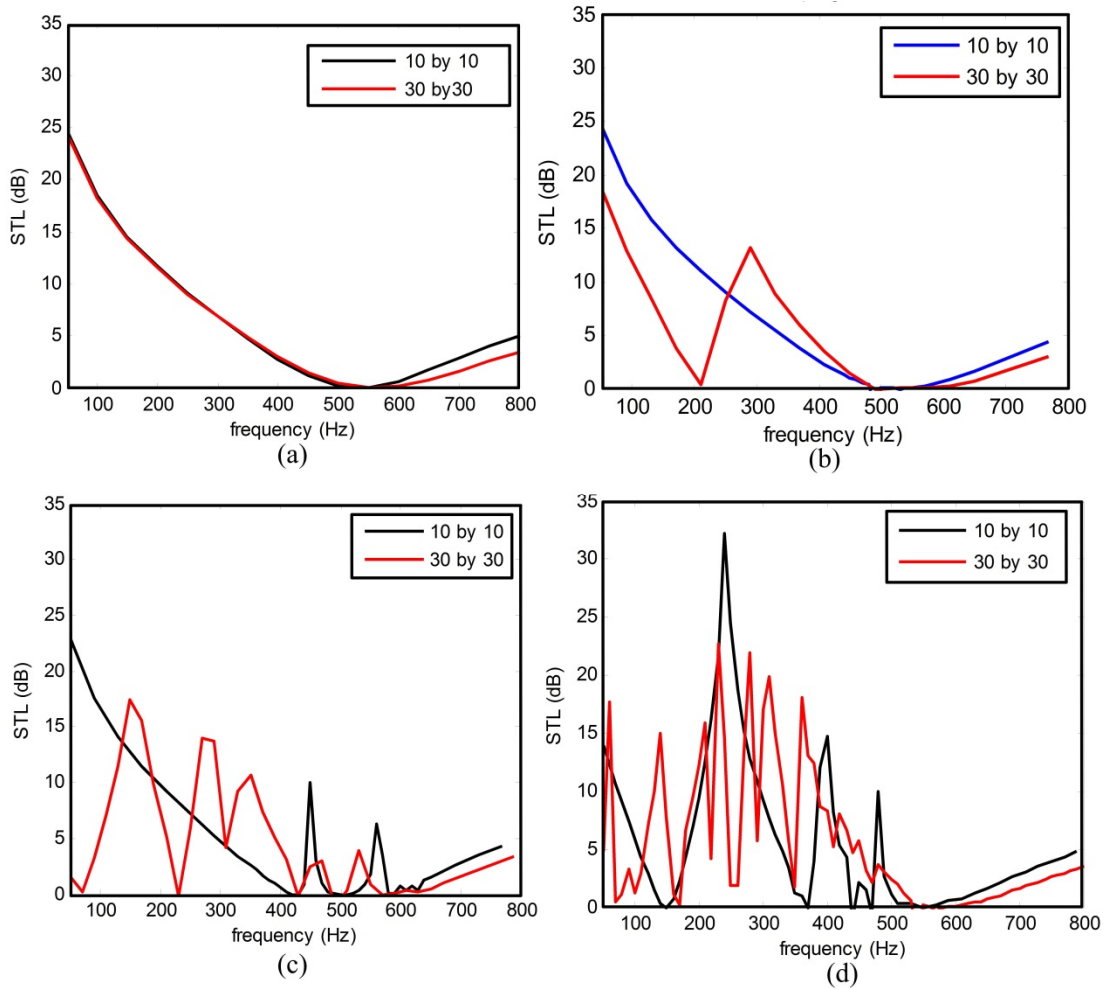


Figure 3.20 The STL comparison of the 10×10 and 30×30 panel with different Young's modulus of frame (a) $E_f = 69000$ MPa; (b) $E_f = 2000$ MPa; (c) $E_f = 200$ MPa; (d) $E_f = 20$ MPa.

3.4 Summary

In this chapter, a lightweight and yet sound-proof honeycomb acoustic metamaterial is designed and experimentally demonstrated. The use of no-mass-attached membrane-type acoustic metamaterials leads to excellent acoustic performance with minimum weight-penalty. The proposed metamaterial having remarkably small mass per unit area at 1.3 kg/m^2 can achieve low frequency ($<500 \text{ Hz}$) STL consistently greater than 45 dB. The sandwich panel which incorporates the honeycomb metamaterial as the core material yields a STL that is consistently greater than 50 dB at low frequencies. Furthermore, the glass fiber reinforcement has excellent sound absorbing performance at high frequencies without adding too much mass. Finally, the stiffness of the grid-like frame and the size of the panel can affect the STL at low frequencies.

Chapter 4

The Helmholtz resonator in a semi-infinite panel

Low frequency sound absorption has great challenge to manipulate by using perfect sound absorber device with some talented advantages: lightweight, minimum thickness with respect to wavelength, comparatively simple configuration, and little modification mating with the originally existing structures. A perfect sound absorber sandwich panel with coupled HRs is the ultimate goal that can achieve total low-frequency sound absorption with sandwich panel design.

In this chapter, the basic theory of sound absorption mechanism for single unit cell HR has been elaborated by solving Kirchhoff-Helmholtz integral in a semi-infinite space bounded by a rigid plate. Two types of HR unit cells are proposed: one is the single HR and the other one is dual HRs with different orifice diameters. In order to analyze the sound absorption capability of HRs in semi-infinite rigid plane, the sound propagation with pressures and the corresponding acoustic impedances are demonstrated. The critical coupling between two HRs is proposed. Moreover, the dissipated sound energy in HRs is calculated thanks to the one dimensional vibration analogy model of HR.

Classic HR is one of the effective passive noise attenuation devices. It consists of an air cavity with the radius a_c and the height l_c and a neck (or orifice) with the radius a_0 and the length l respectively, shown in Figure 4.1 (a). The classic model of HR can be simplified as a single freedom mass spring vibration system that can (the reason why it can be used as lump model) be shown in Figure 4.1 (b). The walls of the resonator are well approximated as acoustically rigid. The air in the cavity can be compressed or elongated so it is used as the spring of the system. The main part of the mass is contributed by the air in the orifice; there are another two parts of mass generated by the abrupt change of the cross sections shown as

external mass end correction l_{ex} and internal mass end correction l_{in} when the system vibrates.

A damper in the system is caused by the radiation and the thermal-viscous forces.

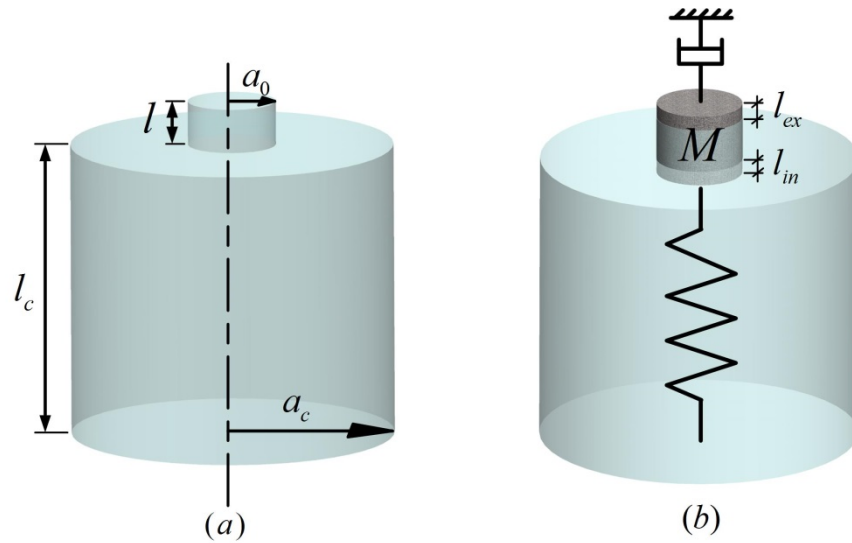


Figure 4.1 Classic single Helmholtz resonator: (a) resonator sketch; (b) vibration analogy model.

In this chapter, the perfect sound absorber panel based on periodically arranged HRs is theoretically proved by using only single unit cell HR and dual HRs with two different orifice radiuses in a semi-infinite rigid panel. The sound absorption mechanism and the corresponding parameters of the HRs are provided, which gives the basic tutorial for HR based perfect sound absorber sandwich panel design.

4.1 The single Helmholtz resonator in a semi-infinite rigid panel

A single Helmholtz resonator (HR) is embedded in a semi-infinite rigid panel, shown as Figure 4.2, and the geometry parameters refer to Figure 4.1. In the following the sound absorbing property for the single Helmholtz resonator mounted in a rigid panel (or in a rigid

sandwich panel) is examined first. For the single HR, the top and bottom surfaces are separated by the cylindrical HR cavity with a radius a_c and the orifice connects the cavity with the air out of the panel. l is the thickness of the top face sheet if the HR is in the sandwich panel or it represents the length of the orifice. Since all the surfaces can be used as the hard boundaries, the orifice is the only contribution to sound absorption on the panel surface.

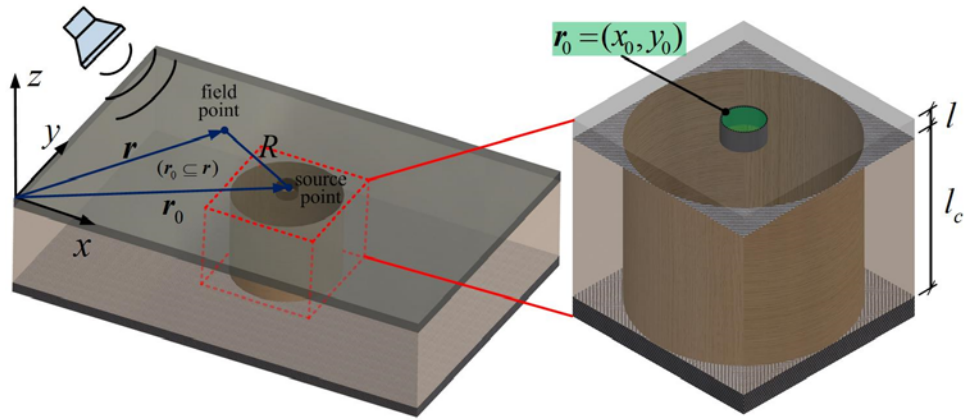


Figure 4.2 A single HR is embedded in the panel with plane wave incidence.

A traveling incident plane wave impinges on the panel surface which located on the x - y plane can be expressed by

$$p_{\text{in}} = P e^{i(\mathbf{k} \cdot \mathbf{r} - \omega t)} \quad (4.1)$$

where P is the amplitude of incident wave; $\mathbf{k} = k\mathbf{n}$ is the wave vector, k is the wavenumber, $\mathbf{n} = \hat{\mathbf{e}}_x \cos \alpha + \hat{\mathbf{e}}_y \cos \beta - \hat{\mathbf{e}}_z \cos \gamma$, and $\mathbf{r} = \hat{\mathbf{e}}_x x + \hat{\mathbf{e}}_y y + \hat{\mathbf{e}}_z z$. α , β , and γ are the angle between

the normal of the wave front and the x, y, z axis, respectively. ω is the angular frequency. Eq. (4.1) can be simplified by omitting the time-harmonica term $e^{-i\omega t}$ and written as

$$p_{\text{in}} = P e^{ik(x \cos \alpha + y \cos \beta - z \cos \gamma)} \quad (4.2)$$

When the incident wave impinges on the face sheet, shown as Figure 4.2, part of the waves are reflected by the panel and the rest of them are absorbed by HR. Assuming that the face sheets are rigid and processed as the hard boundary, the sound pressure value at the surface of the top face sheet turns to twice the incident pressure of p_{in} and the sound wave cannot transmit through the structure since the hard boundary gives the total reflection. The incident plane wave can be imagined originating from a distant point source. Thus, using the Green's function G_N for a semi-infinite space bounded by a rigid plane (top face sheet), the sound pressure p generated on the panel surface (x - y plane) in terms of Kirchhoff-Helmholtz integral equation can be described as

$$p(x, y) = 2p_{\text{in}}(x, y) + p_r(x, y) \quad (4.3a)$$

$$p_r(x, y) = -ik \rho_0 c v \iint_S G_N(\mathbf{r} | \mathbf{r}_0) dS \quad (4.3b)$$

where ρ_0 is air density; c is sound velocity in the air; v is the orifice velocity (velocity is taken positive along the positive z direction); and S is orifice area. $\mathbf{r} = (x, y)$ and $\mathbf{r}_0 = (x_0, y_0)$ are denoted as field points on the face sheet surface and source points on orifice surface respectively. The relation between these two group points is $\mathbf{r}_0 \subseteq \mathbf{r}$. The Green's function G_N for a semi-infinite space bounded by a rigid plane is written as

$$G_N = \frac{e^{ikR}}{2\pi R}, \text{ with } R = \sqrt{(x - x_0)^2 + (y - y_0)^2} \quad (4.4)$$

The pressure on any point of the surface $p(x, y)$ is determined by the pressure induced by a source which is $2p_{\text{in}}(x, y)$ and the sound field generated by the orifice boundary condition which is the radiation sound pressure $p_r(x, y)$. In this problem, the surface of rigid panel everywhere has zero velocity except the orifice. The surface integral is thereby restricted by the orifice surface induced by the piston-like motion from the air mass in the neck region.

Simultaneously, the radiation pressure at any point on the panel surface is then

$$p_r(x, y) = \rho_0 c v z_r(x, y) \quad (4.5)$$

which accounts for the pressure scattered (radiated) from the opening, and combining the Eq. (4.3b) and Eq. (4.5) gives

$$z_r(x, y) = -ik \iint_S G(\mathbf{r} | \mathbf{r}_0) dS \quad (4.6)$$

$z_r(x, y)$ is defined as the normalized radiation impedance at any location on the plane surface. According to the definition of radiation impedance, the normalized radiation impedance for the HR can be defined as the ratio of the average pressure a radiator exerts on the orifice surface area A_0 , to the inlet velocity v and is given by

$$z_r = \frac{\iint_S p_r dS}{\rho_0 c A_0 v} = \frac{-ik}{\pi a_0^2} \iint_S \iint_S G_N dS dS \quad (4.7)$$

With the use of spatial Fourier transform, the Green's function G_N can be written as

$$G_N = \frac{1}{4\pi^2} \int_{-\infty}^{\infty} \int_{-\infty}^{\infty} \mathbf{g} \cdot e^{-i(\xi x + \eta y)} d\xi d\eta \quad (4.8a)$$

$$\mathbf{g} = \int_{-\infty}^{\infty} \int_{-\infty}^{\infty} G_N \cdot e^{-i(\xi x + \eta y)} dx dy \quad (4.8b)$$

where

$$\beta = \sqrt{\xi^2 + \eta^2}, \quad \phi = \tan^{-1}(\eta / \xi), \quad R = \sqrt{(x - x_0)^2 + (y - y_0)^2}, \quad \phi = \tan^{-1}\left(\frac{y - y_0}{x - x_0}\right) \quad (4.9)$$

Thus

$$\begin{aligned} g &= \int_{-\infty}^{\infty} \int_{-\infty}^{\infty} \frac{e^{ikR}}{2\pi R} \cdot e^{i(\xi x + \eta y)} dx dy \\ &= e^{i(\xi x_0 + \eta y_0)} \int_0^{\infty} \int_0^{2\pi} \frac{e^{ikR}}{2\pi R} \cdot e^{i\beta r \cos(\phi - \phi)} r d\phi dr \\ &= e^{i(\xi x_0 + \eta y_0)} \int_0^{\infty} e^{ikr} J_0(\beta r) dr \\ &= e^{i(\xi x_0 + \eta y_0)} \left\{ \int_0^{\infty} \cos(kr) J_0(\beta r) dr + i \int_0^{\infty} \sin(kr) J_0(\beta r) dr \right\} \\ &= \frac{e^{i(\xi x_0 + \eta y_0)}}{\sqrt{\beta^2 - k^2}} \end{aligned} \quad (4.10a)$$

and

$$G_N(\mathbf{r} | \mathbf{r}_0) = \frac{1}{4\pi^2} \int_{-\infty}^{\infty} \int_{-\infty}^{\infty} \frac{e^{-i[\xi(x-x_0) + \eta(y-y_0)]}}{\sqrt{\xi^2 + \eta^2 - k^2}} d\xi d\eta \quad (4.10b)$$

Substituting Eq. (4.10b) into Eq. (4.7) gives

$$\begin{aligned} z_r &= \frac{-ik}{\pi a_0^2} \iint_S \iint_S \left(\frac{1}{4\pi^2} \int_{-\infty}^{\infty} \int_{-\infty}^{\infty} \frac{e^{-i[\xi(x-x_0) + \eta(y-y_0)]}}{\sqrt{\xi^2 + \eta^2 - k^2}} d\xi d\eta \right) dS dS \\ &= \frac{-ik \rho_0 c v}{\pi a_0^2} \cdot \frac{1}{4\pi^2} \int_{-\infty}^{\infty} \int_{-\infty}^{\infty} \frac{d\xi d\eta}{\sqrt{\xi^2 + \eta^2 - k^2}} \iint_S e^{-i(\xi x + \eta y)} dS \iint_S e^{i(\xi x_0 + \eta y_0)} dS \end{aligned} \quad (4.11)$$

where

$$\iint_S e^{-i(\xi x + \eta y)} dS = \pi a_0^2 \frac{2J_1(a_0 \sqrt{\xi^2 + \eta^2})}{a_0 \sqrt{\xi^2 + \eta^2}} e^{-i(\xi x_c + \eta y_c)} \quad (4.12a)$$

$$\iint_S e^{i(\xi x_0 + \eta y_0)} dS = \pi a_0^2 \frac{2J_1(a_0 \sqrt{\xi^2 + \eta^2})}{a_0 \sqrt{\xi^2 + \eta^2}} e^{i(\xi x_c + \eta y_c)} \quad (4.12b)$$

and (x_c, y_c) is the orifice center coordinate. Thus Eq. (4.11) can be further simplified as

$$\begin{aligned} z_r &= \frac{-ik}{\pi a_0^2} \cdot \frac{1}{4\pi^2} \int_{-\infty}^{\infty} \int_{-\infty}^{\infty} \frac{4\pi^2 a_0^2}{\sqrt{\xi^2 + \eta^2 - k^2}} \frac{J_1^2(a_0 \sqrt{\xi^2 + \eta^2})}{\xi^2 + \eta^2} d\xi d\eta \\ &= \frac{-ik}{\pi} \int_{-\infty}^{\infty} \int_{-\infty}^{\infty} \frac{1}{\sqrt{\xi^2 + \eta^2 - k^2}} \frac{J_1^2(a_0 \sqrt{\xi^2 + \eta^2})}{\xi^2 + \eta^2} d\xi d\eta \\ &= \frac{-ik}{\pi} \int_0^{\infty} \int_0^{2\pi} \frac{1}{\sqrt{\beta^2 - k^2}} \frac{J_1^2(a_0 \beta)}{\beta^2} \beta d\varphi d\beta \\ &= -2ik \int_0^{\infty} \frac{1}{\sqrt{\beta^2 - k^2}} \frac{J_1^2(a_0 \beta)}{\beta^2} \beta d\beta \\ &= -2k \int_0^{\infty} \frac{1}{\sqrt{k^2 - \beta^2}} \frac{J_1^2(a_0 \beta)}{\beta^2} \beta d\beta \\ &= -2k \int_0^{\infty} [J_1(a_0 \beta)]^2 \frac{d\beta}{\beta \sqrt{k^2 - \beta^2}} \\ &= -k \left\{ \int_0^k [J_1(a_0 \beta)]^2 \frac{d\beta}{\beta \sqrt{k^2 - \beta^2}} - \int_k^{\infty} [J_1(a_0 \beta)]^2 \frac{d\beta}{\beta \sqrt{k^2 - \beta^2}} \right\} \\ &= 1 - \frac{J_1(2ka_0)}{ka_0} - i \frac{H_1(2ka_0)}{ka_0} \end{aligned} \quad (4.13)$$

where J_n represents the Bessel function of first kind of order n , and $H_1(2ka_0)$ denotes the Struve function of order one and argument $2ka_0$.

Therefore, from Eq. (4.13), the normalized specific radiation impedance of a plane piston in a baffle plane can be specified as

$$z_r = r_r + ix_r \quad (4.14)$$

where r_r is the specific radiation *resistance* and x_r is the specific radiation *reactance*. If long wavelength assumption is assumed, that is, $ka_0 \ll 1$, the specific radiation resistance and reactance are then simplified from Eq. (4.14) as

$$r_r = 1 - \frac{J_1(2ka_0)}{ka_0} \approx \frac{1}{2}(ka_0)^2 \quad (4.15a)$$

$$x_r = -\frac{H_1(2ka)}{ka} \approx -k\left(\frac{8a_0}{3\pi}\right) = -kl_{ex} \quad (4.15b)$$

where $l_{ex} = 8a_0 / 3\pi$ is often referred to as the external mass end correction, shown in Figure 4.1.

The total average pressure $p(x, y)$ at the HR orifice surface can also be conveniently expressed as

$$p^{avg}(x, y) = -v(\rho_0 c)Z_i \quad (4.16)$$

where Z_i is defined as the normalized input impedance and for a HR with both cylindrical neck and cavity, it can be written as

$$Z_i = Z_{neck} + Z_{cavity} + Z_{visc} + Z_{therm} \quad (4.17)$$

Z_{neck} is the neck normalized impedance that stands for impedance of air mass in the orifice and can be calculated by including the internal end correction as

$$Z_{neck} = -ik(l + l_{in}) \quad (4.18)$$

where $l_{in} \approx [1 - (a_0/a_c)^2]l_{ex}$ is the internal end correction; a_0 , a_c and l are the neck radius, cavity radius and the neck length respectively and shown in Figure 4.1.

z_{cavity} , indicating the normalized impedance from air in the cavity, is characterized by analogues “spring” and given by

$$z_{cavity} = ik \left(\frac{a_0}{a_c} \right)^2 \cot(kl_c) \quad (4.19)$$

where l_c the cavity length.

Based on long wavelength assumption, the air in the orifice and cavity can be modelled as mass and spring, respectively, and thus only contribute to the reactive part of the impedance.

The impedance resulting from viscous boundary layer z_{visc} depends on viscous friction between the air mass and the HR walls including the interior orifice wall and the top and bottom surfaces that are in the vicinity of the orifice due to the shear flow with tangential velocity along these walls. The complex shear stress amplitude is given by

$$\tau = -\mu i k_v v = \nu(1-i)\mu / \delta_v \quad (4.20)$$

where μ is the coefficient of shear viscosity, $k_v = (1+i)\sqrt{\rho_0\omega / 2\nu}$ is the propagation constant, $\delta_v = \sqrt{2\nu / \omega}$ is the viscous boundary layer thickness, and ν is the kinematical viscosity of air ($\nu \approx 15 \times 10^{-6} m^2 / s$). Thus the corresponding normalized shear viscous impedance is calculated as

$$\begin{aligned} z_{visc} &= \tau \cdot 2\pi a_0 (l + l_{in} + l_{ex}) / (\pi a_0^2 \rho_0 c \nu) \\ &= k \delta_v (1-i) (l + l_{in} + l_{ex}) / a_0 \end{aligned} \quad (4.21)$$

It is observed that besides the length of the interior orifice wall, the internal and external mass end corrections are assumed to be another contribution to the total length of orifice wall.

Z_{therm} is the impedance due to thermal boundary layer

$$Z_{therm} = k(\gamma - 1)\delta_h l / 2a_0 \quad (4.22)$$

where γ is the specific heat ratio, δ_h is the thermal boundary layer thickness and is given as

$$\delta_h = \sqrt{2K / \rho_0 C_p \omega} \approx \frac{0.25 \times 10^{-2}}{\sqrt{f}} \quad (4.23)$$

where K is heat conduction coefficient and C_p is the specific heat per unit mass at constant pressure. The thermal boundary layer only depends on the interior orifice wall.

Combining Eq. (4.17), Eq. (4.18), Eq. (4.19), Eq. (4.21) and Eq. (4.22) together, the normalized input impedance can be expressed as

$$Z_i = r_i + ix_i \quad (4.24)$$

where

$$r_i = k(\gamma - 1)\delta_h l / 2a_0 + k\delta_v l' / a_0 \quad (4.25a)$$

$$x_i = (a_0 / a_c)^2 \cot(kl_c) - k(l + l_{in}) - k\delta_v l' / a_0 \quad (4.25b)$$

and $l' \equiv l + l_{in} + l_{ex}$. r_i and x_i are normalized input resistance and reactance, respectively.

The total specific normalized input impedance of HR is newly defined by incorporating the imaginary part of the normalized radiation impedance into the Eq. (4.24) as

$$Z_{HR} = Z_i - ikl_{ex} \quad (4.26)$$

Therefore, it is obvious from Eq. (4.25a) that the sound absorbing is solely caused by the viscous and thermal loss at the orifice walls which are given by the resistive part; while the cavity air, the orifice mass and the viscous layer provide reactance for the HR.

The total sound absorption energy that can be dissipated by HR is defined as the absorbed power W_a and given by

$$\begin{aligned}
 W_a &= \frac{1}{2} \text{Re}(p \cdot v^*) \pi a_0^2 \\
 &= \frac{1}{2} \rho_0 c \text{Re}\{z_i\} \cdot |v|^2 \pi a_0^2 \\
 &= \frac{1}{2} \text{Re}\{z_i\} \frac{|2p_{ia}|^2}{|z_r + z_i|^2 \rho_0 c} \pi a_0^2 \\
 &= \pi a_0^2 \frac{4r_i}{|z_r + z_i|^2} \cdot I_{inc}
 \end{aligned} \tag{4.27}$$

where $I_{inc} = \frac{|p_{ia}|^2}{2\rho_0 c}$ is the incident acoustic intensity.

At resonant frequency, the reactive part of the total normalized impedance vanishes, i.e.,

$$x_i + x_r = 0 \text{ at resonance} \tag{4.28}$$

Therefore, the absorbed energy at resonant is

$$W_a = \frac{2\lambda^2}{\pi} \frac{r_i r_r}{|r_i + r_r|^2} I_{inc} \text{ at resonance} \tag{4.29}$$

The maximum absorption energy is deduced as

$$W_{a,max} = \frac{\lambda^2}{2\pi} I_{inc} \text{ at resonance, if } r_i = r_r \tag{4.30}$$

The frequency response of the absorbed energy can be evaluated through examine the sharpness of resonance, i.e., the Q -factor. The single HR in a rigid panel is analogous to a

one-dimensional vibration system (shown in Figure 4.3). Thus, the Q -factor can be readily defined as

$$Q = 2\pi f_0 (M_{in} + M_r) / (R_{in} + R_r) \quad (4.31)$$

where f_0 is the system resonant frequency, M_{in} and M_r are the mass elements, R_{in} and R_r are the damping elements and C_{in} is the compliance. M_{in} and M_r resemble the orifice reactance x_i and the radiation reactance x_r , respectively, R_{in} and R_r are equivalent to the orifice resistance and the radiation resistance, respectively. The Q factor determines the bandwidth of the frequency response and a Q -factor is desired to obtain a wider bandwidth.

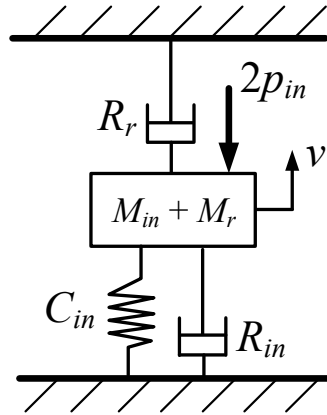


Figure 4.3 One-dimensional vibration system analogy to the single HR on a rigid plane.

4.2 Coupled dual Helmholtz resonators in a semi-infinite rigid panel

If two HRs with different orifice radiuses are considered as the one unit cell of the sandwich panel, dual HRs themselves in the panel or a sandwich panel, as shown in Figure 4.4, are primarily introduced in order to guide the sound absorption in whole sandwich panel. The total pressure on the panel surface (x - y plane) can now be expressed as

$$p(x, y) = 2p_{in}(x, y) - ik\rho_0 c \sum_{j=1}^2 v_j \iint_{S_j} G(\mathbf{r}|\mathbf{r}_0) dS_j \quad (4.32)$$

$p_r(x, y)$

where the subscript j represents the index of orifice, S_j the orifice area, and v_j the orifice velocity.

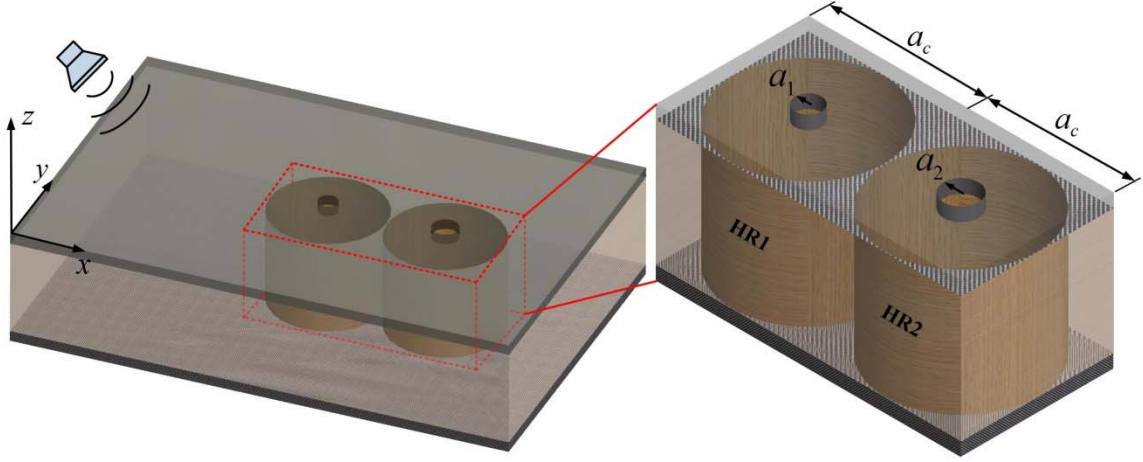


Figure 4.4 The coupled dual HRs embedded in the semi-infinite panel.

The sound radiation pressure is obtained by the summation of two orifices. For any orifice denoting as HR_h , the normalized impedance can be obtained by taking average value of corresponding pressure on the orifice area S_h . Thus, the average sound pressure exerted on any orifice is the same as the pressure at the center of the orifice (x_c, y_c) . The Eq. (4.32) can be rewritten as

$$p_h^{avg} = 2p_{in,h}^{avg} + \frac{\iint_{S_h} -ik\rho_0 c \sum_{j=1}^2 v_j \iint_{S_j} G(\mathbf{r}|\mathbf{r}_0) dS_j dS_h}{S_h} \quad (4.33)$$

Recall $p_r^{avg} = Z_{r,h} v_h \rho_0 c$, the normalized radiation impedance for orifice h can be expressed from Eq. (4.33) as

$$Z_{r,h} = \frac{-ik \sum_{j=1}^2 v_j \iint_{S_h} \iint_{S_j} G(\mathbf{r}|\mathbf{r}_0) dS_j dS_h}{v_h S_h} \quad (4.34)$$

$Z_{r,h}$ is defined as normalized net radiation impedance for any orifice h . The acoustic impedance of any HR is affected by both itself and other orifice. The mutual impedance is defined to interpret the coupling between orifice j and h as

$$Z_r^{h,j} = \frac{-ik}{S_h} \iint_{S_h} \iint_{S_j} G(\mathbf{r}|\mathbf{r}_0) dS_j dS_h \quad (4.44)$$

If $h=1$, Eq. (4.34) and Eq. (4.44) yield the normalized net radiation impedance:

$$Z_{r,1} = Z_{1,1} + Z_{1,2} \cdot \frac{v_2}{v_1} \quad (4.45)$$

The radiation impedance of any orifice is caused by self-radiation impedance and the mutual radiation impedance with respect of the velocity ratio between the two orifices.

Similar to the derivation of normalized self-radiation impedance, with the use of spatial Fourier transform, the Green's function G_N can be written as

$$G_N(\mathbf{r}|\mathbf{r}_0) = \frac{1}{4\pi^2} \int_{-\infty}^{\infty} \int_{-\infty}^{\infty} g \cdot e^{-i(\xi x + \eta y)} d\xi d\eta \quad (4.46a)$$

$$g = \int_{-\infty}^{\infty} \int_{-\infty}^{\infty} G_N(\mathbf{r}|\mathbf{r}_0) \cdot e^{i(\xi x + \eta y)} dx dy \quad (4.46b)$$

where

$$\beta = \sqrt{\xi^2 + \eta^2}, \quad \varphi = \tan^{-1}(\eta / \xi), \quad r = \sqrt{(x - x_0)^2 + (y - y_0)^2}, \quad \phi = \tan^{-1}\left(\frac{y - y_0}{x - x_0}\right) \quad (4.46c)$$

Thus

$$\begin{aligned}
g &= \int_{-\infty}^{\infty} \int_{-\infty}^{\infty} \frac{e^{ikR}}{2\pi R} \cdot e^{i(\xi x + \eta y)} dx dy \\
&= e^{i(\xi x_0 + \eta y_0)} \int_0^{\infty} \int_0^{2\pi} \frac{e^{ikR}}{2\pi R} \cdot e^{i\beta r \cos(\phi - \varphi)} r d\phi dr \\
&= e^{i(\xi x_0 + \eta y_0)} \int_0^{\infty} e^{ikr} J_0(\beta r) dr \\
&= e^{i(\xi x_0 + \eta y_0)} \left\{ \int_0^{\infty} \cos(kr) J_0(\beta r) dr + i \int_0^{\infty} \sin(kr) J_0(\beta r) dr \right\} \\
&= \frac{e^{i(\xi x_0 + \eta y_0)}}{\sqrt{\beta^2 - k^2}}
\end{aligned} \tag{4.47a}$$

and

$$G_N(\mathbf{r} | \mathbf{r}_0) = \frac{1}{4\pi^2} \int_{-\infty}^{\infty} \int_{-\infty}^{\infty} \frac{e^{-i[\xi(x-x_0) + \eta(y-y_0)]}}{\sqrt{\xi^2 + \eta^2 - k^2}} d\xi d\eta \tag{4.47b}$$

Substituting Eq. (4.47b) into Eq. (4.44) gives

$$\begin{aligned}
z_r^{h,j} &= \frac{-ik}{\pi a_h^2} \iint_{S_h} \iint_{S_j} \left(\frac{1}{4\pi^2} \int_{-\infty}^{\infty} \int_{-\infty}^{\infty} \frac{e^{-i[\xi(x-x_0) + \eta(y-y_0)]}}{\sqrt{\xi^2 + \eta^2 - k^2}} d\xi d\eta \right) dS_j dS_h \\
&= \frac{-ik}{\pi a_h^2} \cdot \frac{1}{4\pi^2} \int_{-\infty}^{\infty} \int_{-\infty}^{\infty} \frac{d\xi d\eta}{\sqrt{\xi^2 + \eta^2 - k^2}} \iint_{S_h} e^{-i(\xi x + \eta y)} dS_h \iint_{S_j} e^{i(\xi x_0 + \eta y_0)} dS_j
\end{aligned} \tag{4.48}$$

where

$$\iint_{S_h} e^{-i(\xi x + \eta y)} dS_h = \pi a_h^2 \frac{2J_1(a_h \sqrt{\xi^2 + \eta^2})}{a_h \sqrt{\xi^2 + \eta^2}} e^{-i(\xi x_{c,h} + \eta y_{c,h})} \tag{4.49a}$$

$$\iint_{S_j} e^{i(\xi x_0 + \eta y_0)} dS_j = \pi a_j^2 \frac{2J_1(a_j \sqrt{\xi^2 + \eta^2})}{a_j \sqrt{\xi^2 + \eta^2}} e^{i(\xi x_{c,j} + \eta y_{c,j})} \tag{4.49b}$$

The distance between the two orifice centers is given by

$$r_{h,j} = \sqrt{(x_{c,h} - x_{c,j})^2 + (y_{c,h} - y_{c,j})^2}, \phi_{h,j} = \tan^{-1} \left(\frac{y_{c,h} - y_{c,j}}{x_{c,h} - x_{c,j}} \right) \quad (4.49c)$$

Eq. (4.48) can be further simplified as

$$\begin{aligned} z_r^{h,j} &= \frac{-ika_j a_h}{\pi a_j^2} \cdot \int_{-\infty}^{\infty} \int_{-\infty}^{\infty} \frac{e^{-i(\xi(x_{c,h} - x_{c,j}) + \eta(y_{c,h} - y_{c,j}))}}{\sqrt{\xi^2 + \eta^2 - k^2}} \frac{J_1(a_j \sqrt{\xi^2 + \eta^2}) J_1(a_h \sqrt{\xi^2 + \eta^2})}{\xi^2 + \eta^2} d\xi d\eta \\ &= \frac{-ika_h}{\pi a_j} \int_0^{\infty} \int_0^{2\pi} \frac{1}{\sqrt{\beta^2 - k^2}} \frac{J_1(a_j \beta) J_1(a_h \beta)}{\beta^2} e^{-i\beta r_{h,j} \cos(\varphi - \phi_{hj})} \beta d\varphi d\beta \end{aligned} \quad (4.50)$$

If the integral expression of the Bessel function is applied on the last term Eq. (4.50), the mutual radiation impedance can be expressed by the following integral form

$$z_r^{h,j} = \frac{2a_h}{a_j} \int_0^{\infty} \frac{-ik}{\sqrt{\beta^2 - k^2}} \frac{J_1(a_j \beta) J_1(a_h \beta) J_0(r_{h,j} \beta)}{\beta} d\beta \quad (4.51)$$

Letting $\beta = k \sin \theta$ and using integration by steps, i.e., $\theta \in [(0, \pi/2) \cup (\pi/2 + i0, \pi/2 + i\infty)]$, Eq. (4.51) can be written as

$$\begin{aligned} z_r^{h,j} &= \mathbf{r}_r^{h,j} + i\mathbf{x}_r^{h,j} \\ &= \frac{2a_h}{a_j} \left[\int_0^{\pi/2} \frac{J_1(a_j k \sin \theta) J_1(a_h k \sin \theta) J_0(r_{h,j} k \sin \theta)}{\sin^2 \theta} \sin \theta d\theta \right. \\ &\quad \left. - \int_{\pi/2+i0}^{\pi/2+i\infty} \frac{J_1(a_j k \sin \theta) J_1(a_h k \sin \theta) J_0(r_{h,j} k \sin \theta)}{\sin^2 \theta} \sin \theta d\theta \right] \end{aligned} \quad (4.52)$$

Mutual Radiation Resistance

The mutual radiation resistance $\mathbf{r}_r^{h,j}$ may be evaluated from Eq. (4.52) by integrating along the real values of θ , where $\theta \in [(0, \pi/2)]$

$$\mathbf{r}_r^{h,j} = \int_0^{\pi/2} \frac{2a_h}{a_j} \left[\frac{J_1(a_j k \sin \theta)}{\sin \theta} \frac{J_1(a_h k \sin \theta)}{\sin \theta} J_0(r_{h,j} k \sin \theta) \sin \theta \right] d\theta \quad (4.53)$$

Substituting $\sin \theta = (1 - \cos^2 \theta)^{1/2}$ into the first terms in the integrand of Eq. (4.53), each term may be expressed as an infinite series by utilizing a Lommel expansion.

$$\begin{aligned} \frac{J_1(a_j k \sin \theta)}{\sin \theta} &= \frac{J_1 \left\{ [(a_j k)^2 - (a_j k)^2 \cos^2 \theta]^{1/2} \right\}}{(1 - \cos^2 \theta)^{1/2}} \\ &= \sum_{m=0}^{\infty} \frac{(a_j k)^m \cos^{2m} \theta}{2^m m!} J_{1+m}(a_j k) \end{aligned} \quad (4.54a)$$

$$\begin{aligned} \frac{J_1(a_h k \sin \theta)}{\sin \theta} &= \frac{J_1 \left\{ [(a_h k)^2 - (a_h k)^2 \cos^2 \theta]^{1/2} \right\}}{(1 - \cos^2 \theta)^{1/2}} \\ &= \sum_{n=0}^{\infty} \frac{(a_h k)^n \cos^{2n} \theta}{2^n n!} J_{1+n}(a_h k) \end{aligned} \quad (4.54b)$$

The series in Eq. (4.54) are then substituted back in Eq. (4.53). The orders of summation and integration are interchanged (since the series are convergent for all finite values of ka_h and ka_j). With the aid of Sonine's integral and performing term by term integration yields,

$$J_{m+n+1/2}(r_{h,j} k) = \frac{(r_{h,j} k)^{m+n+1/2}}{2^{m+n-1/2} \Gamma(m+n+1/2)} \times \int_0^{\pi/2} J_0(r_{h,j} k \sin \theta) \sin \theta \cos^{2m+2n} \theta d\theta \quad (4.55)$$

Alternatively, this half-integer order Bessel function may be replaced by the spherical Bessel function

$$\psi_{m+n}(r_{h,j} k) = (\pi / 2r_{h,j} k)^{1/2} J_{m+n+1/2}(r_{h,j} k) \quad (4.56)$$

This results in a double infinite series

$$\mathbf{r}_r^{h,j} = \frac{2a_h}{a_j} \left[\sum_{m=0}^{\infty} \sum_{n=0}^{\infty} \frac{\Gamma(m+n+1/2)}{m!n!\pi^{1/2}} \left(\frac{a_j^m a_h^n}{r_{h,j}^{m+n}} \right) \times J_{1+m}(a_j k) \cdot J_{1+n}(a_h k) \psi_{m+n}(r_{h,j} k) \right] \quad (4.57)$$

This series is absolutely convergent for all finite values of a_j , a_h and $r_{h,j}$.

Mutual radiation reactance

The mutual radiation reactance $x_r^{h,j}$ may be obtained from Eq. (4.52) by integrating along the pure imaginary values of θ , where $\theta \in [(0, i\infty)]$ at $\text{Re}(\theta) = \pi / 2$,

$$x_r^{h,j} = -\frac{2a_h}{ia_j} \int_{\pi/2+i\infty}^{\pi/2+i\infty} \frac{J_1(a_j k \sin \theta)}{\sin \theta} \frac{J_1(a_h k \sin \theta)}{\sin \theta} J_0(r_{h,j} k \sin \theta) \sin \theta d\theta \quad (4.58)$$

By employing a change of variable $t = ik \cos \theta$, $\sin \theta = (k^2 + t^2)^{1/2} / k$, Eq. (4.58) can be rewritten as

$$x_r^{h,j} = -\frac{2a_h k}{a_j} \int_0^\infty \frac{J_1[a_j(t^2 + k^2)^{1/2}]}{(t^2 + k^2)^{1/2}} \frac{J_1[a_h(t^2 + k^2)^{1/2}]}{(t^2 + k^2)^{1/2}} \times J_0[r_{h,j}(t^2 + k^2)^{1/2}] dt \quad (4.59)$$

This integral can be evaluated using the procedure described in, and Eq. (4.59) can be written as a double infinite series

$$x_r^{h,j} = -\frac{2a_h}{a_j} \sum_{m=0}^{\infty} \sum_{n=0}^{\infty} \frac{(-1)^{m+n} \Gamma(m+n+1/2) a_j^m a_h^n 2^{m+n}}{m!n!k^{m+n+1} r_{h,j}^{2m+2n+1}} \cdot \int_0^{\pi/2} J_{1+m}(a_j k) \cdot J_{1+n}(a_h k) \times \left\{ \frac{1}{2\pi i} \int_C u^{-1+m+n+1/2} \exp\left(u - \frac{r_{h,j}^2 k^2}{4u}\right) du \right\} \quad (4.60)$$

where C represents a contour which starts from $-\infty$ on the real axis, encircles the origin once in the positive sense, and returns to $-\infty$. This contour integral may be expressed in terms of the Bessel function $J_{-m-n-1}(r_{h,j} k)$. Alternatively, this can be replaced by the spherical Bessel function

$$\chi_{m+n}(r_{h,j} k) = (-1)^{m+n} (\pi / 2kr_{h,j})(\pi / 2r_{h,j} k)^{1/2} J_{-m-n-1}(r_{h,j} k) \quad (4.61)$$

Eq. (4.60) can then be expressed as

$$x_r^{h,j} = -\frac{2a_h}{a_j} \sum_{m=0}^{\infty} \sum_{n=0}^{\infty} \frac{\Gamma(m+n+1/2)}{m!n!\pi^{1/2}} \left(\frac{a_j^m a_h^n}{r_{h,j}^{m+n}} \right) \times J_{1+m}(a_j k) \cdot J_{1+n}(a_h k) \chi_{m+n}(r_{h,j} k) \quad (4.62)$$

This series is absolutely convergent for $(a_j a_h / r_{h,j}^2) < 1$.

The average total pressure p_h^{avg} on orifice h results from Eq. (4.33)

$$p_h^{avg} = 2p_{in}^{avg} + z_{r,h} v_h \rho_0 c \quad (4.63)$$

which can be expressed by the normalized input impedance $z_{in,h}$ for orifice h as

$$p_h^{avg} = -v_h (\rho_0 c) z_{in,h} \quad (4.64)$$

Substituting Eq. (4.64) into Eq. (4.63) yields the following relation

$$-2p_{in,1}^{avg} = (z_{11} + z_{in,1}) v_1 \rho_0 c + z_{12} \rho_0 c v_2 \quad \text{if } h = 1; \quad (4.65a)$$

$$-2p_{in,2}^{avg} = (z_{22} + z_{in,2}) \rho_0 c v_2 + z_{21} \rho_0 c v_1 \quad \text{if } h = 2. \quad (4.65b)$$

Substituting $V_1 = \rho_0 c v_1$, $V_2 = \rho_0 c v_2$ into Eq. (4.65a) and Eq. (4.65b), V_1, V_2 can be calculated as

$$V_1 = \frac{2p_{in}(z_{22} + z_{in,2} - z_{12})}{z_{21}z_{12} - (z_{22} + z_{in,2})(z_{11} + z_{in,1})} \quad (4.66a)$$

$$V_2 = \frac{2p_{in}(z_{11} + z_{in,1} - z_{21})}{z_{12}z_{21} - (z_{22} + z_{in,2})(z_{11} + z_{in,1})} \quad (4.66b)$$

4.3 Summary

In this chapter, the proposed HR based sandwich panel was modeled as a semi-infinite space bounded by a rigid panel with only one unit cell. Two types of HR panels were

introduced: single HR unit cell and dual HRs unit cells with different orifices. The radiation property for this model was derived by Kirchhoff-Helmholtz integral by using the Green's function. The one dimensional mass-spring system of the HR and the corresponding impedance were illustrated. The thermal-viscous energy dissipation at the thermal boundary layer dominates the total energy consumed. The established theory can be used to calculate the maximum absorption power of the HR at the resonance. The sound radiation was coupled when another HR was introduced based on single HR. In order to solve the Kirchhoff-Helmholtz integral for dual HRs, the mutual radiation impedance and the corresponding mutual radiation resistance and reactance were presented, which is attributed to the coupling. The theory foundation will lead the perfect sound absorption design on the full size sandwich panels.

Chapter 5

Perfect sound absorption panel using periodic arranged Helmholtz resonators

Since the honeycomb structures, which are composed of hollow cells (whether the core is in hexagonal, cylindrical or rectangular shape), sandwiched between top and bottom thin face sheets and separated between thin vertical walls, are well known to yield lower weight and material cost. In comparison the acoustic impedance of the honeycomb cell with that of air, the face sheets and vertical walls of the honeycomb panels can be treated as rigid. By perforating a small circular opening (orifice) on the top face sheet in the each repetitive unit cell, each unit cell of the honeycomb panel can be readily adapted as a Helmholtz resonator. In each unit cell, the perforated orifice, and the volume formed by the honeycomb core surrounded by the walls and bottom surface represents the neck and cavity for a Helmholtz resonator, respectively.

In this chapter, two types of perfect sound absorber panels with HRs are designed with respect to the single HR as a unit cell and the dual HRs as a unit cell at sub-wavelength size in low frequencies. The sound pressure in terms of acoustic impedance is investigated first by solving the Kirchhoff-Helmholtz integral. The average power flow method and the equivalent surface impedance method are then proposed to calculate the absorption coefficient of the panel. The perfect sound absorber sandwich panels with two types of unit cells are finally presented and the absorption bandwidth based on Q factor is analyzed. The theory of perfect sound absorption prediction for the panel design is compared with the numerical results by finite element simulation. The perfect sound absorption for the entire sandwich panel requires that each unit cell yields total sound absorption simultaneously. The

total power absorbed on a sandwich panel is equal to the sum of power dissipated by individual HRs.

5.1 Identical Helmholtz resonators in the panel

The sandwich panel is formed by periodically arranging identical HRs together with a perforated hole in each unit cell as shown in Figure 5.1. Each unit cell that is one HR is in rectangular shape with square cross section and labeled as (m, n) . The orifice center coordinates can be noted by the unit cell labels. Denote h as the index (integer) for any unit cell of HR. Based on the single HR and coupled dual HRs in the semi-infinite panel in the Chapter 4, the radiation pressure term with respect to the Kirchhoff-Helmholtz integral equation is the summation of all the unit cells as $h \in (-\infty, +\infty)$.

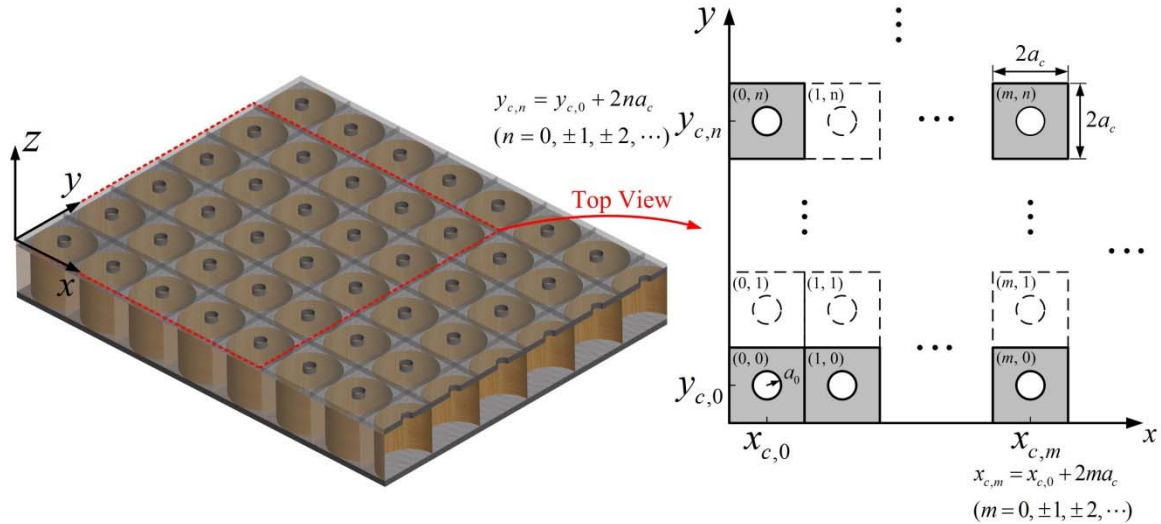


Figure 5.1 The sandwich panel with periodically arranged identical HRs.

Therefore, the sound pressure p on any location of the panel surface consisting of periodically perforated identical HRs can be written using the Kirchhoff-Helmholtz integral equation and is written as

$$p(x, y) = 2p_{in}(x, y) - \sum_{h=-\infty}^{\infty} ik\rho_0cv_h \iint_{S_h} G_N(\mathbf{r}|\mathbf{r}_0) dS_h \quad (5.1)$$

$p_r(x, y)$

where

$$\mathbf{r} = (x, y), \mathbf{r}_0 = (x_0, y_0) \quad (\mathbf{r}_0 \subseteq \mathbf{r})$$

$$G_N = \frac{e^{ikR}}{2\pi R}, \text{ with } R = \sqrt{(x-x_0)^2 + (y-y_0)^2} \quad (5.2)$$

which are same as the single unit cell derivation. The total sound pressure on the surface $p(x, y)$ results from the pressure induced by a source $2p_{in}(x, y)$ and the sound field generated by the boundary conditions (radiations $p_r(x, y)$) including the contribution from all of the orifices. In this situation, except the orifice, the top panel surface is rigid everywhere with zero velocity. The surface integral is thereby restricted by the orifice surface induced by the piston-like motion from the air in the orifice region.

Since the panel is periodic and infinite, it is equivalent to evaluate the absorption capability of the panel at any unit cell. The input velocities v_i at the entrance of any orifices are the same. Let the unit cell located at position $(0, 0)$ as the base cell for sound absorption evaluation. Under long wavelength assumption, i.e., the wavelength is much greater than the orifice radius, the average radiation pressure exerts on the base cell is derived from Eq. (5.1)

as

$$p_r^{(0,0)} = \frac{i\rho_0 c k v}{S_{(0,0)}} \iint_{S_{(0,0)}} \sum_{m,n} \iint_{S_{(m,n)}} G_N(\mathbf{r}|\mathbf{r}_0) dS_{(m,n)} dS_{(0,0)} = \rho_0 c v z_r^{(0,0)} \quad (5.3)$$

where

$$z_r^{(0,0)} = \frac{ik}{S_{(0,0)}} \sum_{m,n} \iint_{S_{(0,0)}} \iint_{S_{(m,n)}} G_N(\mathbf{r}|\mathbf{r}_0) dS_{(m,n)} dS_{(0,0)} \quad (5.4)$$

$z_r^{(0,0)}$ is defined as the net radiation impedance for the HR at base cell due to the radiation pressure from all the cells in the panel. Thus, any HR is coupled with all of the other unit cells and by recalling the definition of mutual impedance Eq. (4.44), it is observed that the net impedance is equal to the summation of mutual impedances for all the orifices including the base cell itself. The green function G_N can be calculated as

$$G_N = \frac{e^{ik\sqrt{(x_c^{(m,n)} - x_c^{(0,0)})^2 + (y_c^{(m,n)} - y_c^{(0,0)})^2}}}{2\pi\sqrt{(x_c^{(m,n)} - x_c^{(0,0)})^2 + (y_c^{(m,n)} - y_c^{(0,0)})^2}} \quad (5.5)$$

Averaging both sides of Eq. (5.1) over the orifice surface area of the base cell $S_{(0,0)}$, the total pressure at the bass orifice can be written as

$$p^{(0,0)} = 2p_{in}^{(0,0)} + p_r^{(0,0)} \quad (5.6a)$$

$$p_{(0,0)} = -v(\rho_0 c) z_i^{(0,0)} \quad (5.6b)$$

where $z_i^{(0,0)}$ is the input impedance of the orifice. Eq. (5.6a) can then be decomposed into a finite set of equations by substituting Eq. (5.3) and Eq. (5.6b) as

$$-2p_{in}^{(0,0)} = \rho_0 c v [z_r^{(0,0)} + z_i^{(0,0)}] \quad (5.7)$$

5.1.1 Absorption coefficient calculation-Energy Method

The absorbed power dissipated in the base unit cell is

$$\begin{aligned}
W_a &= \frac{1}{2} \text{Re}(p \cdot v^*) \pi a_0^2 \\
&= \frac{1}{2} \rho_0 c \text{Re}\{z_i^{(0,0)}\} \cdot |v|^2 \pi a_0^2
\end{aligned} \tag{5.8}$$

The power of the incident plane wave is

$$W_{inc} = I_{inc} A, \text{ where } I_{inc} = \frac{|p_{in}|^2}{2\rho_0 c} \tag{5.9}$$

where A is unit cell surface area. $A_0 = \pi a_0^2$ is the orifice surface area. The absorption coefficient of the sandwich panel is thereby defined as the ratio of the absorbed power W_a in HR to the incident power W_{inc} is given as

$$\alpha = \frac{W_a}{W_{inc}} = \frac{\pi a_0^2 \rho_0 c}{4a_c^2} \left| \frac{v}{p_{ia}} \right|^2 \text{Re}\{z_i^{(0,0)}\} \tag{5.10}$$

Substituting Eq. (5.7) into Eq. (5.10), the absorption coefficient of the sandwich panel can be written in the following form

$$\alpha = \frac{\pi a_0^2}{A} \frac{4 \text{Re}\{z_i^{(0,0)}\}}{|z_r^{(0,0)} + z_i^{(0,0)}|^2} \tag{5.11}$$

The mutual radiation impedance $z_r^{(0,0)}$ can be obtained by using the spatial Fourier transform of the Green's function given in Eq. (5.5), and Bessel's integral leads to

$$z_r^{(0,0)} = \frac{\pi a_0^2}{A} + \frac{\pi a_0^2}{A} \sum_{\substack{m=-\infty \\ m,n \neq 0}}^{\infty} \sum_{n=-\infty}^{\infty} \frac{ik}{\sqrt{\xi_{mn}^2 - k^2}} \left(\frac{2J_1(a_0 \xi_{mn})}{a_0 \xi_{mn}} \right)^2 \tag{5.12}$$

where

$$\xi_{mn} = \sqrt{\left(\frac{2\pi m}{D_x} - k_x\right)^2 + \left(\frac{2\pi n}{D_y} - k_y\right)^2} \tag{5.13}$$

ξ_{mn} ($m, n \neq 0$) is always greater than k since

$$(m\lambda / D_x)^2 + (n\lambda / D_y)^2 > 1 \quad \text{for } (m,n) \neq (0,0) \quad (5.14)$$

The double summation in Eq. (5.12) now becomes purely imaginary and thus represents the net radiation reactance $x_r^{(0,0)}$ of the base HR which is related to the external end correction $l_{ex}^{(0,0)}$ by

$$x_r^{(0,0)} = \frac{\pi a_0^2}{A} \sum_{\substack{m=-\infty \\ m,n \neq 0}}^{\infty} \sum_{n=-\infty}^{\infty} \frac{k}{\sqrt{\xi_{mn}^2 - k^2}} \left(\frac{2J_1(a_0 \xi_{mn})}{a_0 \xi_{mn}} \right)^2 = kl_{ex}^{(0,0)} \quad (5.15)$$

Substituting Eq. (5.15) into Eq. (5.10) gives

$$\alpha = \frac{4 \operatorname{Re}\{z_i^{(0,0)}\} / \zeta}{\left| 1 + (z_i^{(0,0)} + ikl_{ex}^{(0,0)}) / \zeta \right|^2} = \frac{4 \operatorname{Re}\{z_i^{(0,0)}\} / \zeta}{\left| 1 + \frac{\operatorname{Re}\{z_i^{(0,0)}\}}{\zeta} \right|^2 + \left| \frac{\operatorname{Im}\{z_i^{(0,0)} + ikl_{ex}^{(0,0)}\}}{\zeta} \right|^2} \quad (5.16)$$

where $\zeta = \pi a_0^2 / A$ is the surface porosity.

On the other hand, from Eq. (5.12), the net radiation resistance $r_r^{(0,0)}$ for the base cell turns out to be a constant value $\pi a_0^2 / A$ and thus the absorption coefficient in Eq. (5.11) can also be written as

$$\alpha = \frac{4r_i^{(0,0)}r_r^{(0,0)}}{\left| z_r^{(0,0)} + z_i^{(0,0)} \right|^2} \quad (5.17)$$

5.1.2 Absorption coefficient calculation-Surface Impedance Method

The panel surface with orifices can be treated as a homogenous surface with equivalent surface impedance under the long wavelength assumption. The surface impedance for the base cell can be expressed in an average sense, i.e.,

$$z_{surf}^{avg} = \frac{\langle p \rangle}{\langle v \rangle} \approx \frac{Ap_{HR}}{A_0 v} \quad (5.18)$$

where p_{HR} is the pressure at the outlet orifice of HR and can be derived from Eq.(5.1) and Eq. (5.3) as

$$p_{HR} = 2p_{in} + p_r - ikl_{ex}v \quad (5.19)$$

Substituting Eq. (5.19) into Eq. (5.18) gives the equivalent surface impedance

$$z_{surf}^{avg} = \frac{z_{HR}}{\zeta} = \frac{z_i + z_r}{\zeta} = \frac{z_i - ikl_{ex}}{\zeta} \quad (5.20)$$

The absorption coefficient α can be simply derived as

$$\begin{aligned} \alpha &= 1 - \left| \frac{z_{surf}^{avg} - 1}{z_{surf}^{avg} + 1} \right|^2 \\ &= \frac{4 \operatorname{Re}(z_{surf}^{avg})}{\left\{ \left[1 + \operatorname{Re}(z_{surf}^{avg}) \right]^2 + \left[\operatorname{Im}(z_{surf}^{avg}) \right]^2 \right\}} \\ &= \frac{4 \operatorname{Re}(z_i) / \zeta}{\left\{ \left[1 + \operatorname{Re}(z_i) / \zeta \right]^2 + \left[\operatorname{Im}(z_i + z_r) / \zeta \right]^2 \right\}} \end{aligned} \quad (5.21)$$

5.1.3 Perfect sound absorption for the sandwich panel

The perfect absorption requires that the sandwich panel with embedded HRS is at the resonant state and the average surface impedance of panel matches with the air impedance simultaneously. As shown in Figure 5.2, a normal incident wave impinges on the panel surface interface between Medium II and air medium I. No waves can be reflected and all the wave energy is transmitted into medium II when perfect absorption occurs.

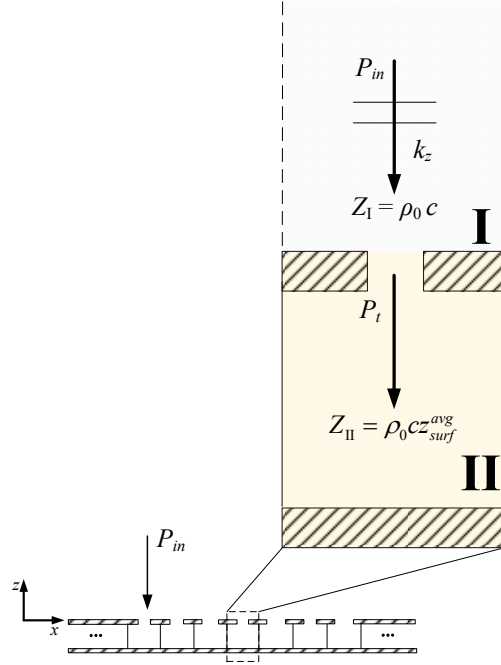


Figure 5.2 wave propagation of the perfect sound absorber sandwich panel with identical unit cells

At resonant frequencies, the average surface reactance x_{surf}^{avg} vanishes, i.e.,

$$x_i + x_r = 0 \quad \text{at resonance} \quad (5.22)$$

Thus we have

$$(a_0 / a_c)^2 \cot(kl_c) - k(l + l_{in}) - kl' \delta_v / a_0 = 0 \quad (5.23)$$

The absorption coefficient at resonance is thereby

$$\alpha = \frac{4r_r^{(0,0)}r_i^{(0,0)}}{|r_r^{(0,0)} + r_i^{(0,0)}|^2} = \frac{4\varepsilon}{(1 + \varepsilon)^2} \quad (5.24)$$

where $\varepsilon = r_i^{(0,0)}/r_r^{(0,0)}$. Perfect absorption is achieved for $\varepsilon = 1$, i.e., when the input resistance $r_i^{(0,0)}$ equals the net radiation resistance $r_r^{(0,0)} = \zeta$, and is

$$k(\gamma - 1)\delta_h l / 2a_0 + k\delta_v l / a_0 = \zeta \quad (5.25)$$

Eq. (5.23) and Eq. (5.25) provide the requirements to design a perfect sound absorber. In a panel absorber design, the cavity length or radius is known in prior and the following procedures can be adopted to obtain geometrical parameters for perfect absorption at desired frequencies:

Step 1) Given a fixed value of cavity radius a_c , iterating the frequency f and neck radius a_0 to find neck length l to satisfy resistance match condition, i.e., Eq. (5.25).

Step 2) Substituting the parameters obtained in Step 2) into Eq. (5.23) to calculate the corresponding cavity length l_c .

Step 3) Check the values of neck length l , cavity length l_c to ensure they are positive values and the thickness of the absorber ($l_c + 2l$) is much smaller than the wavelength so that the absorber is indeed in sub-wavelength.

Step 4) Output the value of desired resonant frequencies and the corresponding geometrical parameters for a perfect absorber design.

Based on the design procedure, two cases with cavity radiuses $a_c=30\text{mm}$ and $a_c=10\text{mm}$ are shown in Figure 5.3 and Figure 5.4. Figure 5.3(a) and 5.4(a) show the required geometrical parameters to design a perfect absorber at desired frequencies with cavity radius to be 30 mm and 10 mm, respectively. From the figures, it is clear shown that at any

frequency, there are a variety of geometrical choices that satisfy the critical total absorption conditions to absorb sound energy totally.

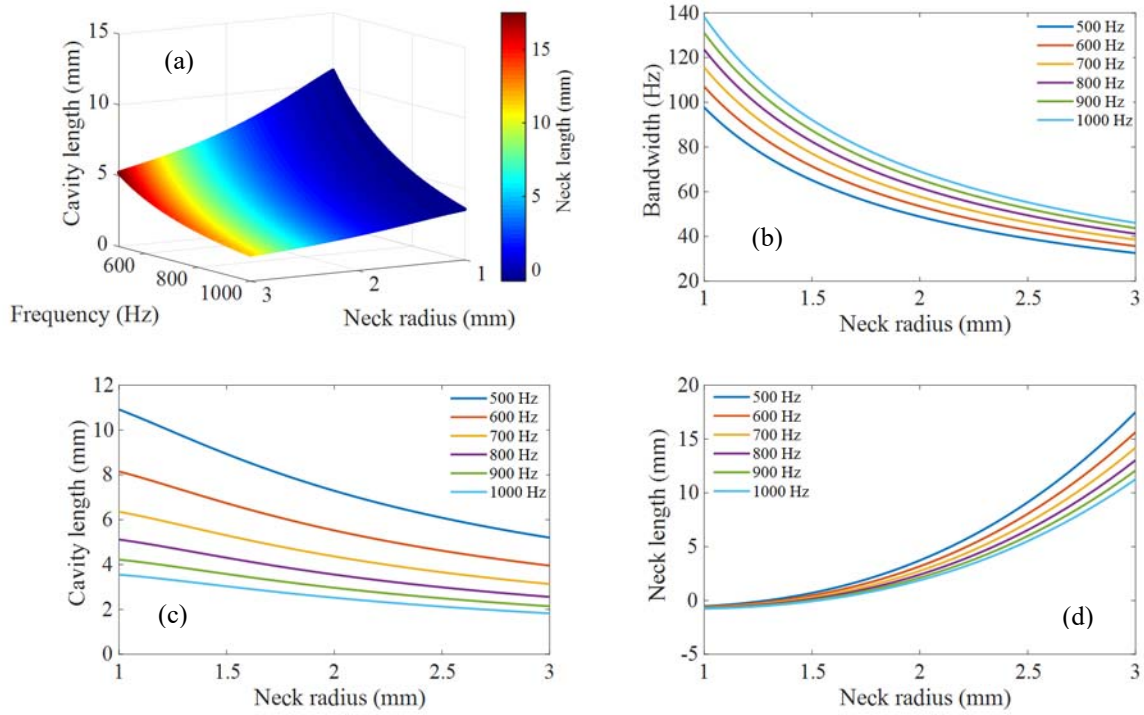


Figure 5.3 (a) Geometrical parameters required for designing perfect sound absorber sandwich panel at different frequencies, (b) the bandwidth of as a function of neck radius, (c) cavity length as a function of neck radius, (d) neck length as a function of neck radius.

The cavity radius is 30 mm.

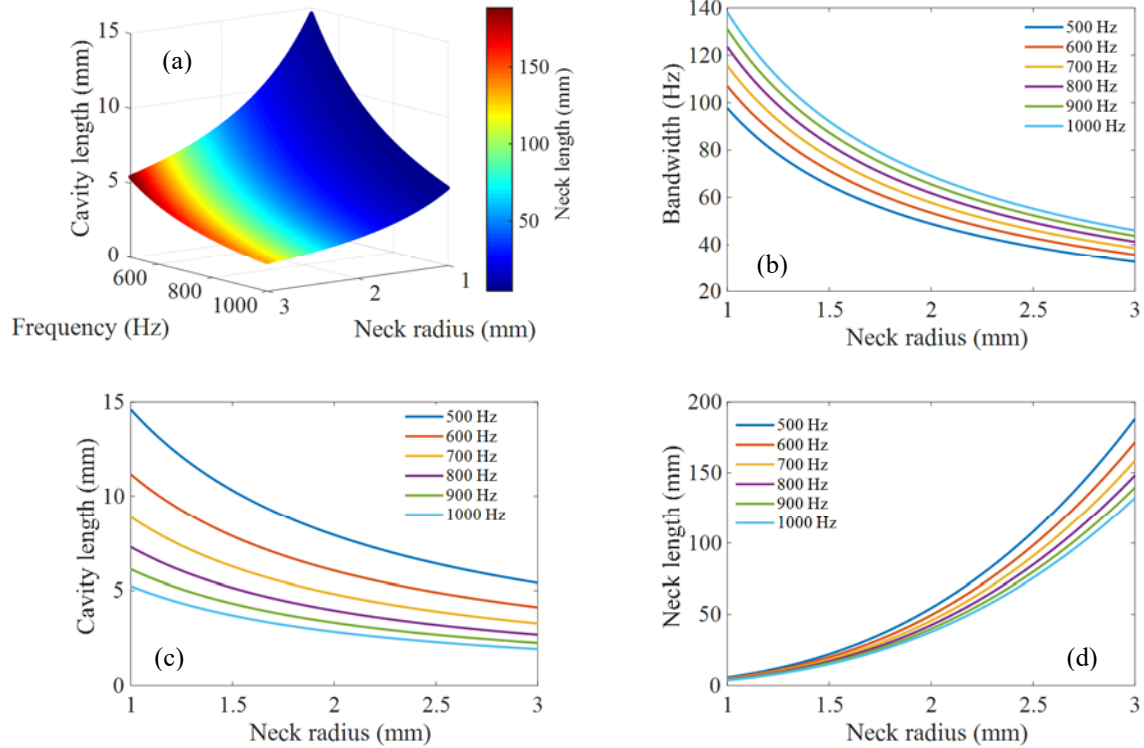


Figure 5.4 (a) Geometrical parameters required for designing perfect sound absorber sandwich panel at different frequencies, (b) the bandwidth as a function of neck radius, (c) cavity length as a function of neck radius, (d) neck length as a function of neck radius.

The cavity radius is 10 mm.

Perfect absorption is generally desired in most absorber designs, however, a larger bandwidth of sound absorption is another crucial factor that needs to be considered to measure the absorption selectivity of the absorber. An adequate measure is often selected for the frequency range in which the absorption coefficient is greater than 0.5 of the perfect

absorption at resonance. As the input resistance r_i varies little with frequency, the total resistance $r_r + r_i$ is assumed to be frequency independent and is chosen as the total resistance at resonance. The ‘half absorption point’ in the absorption response spectrum is thereby obtained as

$$\left(x_r^{(0,0)} + x_i^{(0,0)} \right) \Big|_{\text{half absorption}} = r_{r,n}^{(0,0)} + r_{i,n}^{(0,0)} = \pm 2\zeta \quad (5.26)$$

Substituting the expressions of $x_r^{(0,0)}$ and $x_i^{(0,0)}$ into Eq. (5.26) yields

$$\begin{cases} \frac{(a_0 / a_c)^2 c}{2\pi f_L l_c} - \frac{2\pi f_L l'}{c} = 2\zeta \\ \frac{(a_0 / a_c)^2 c}{2\pi f_R l_c} - \frac{2\pi f_R l'}{c} = -2\zeta \end{cases} \quad (5.27)$$

The bandwidth is given from Eq. (5.27) as

$$\Delta f = f_R - f_L = \frac{2}{a_0} \sqrt{\frac{\nu}{\pi}} \sqrt{f_n} \quad (5.28)$$

where f_R and f_L are the half-absorption frequencies at the left and right side of resonant frequency, respectively.

The corresponding Q -value is

$$Q = \frac{f_n}{\Delta f} = \frac{a_0}{2} \sqrt{\frac{\pi f_n}{\nu}} \quad (5.29)$$

It is seen from Eq. (5.28), the bandwidth for a perfect absorber in which the absorption coefficient is greater than 0.5 is inversely proportional to the neck radius a_0 and is proportional to the resonant frequency, and thus the Q factor decreases as the neck radius decreases which is evident by Eq. (5.29) as well.

The bandwidth of the perfect absorbers designed using Figure 5.3(a) and 5.4(a) can be theoretically predicted using Eq. (5.28). With the aid of the theoretical predictions, largest bandwidth of a perfect absorber around a target resonant frequency can be selected. Figure 5.3(b) and 5.4(b) show the relations between the bandwidth and the neck radius for the cavity radius fixed at 30 mm and 10 mm, respectively. To achieve perfect absorption at 500 Hz with cavity neck radius set as 30 mm, the largest bandwidth is determined to be 97.72 Hz if the neck radius a_0 is chosen to be 1mm, as shown in Figure 5.3(b). However, this bandwidth is not achievable since the neck length turns out to be a negative value. Figure 5.3(d) provides the relationship between the neck length and the neck radius. The neck length appears to be negative values for smaller neck radii. Figure 5.3(c) gives the change of cavity length as a function of neck radius. To avoid the negative neck length in the perfect absorber design, the cavity radius may be adjusted as needed. If the cavity radius is set as 10 mm, the neck lengths are positive for the radius values under consideration, as shown in Figure 5.4 (d), and these perfect absorbers can bring similar bandwidth as those having 30 mm cavity radius. The required cavity length that is shown in Figure 5.4(c) is under allowable range. As stated in the design procedures, the thickness of the cavity should be examined as well for subwavelength requirement. Therefore, the perfect absorber needs to be carefully designed and the geometrically parameters must be selected with caution to ensure a meaningful perfect absorber design with the largest bandwidth and minimum thickness.

In order to get a perfect absorber at 500 Hz having cavity radius equals to 30 mm, the required neck radius, neck length and cavity length are selected using Figure 5.3 and are determined to be 1.63 mm, 1.6 mm, and 7.847 mm, respectively. The bandwidth of this

absorber is found to be 59.95 Hz and absorber thickness is 11.074 mm which is approximated $1/62^{\text{th}}$ of the corresponding wavelength at 500 Hz. This confirms the proposed perfect absorber is indeed a deep subwavelength metamaterial structure. For a perfect absorber at 500 Hz with a 10 mm cavity radius, the bandwidth of this perfect absorber can be as large as 97.23 Hz, if the neck radius, neck length and cavity length are chosen to be 1 mm, 7.218 mm and 12.21 mm, respectively. The thickness of the perfect absorber is 26.646 mm which is about $1/26^{\text{th}}$ of the wavelength. Thus, a wider bandwidth is achievable for a 500 Hz perfect absorber at the cost of absorber thickness increasing.

Figure 5.5 and Figure 5.6 show the absorption coefficient spectrum as well as both the real and imaginary part of the average surface impedance for a perfect absorber at 500 Hz with different geometrical parameters. In the plots, the absorption coefficient calculated from the average surface impedance method is in agreement with the absorbed energy method. From Figure 5.5(b), (c) and Figure 5.6(b), (c), the average surface resistance matches the background air medium while the average surface reactance vanishes at 500 Hz where perfect absorption conditions are fulfilled for both structures. The bandwidth of the two absorbers obtained from the absorption spectrum are 57.4 Hz and 91 Hz, respectively, and agree well with the theoretical predicted bandwidth.

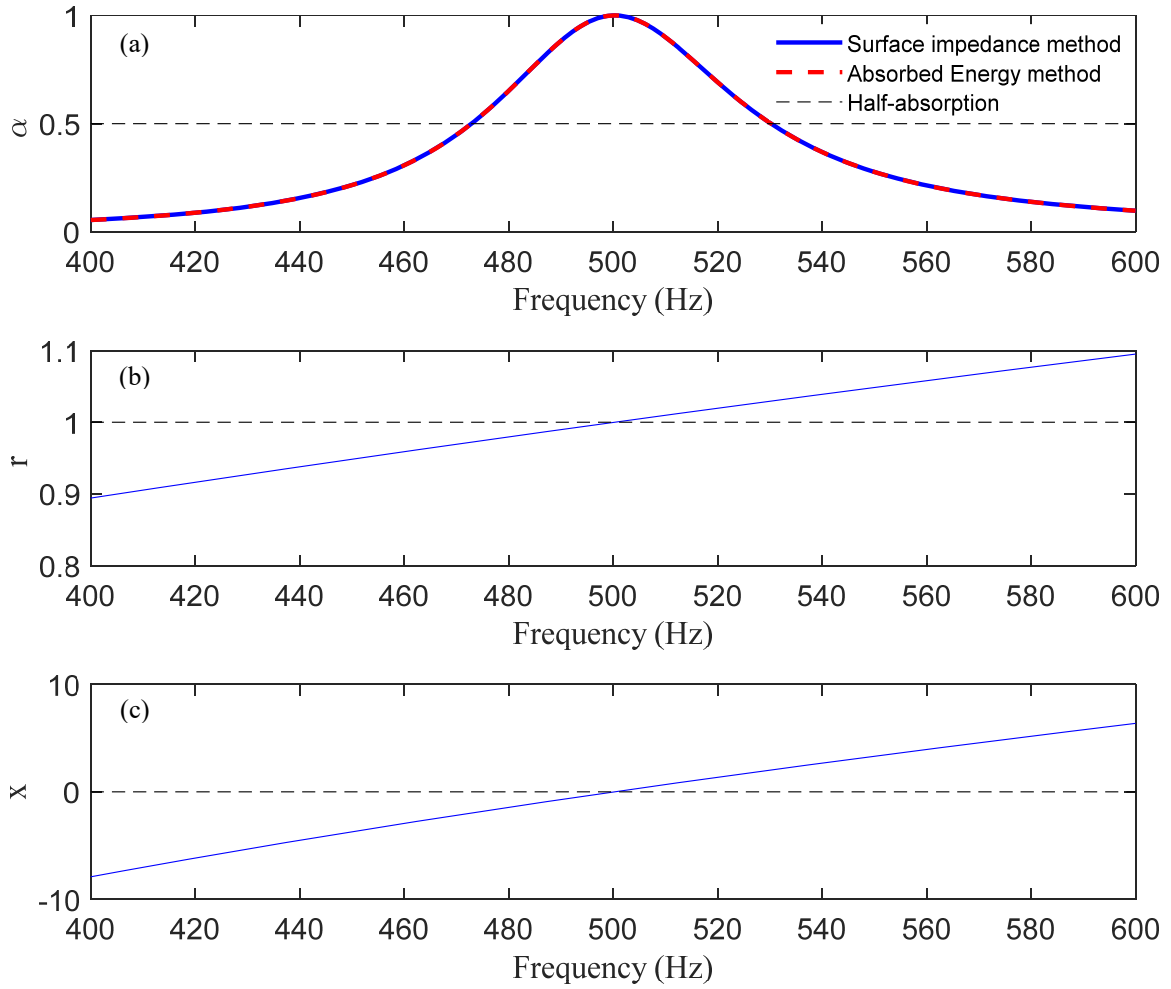


Figure 5.5 (a) Absorption spectrum of the proposed sound absorber sandwich panel, (b) resistive part of the sandwich panel, (c) reactive part of the sandwich panel with neck radius, neck length, cavity length and cavity radius to be 1.63 mm, 1.6 mm, 7.847 mm, and 30 mm, respectively.

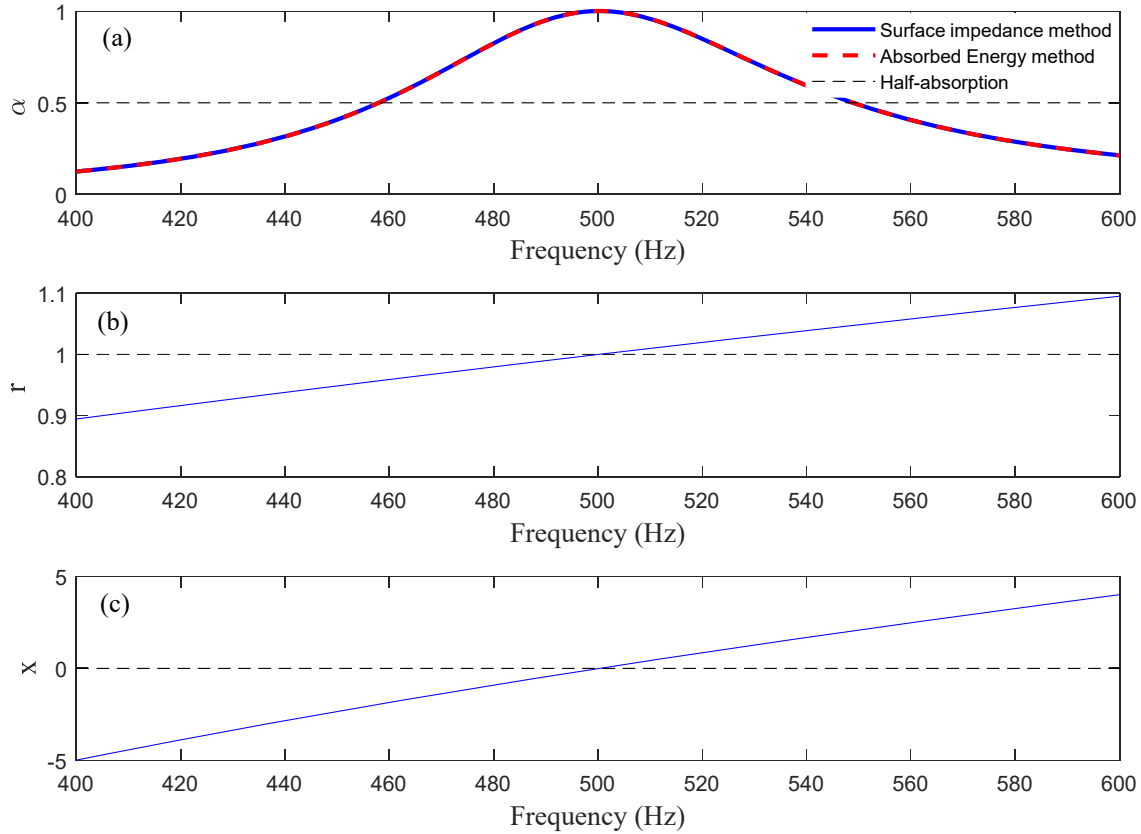


Figure 5.6 (a) Absorption spectrum of the proposed sound absorber sandwich panel, (b) resistive part of the sandwich panel, (c) reactive part of the sandwich panel with neck radius, neck length, cavity length and cavity radius to be 1 mm, 7.218 mm, 12.21 mm, and 10 mm, respectively.

5.1.4 Finite element simulation for numerical analysis

Comsol Multiphysics™ Version 5.2a with preset Thermoacoustic and Pressure acoustics modules are utilized to obtain the absorption spectrum of the perfect absorber sandwich panel. The effects of heat transfer and viscous friction are concluded in the linearized compressible Navier-Stokes equation, the continuity equation and the energy equation if the

diameter of neck radius a_0 is comparable to the viscous boundary layer δ_v . The background medium is air with its density $\rho_0 = 1.21 \text{ kg/m}^3$, speed of sound $c = 343.2 \text{ m/s}$, and dynamic viscosity $\mu = 1.21 \text{ kg/m}^3$. A normally incident plane wave with unit amplitude is incident along negative z direction and impinges on the surface of the unit cell of the sandwich panel. Hard boundary conditions are imposed on the panel surfaces except the openings since the impedance mismatch between the panel and the air is huge. Periodic boundary (continuity) conditions are applied at the four surfaces of the air and HR domain to model a periodic arranged HRs based sandwich panel to reduce computational cost

Figure 5.7(a) shows the absorption spectrum of the proposed perfect absorber with maximum absorption occurs at 500 Hz. The simulation results show a good accordance with the theoretical predictions for both the surface impedance and energy method. Figure 5.7(b) and 5.7(c) give the comparison of average surface resistance and reactance obtained from theoretical model and finite element simulation and show a very good agreement. It confirms that the conditions to achieve perfect absorption, i.e., impedance match condition ($r = 1$) is fulfilled at resonant state ($x = 0$). An energy conservation relation exists for the presented sound absorber, and can be stated as

$$\Delta W = W_{in} - W_{ref} = W_{loss} \quad (5.30)$$

where W_{in} and W_{ref} denoted the incident wave energy and reflected wave energy at the inlet of domain I, respectively, and W_{loss} is the total loss resulting from viscous and thermal loss. The energy difference between the incident and reflected wave are dissipated in the neck of HR due to both the viscous and thermal losses.

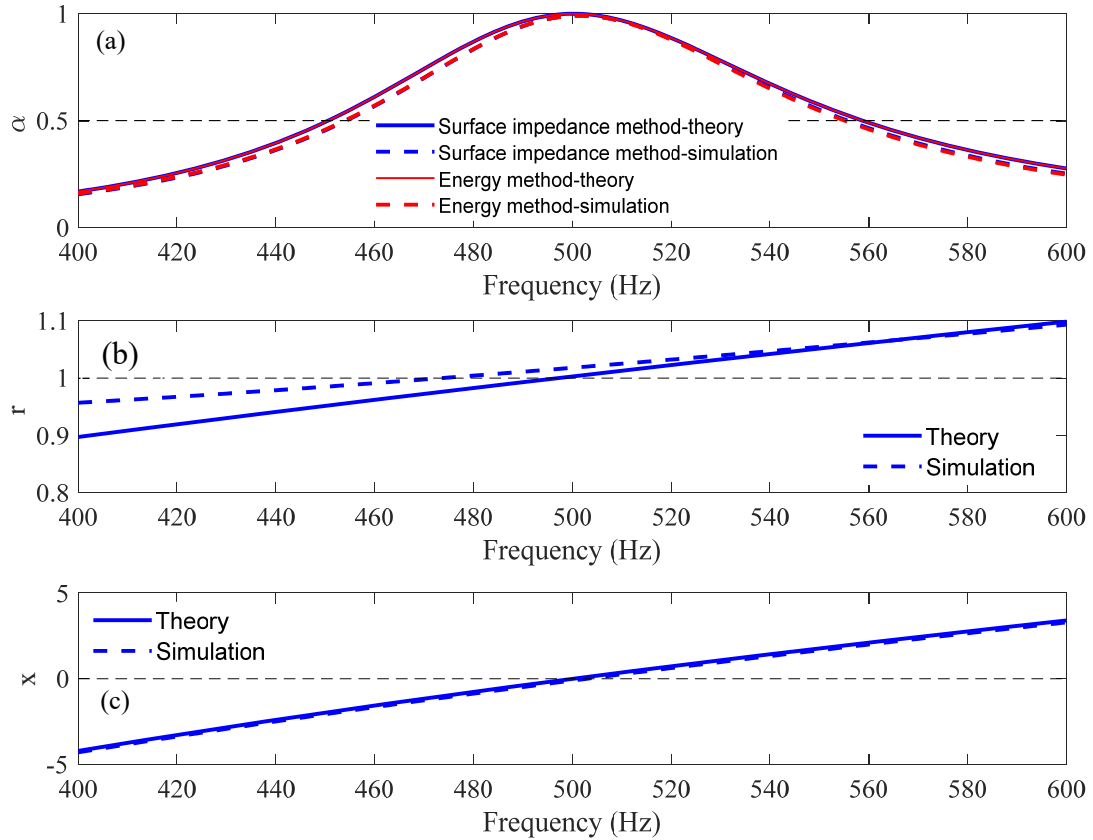


Figure 5.7 (a) Comparison of theoretical and numerical results of absorption coefficient spectrum, (b) comparison on resistance, (c) comparison on reactance. The neck radius, neck length, cavity length and cavity radius are 1 mm, 7.218 mm, 12.21 mm, and 10 mm, respectively.

Figure 5.8 shows the energy conservation relation of the proposed sound absorber, i.e., the relation between Logarithm of the power and frequency. It is found that the energy difference equals exactly the amount of total energy loss from viscous friction and heat conduction, which means all the incident energy transmitted into the sandwich panel and is

dissipated and no reflection wave is observed at the plane wave inlet. It is clear from the figure, the energy loss due to thermal effect is much smaller compared to the loss from viscous shear. However, the thermal loss must be considered so as to obtain an accurate average surface impedance value and the resonant frequency of the absorber.

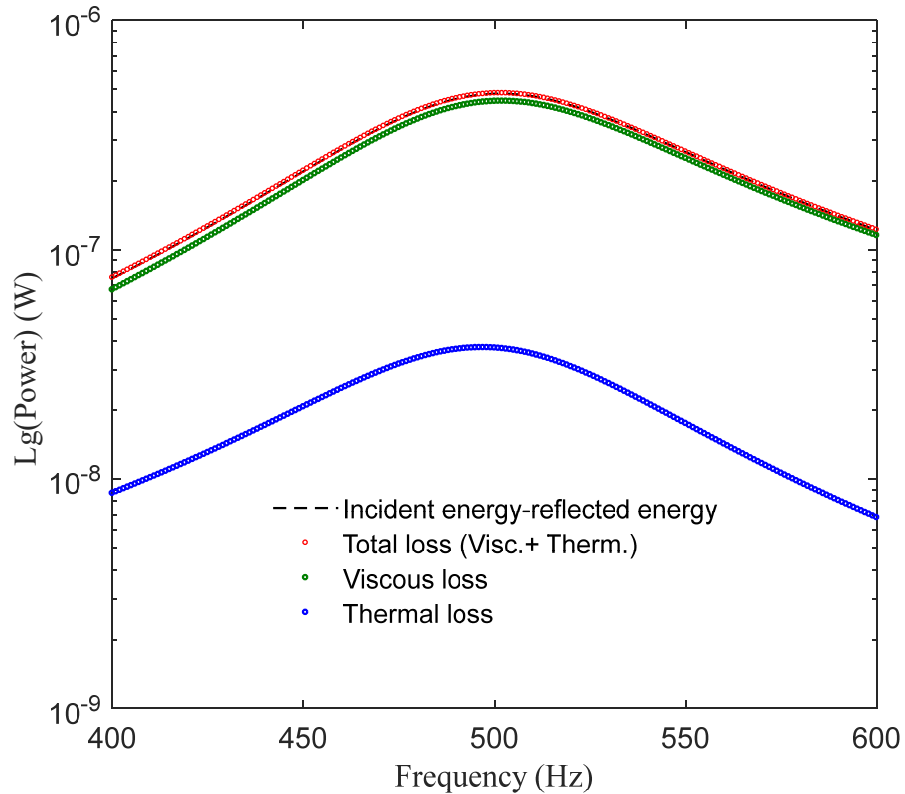


Figure. 5.8 Energy conservation of the sound absorber panel.

5.2 Two different Helmholtz Resonators as a unit cell in the panel

Based on dual HRs in the semi-infinite rigid panel, the dual HRs as one unit cell are periodically arranged to form sandwich panel, shown in Figure 5.9. Each unit cell with two

HRs is labeled as (m, n) . For any unit cell that is denoted by the integer $h \in (-\infty, +\infty)$, the orifice radii are a_1 and a_2 respectively. Denote j as the index for the any HR in one unit cell ($j=1, 2$). The orifice center coordinates can be presented by the unit cell labels and the HR index in any unit cell. The pressure at any point on the panel surface is attributed to the incident pressure and the radiation pressure from all of the orifices. Therefore, the sound pressure p on any point of x - y plane can be described using the Kirchhoff-Helmholtz integral equation and is written as

$$p(x, y) = 2p_{in}(x, y) - \sum_{h=-\infty}^{\infty} ik\rho_0cv_h \iint_{S_h} G_N(\mathbf{r}|\mathbf{r}_0) dS_h \quad (5.31)$$

$p_r(x, y)$

where

$$\mathbf{r} = (x, y), \mathbf{r}_0 = (x_0, y_0) \quad (\mathbf{r}_0 \subseteq \mathbf{r})$$

$$G_N = \frac{e^{ikR}}{2\pi R}, \text{ with } R = \sqrt{(x-x_0)^2 + (y-y_0)^2} \quad (5.32)$$

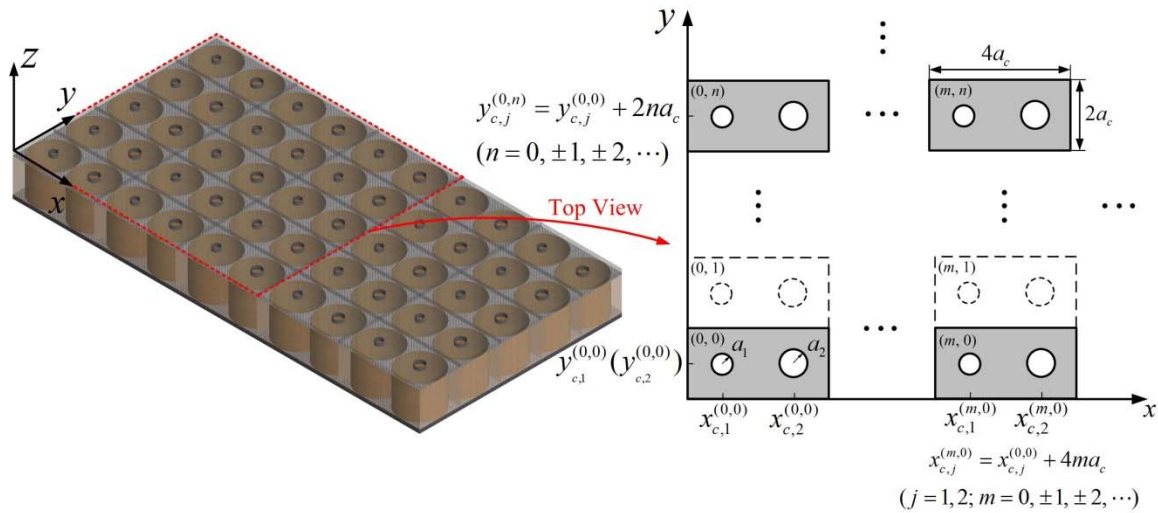


Figure 5.9 the sandwich panel with periodically arranged dual HRs.

and v is the orifice velocity (velocity is taken positive along the positive z direction). Similarly to the previous derivation, the first term in the right-hand side of Eq. (5.31) is the pressure induced by a source, and the second term denotes the sound field generated by the boundary conditions (radiations) including the effects from all the orifices. The panel surface is rigid everywhere with zero velocity except the orifice. The surface integral is thereby restricted by the orifice surface induced by the piston-like motion from the air in the neck region.

Since the panel is periodic and infinite, considering one unit cell is adequate enough to compute the sound absorption coefficient. For convenience, the unit cell labeled as $(0, 0)$ is chosen for absorption calculation. According to the position of the unit cell, the coordinates for the two HRs located at base cell $(0, 0)$ are given as $(x_{c,j}^{(0,0)}, y_{c,j}^{(0,0)})$. The same HR located at different cells possesses the same velocity v_j .

Since the orifice radius is much smaller compared with the wavelength, the average radiation pressure at orifice j in cell $(0, 0)$ after considering all the scatterings from HRs (m, n) in the panel with corresponding orifice j' in the unit cell can be written as

$$p_{r,j}^{(0,0)} = \sum_{j'=1}^2 \frac{i\rho_0 c k v_{j'}}{S_j^{(0,0)}} \iint_{S_j^{(0,0)}} \iint_{S_{j'}^{(m,n)}} G_N(\mathbf{r}|\mathbf{r}_0) dS_{j'}^{(m,n)} dS_j^{(0,0)} \quad (j=1,2) \quad (5.33a)$$

$$p_{r,j}^{(0,0)} = \rho_0 c v_j z_{r,j}^{(0,0)} \quad (j=1,2) \quad (5.33b)$$

The net radiation impedance of any orifice in base cell $(0, 0)$ can be obtained by Eq. (5.33)

$$z_{r,j}^{(0,0)} = \sum_{j'=1}^2 \frac{ikv_{j'}}{v_j S_j^{(0,0)}} \sum_{m',n'} \iint_{S_j^{(0,0)}} \iint_{S_j^{(m,n)}} G_N(\mathbf{r}|\mathbf{r}_0) dS_{j'}^{(m,n)} dS_j^{(0,0)} \quad (5.34)$$

The mutual radiation impedance for orifices j at base unit cell $(0, 0)$ due to the radiation pressure from the orifices j' resulting from all the cells (m, n) can be written with respect to net radiation impedance as

$$z_r^{j(0,0),j'(m,n)} = \frac{ik}{S_j^{(0,0)}} \sum_{j'=1}^2 \sum_{m,n} \iint_{S_j^{(0,0)}} \iint_{S_j^{(m,n)}} G_N(\mathbf{r}|\mathbf{r}_0) dS_{j'}^{(m,n)} dS_j^{(0,0)} \quad (5.35)$$

where

$$G_N = \frac{e^{ik\sqrt{(x_{c,j'}^{(m,n)} - x_{c,j}^{(0,0)})^2 + (y_{c,j'}^{(m,n)} - y_{c,j}^{(0,0)})^2}}}{2\pi\sqrt{(x_{c,j'}^{(m,n)} - x_{c,j}^{(0,0)})^2 + (y_{c,j'}^{(m,n)} - y_{c,j}^{(0,0)})^2}} \quad (5.36)$$

By averaging the total pressure over the orifice surface area $S_j^{(0,0)}$, the average total pressure and the input pressure become the pressures at the center of the orifice as $p_j^{(0,0)}$ and $2p_{in,j}^{(0,0)}$, respectively. Given the fact that the total pressure at orifice $j^{(0,0)}$ is $p_j^{(0,0)} = -v_j(\rho_0 c)z_{in,j}^{(0,0)}$, where $z_{in,j}^{(0,0)}$ is the input impedance of orifice $j^{(0,0)}$, resulting in the following finite set of equations

$$-2p_{in,j}^{(0,0)} = \rho_0 c v_j (z_{r,j}^{(0,0)} + z_{in,j}^{(0,0)}) \quad (j=1,2) \quad (5.37)$$

5.2.1 Absorption coefficient calculation-Energy Method

The absorbed energy in the unit cell is the summation of the energy dissipated by individual HR from the real power flow into the orifices and can be written as

$$W_a = \frac{1}{2} \sum_{j=1}^2 \text{Re}(p \cdot v_j^*) \pi a_j^2 = \frac{1}{2} \sum_{j=1}^2 \rho_0 c \text{Re}\{z_{in,j}\} \cdot |v_j|^2 \pi a_j^2 \quad (5.38)$$

The energy of the incident wave can be given as

$$W_{inc} = I_{inc} A, \text{ where } I_{inc} = \frac{|p_{in}|^2}{2\rho_0 c} \quad (5.39)$$

where $A = 8a_c^2$ is the surface area of the unit cell.

The absorption coefficient of the absorber sandwich panel is thereby defined as the ratio between the absorbed power W_a and the incident power W_{inc} and is given as

$$\alpha = \frac{W_a}{W_{inc}} = \frac{\pi a_j^2 \rho_0 c}{8a_c^2} \sum_{j=1}^2 \left| \frac{v_j}{p_{in}} \right|^2 \text{Re}\{z_{in,j}\} \quad (5.40)$$

Substituting Eq. (5.37) into Eq. (5.40), the absorption coefficient can be rewritten as

$$\alpha = \frac{\pi a_1^2}{A} \frac{4 \text{Re}\{z_{in,1}\}}{|z_r^{1(0,0)} + z_{in,1}|^2} + \frac{\pi a_2^2}{A} \frac{4 \text{Re}\{z_{in,2}\}}{|z_r^{2(0,0)} + z_{in,2}|^2} \quad (5.41)$$

where

$$z_r^{1(0,0)} = z_r^{1(0,0),1(m,n)} + z_r^{1(0,0),2(m,n)} (v_2 / v_1) \quad (5.42a)$$

$$z_r^{2(0,0)} = z_r^{2(0,0),2(m,n)} + z_r^{2(0,0),1(m,n)} (v_1 / v_2) \quad (5.42b)$$

are defined as net radiation impedance for HR1 and HR2 in the base cell unit, respectively.

It's worth noting that the mutual radiation impedance $z_r^{1(0,0),1(m,n)}$ is independent of the velocity which is consistent with the electric-circuit theory. On the other hand, the net radiation impedance of each resonator $z_r^{j(0,0)} = p_r^{j(0,0)} / v_j$ is a function of the velocities of the other radiators as shown in Eq. (5.42).

5.2.2 Absorption coefficient calculation - Surface Impedance Method

Another straightforward way to compute the absorption coefficient is to obtain the pressure reflection coefficient first at the interface between the HR and air, which is expressed as

$$r_p = \left| \frac{Z_{surf}^{avg} - Z_0}{Z_{surf}^{avg} + Z_0} \right| \quad (5.43)$$

where Z_{surf}^{avg} is the equivalent surface impedance of the sandwich panel surface and $Z_0 = 1$ is the normalized specific acoustic impedance of air.

If the individual resonator in the unit cell is much smaller compared with the wavelength, i.e. ($ka_j \ll 1$), constant pressure distribution over the entire surface can be assumed. The average (equivalent) specific surface impedance of the sandwich panel can be approximated as

$$Z_{surf}^{avg} = \frac{P_{surf}}{\langle v \rangle} \approx \frac{P_{HR}}{A_1 v_1 / A + A_2 v_2 / A} = \frac{1}{\zeta_1 / Z_{HR}^1 + \zeta_2 / Z_{HR}^2} = \frac{Z_{HR}^1 Z_{HR}^2}{\zeta_1 Z_{HR}^2 + \zeta_2 Z_{HR}^1} \quad (5.44)$$

The average specific surface impedance can also be generalized by the corresponding admittance that is written as

$$y_{surf}^{avg} = \sum_{j=1}^2 \zeta_j y_{HR}^j \quad (j=1,2) \quad (5.45)$$

where

$$y_{HR}^j = 1 / Z_{HR}^j = 1 / \{ Z_{in}^j + ikl_{ex}^j \} \quad (5.46)$$

$$\zeta_j = \frac{\pi a_j^2}{8a_c^2} \quad (5.47)$$

ζ_j is the surface porosity. It should be noted that y_{HR}^j is the normalized specific admittance of the sandwich panel containing only HRs in the base unit cell, respectively. The exact value of external end correction l_{ex}^j of each HR in a unit cell depends on the actual boundary condition, and is hard to obtain analytically. However, it can be taken as $8a_j/3\pi$ as a good approximation by only considering the radiation effects from the orifices of the same type.

The absorption coefficient of the sandwich panel can then be computed with the aid of the well familiar relation as

$$\alpha = 1 - |r_p^2| = \frac{4 \operatorname{Re}(z_{surf}^{avg})}{\left\{ \left[1 + \operatorname{Re}(z_{surf}^{avg}) \right]^2 + \left[\operatorname{Im}(z_{surf}^{avg}) \right]^2 \right\}} \quad (5.48)$$

5.2.3 Perfect absorption for sandwich panel

When a normal incident wave impinges on the panel surface interface between Medium II and air medium I, no waves can be reflected and all the wave energy is transmitted into medium II when perfect absorption occurs, as shown in Figure 5.10. The resonance of the sandwich panel consisting of two different HRs in a unit cell occurs when the average surface specific admittance y_{surf}^{avg} becomes maximum, i.e., the surface average reactance of Eq. (57) reaches to zero, i.e.,

$$\operatorname{Im}(z_{surf}^{avg}) = x_{surf}^{avg} = 0 \quad (5.49a)$$

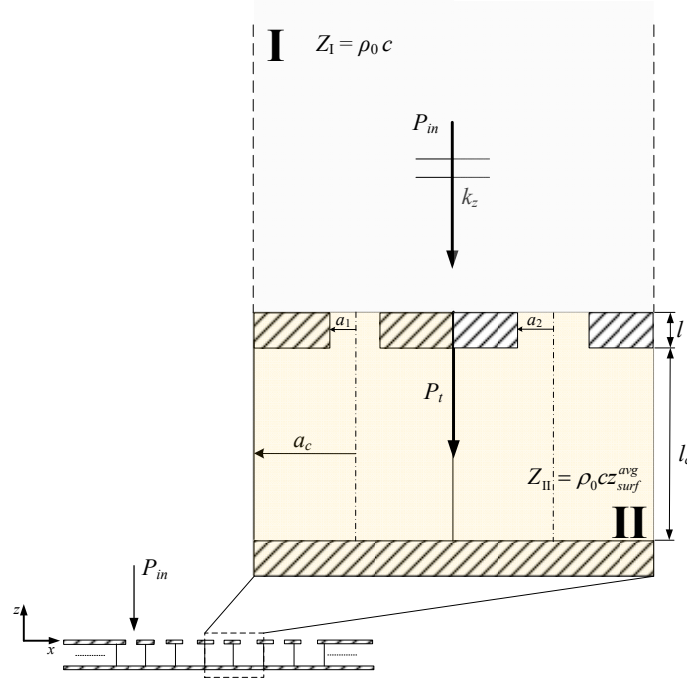


Figure 5.10 Wave propagation of the perfect sound absorber sandwich panel with dual HR as a unit cell

In order to achieve perfect sound absorption over the unit cell surface, resistance match is required to eliminate unnecessary reflection from the panel surface, i.e., the resistive part of Eq. (5.47) has to match with the air resistance

$$\text{Re}(z_{surf}^{avg}) = r_{surf}^{avg} = 1 \quad (5.49b)$$

Therefore, Eq. (5.49a) and Eq. (5.49b) need to be satisfied simultaneously to realize a perfect deep sub-wavelength sound absorber panel.

Expanding Eq. (5.47) in the form of total input resistance and reactance, the surface average resistance can be reorganized as

$$\begin{aligned}
Z_{surf}^{avg} &= \frac{r_{HR}^1 r_{HR}^2 - x_{HR}^1 x_{HR}^2 + i(r_{HR}^1 x_{HR}^2 + r_{HR}^2 x_{HR}^1)}{\zeta_1 r_{HR}^2 + \zeta_2 r_{HR}^1 + i(\zeta_1 x_{HR}^2 + \zeta_2 x_{HR}^1)} \\
&= \frac{1}{(\zeta_1 r_{HR}^2 + \zeta_2 r_{HR}^1)^2 + (\zeta_1 x_{HR}^2 + \zeta_2 x_{HR}^1)^2} \left\{ \begin{aligned} & (r_{HR}^1 r_{HR}^2 - x_{HR}^1 x_{HR}^2)(\zeta_1 r_{HR}^2 + \zeta_2 r_{HR}^1) + \\ & (r_{HR}^1 x_{HR}^2 + r_{HR}^2 x_{HR}^1)(\zeta_1 x_{HR}^2 + \zeta_2 x_{HR}^1) + \\ & i \left[(r_{HR}^1 x_{HR}^2 + r_{HR}^2 x_{HR}^1)(\zeta_1 r_{HR}^2 + \zeta_2 r_{HR}^1) - \right. \\ & \left. (r_{HR}^1 r_{HR}^2 - x_{HR}^1 x_{HR}^2)(\zeta_1 x_{HR}^2 + \zeta_2 x_{HR}^1) \right] \end{aligned} \right\} \quad (5.50)
\end{aligned}$$

The average surface resistance and reactance are now given from Eq. (5.50) as

$$\begin{aligned}
r_{surf}^{avg} &= \frac{(r_{HR}^1 r_{HR}^2 - x_{HR}^1 x_{HR}^2)(\zeta_1 r_{HR}^2 + \zeta_2 r_{HR}^1) + (r_{HR}^1 x_{HR}^2 + r_{HR}^2 x_{HR}^1)(\zeta_1 x_{HR}^2 + \zeta_2 x_{HR}^1)}{(\zeta_1 r_{HR}^2 + \zeta_2 r_{HR}^1)^2 + (\zeta_1 x_{HR}^2 + \zeta_2 x_{HR}^1)^2} \\
&= \frac{\zeta_1 r_{HR}^1 |Z_{HR}^2|^2 + \zeta_2 r_{HR}^2 |Z_{HR}^1|^2}{|\zeta_1 Z_{HR}^2|^2 + |\zeta_2 Z_{HR}^1|^2 + 2\zeta_1 \zeta_2 (r_{HR}^1 r_{HR}^2 + x_{HR}^1 x_{HR}^2)} \quad (5.51a)
\end{aligned}$$

$$\begin{aligned}
x_{surf}^{avg} &= \frac{i \left[(r_{HR}^1 x_{HR}^2 + r_{HR}^2 x_{HR}^1)(\zeta_1 r_{HR}^2 + \zeta_2 r_{HR}^1) - (r_{HR}^1 r_{HR}^2 - x_{HR}^1 x_{HR}^2)(\zeta_1 x_{HR}^2 + \zeta_2 x_{HR}^1) \right]}{(\zeta_1 r_{HR}^2 + \zeta_2 r_{HR}^1)^2 + (\zeta_1 x_{HR}^2 + \zeta_2 x_{HR}^1)^2} \\
&= \frac{i (\zeta_1 x_{HR}^1 |Z_{HR}^2|^2 + \zeta_2 x_{HR}^2 |Z_{HR}^1|^2)}{|\zeta_1 Z_{HR}^2|^2 + |\zeta_2 Z_{HR}^1|^2 + 2\zeta_1 \zeta_2 (r_{HR}^1 r_{HR}^2 + x_{HR}^1 x_{HR}^2)} \quad (5.51b)
\end{aligned}$$

Comparing Eq. (5.51) and Eq. (5.49) gives the conditions for perfect absorption

$$\begin{cases} \zeta_1 x_{HR}^1 |Z_{HR}^2|^2 + \zeta_2 x_{HR}^2 |Z_{HR}^1|^2 = 0 \\ \zeta_1 r_{HR}^1 |Z_{HR}^2|^2 + \zeta_2 r_{HR}^2 |Z_{HR}^1|^2 = |\zeta_1 Z_{HR}^2|^2 + |\zeta_2 Z_{HR}^1|^2 + 2\zeta_1 \zeta_2 (r_{HR}^1 r_{HR}^2 + x_{HR}^1 x_{HR}^2) \end{cases} \quad (5.52)$$

Figure 5.11 shows the absorption spectrum of the sandwich panel consisting periodically arranged unit cells with two different HRs in each unit cell. The neck radius a_1 , two neck lengths (l_1 and l_2) and the cavity length are selected as 1 mm, 3.5 mm, and 30 mm, respectively. From Figure 5.11, the absorption coefficient of the panel design can be obtained

with different geometrical combinations. The perfect absorption can be achieved in a variety of geometrical arrangements and the bandwidth that is above 50% absorption can be roughly estimated. It is worth noting that by properly choosing geometry of the sandwich panel, the perfect or near perfect sound absorption appears at different frequencies.

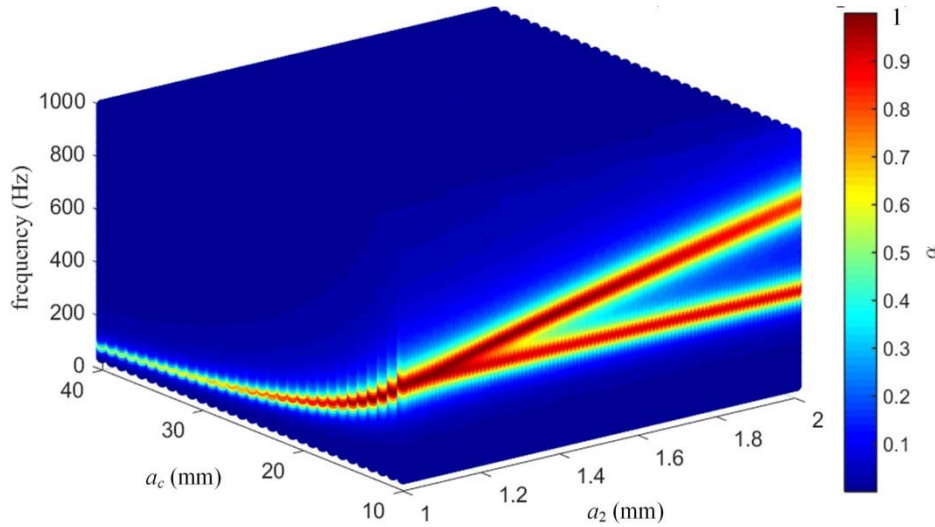


Figure 5.11 The absorption spectrum of the sandwich panel consisting periodical arrangement of dual HRs unit cells. The neck radius a_1 , neck lengths (l_1 and l_2) and the cavity length are selected as 1 mm, 3.5 mm, and 30 mm, respectively.

In order to further investigate absorption coefficient and the bandwidth with respect to the cavity radius and the neck radius respectively, by setting the cavity radius as 10 mm, 20 mm and 30 mm, the absorption coefficient with the variance of frequency and neck radius a_2 can be shown in Figure 5.12 (a) – (f). Similarly, if the neck radius a_2 is kept as constant as 1 mm, 1.25 mm and 1.4 mm, the frequency and absorption spectrum as a function of cavity radius shows in Figure 5.13 (a) – (f).

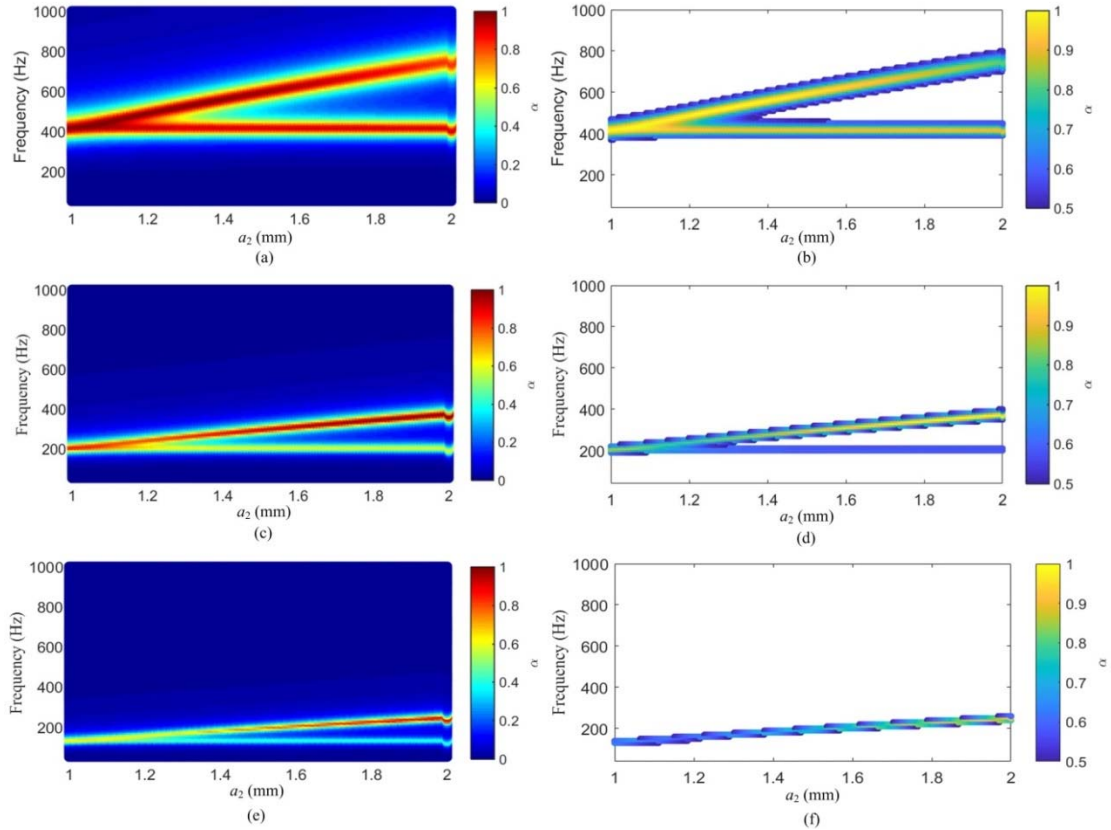


Figure 5.12 Absorption coefficient with the variance of frequency and neck radius a_2 with the neck radius a_1 , neck length l and cavity length are 1mm, 3.5 mm, and 30 mm, respectively: (a) The cavity radius is 10 mm; (c) The cavity radius is 20 mm; (e) The cavity radius is 30 mm; (b), (d) and (f) The corresponding ‘half-absorption’ spectrum.

The neck radius a_1 , two neck lengths (l_1 and l_2) and the cavity length are selected as 1 mm, 3.5 mm, and 30 mm, respectively. Figure 5.12 (b), (d) and (f) and Figure 5.13 (b), (d) and (f) provide the ‘half-absorption’ spectrums in which the absorption coefficients are greater than 0.5. From Figure 5.12, the frequencies and the corresponding bandwidths decrease as the cavity radiuses increase. For smaller cavity radius, the perfect or near perfect

sound absorption can be achieved under two frequencies when the neck radius a_2 is above some specific value. However, as the cavity radius get larger, the perfect or near perfect sound absorption only appears at one frequency and the corresponding bandwidth merges together above the ‘half-absorption’. For the other case, the absorption spectrum shows opposite trend and deviated into two branches as the neck radius a_2 increases shown from Figure 5.13.

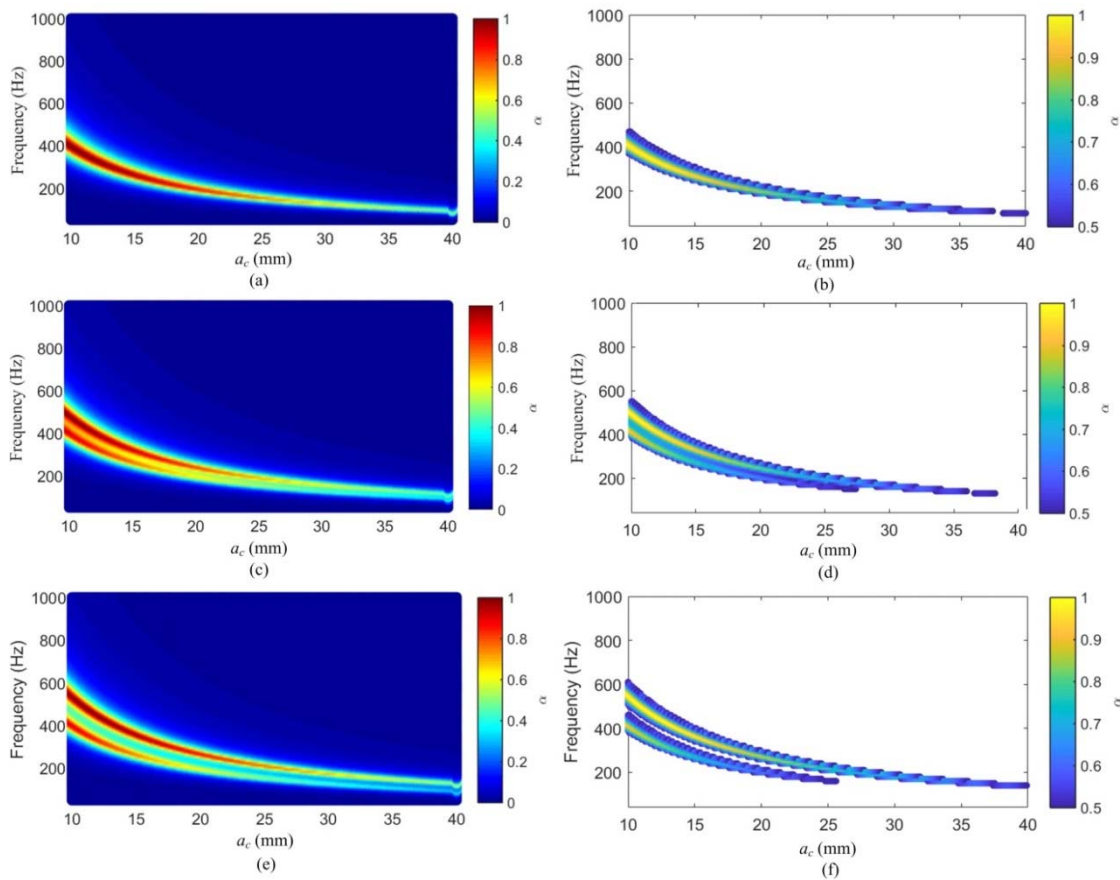


Figure 5.13 Absorption spectrum with the variance of frequency and cavity radius a_c with the neck radius a_1 , neck length l and cavity length l_c are 1mm, 3.5 mm, and 30 mm, respectively: (a) The neck radius a_2 is 1 mm; (c) The neck radius a_2 is 1.2 mm; (e) The neck radius a_2 is 1.4 mm; (b), (d) and (f) The corresponding ‘half-absorption’ spectrum.

Figure 5.14 present the absorption spectrum as a function of neck radius a_2 and cavity radius a_c at 300 Hz, 400 Hz, 500 Hz and 600 Hz, respectively. The neck radius a_1 , two neck lengths (l_1 and l_2) and the cavity length are selected as 1 mm, 3.5 mm, and 30 mm, respectively. The blue dotted line in each figure is where the perfect absorption located. From those figures, the design parameters for perfect absorption sandwich panel can be selected at target frequencies. The flexibility of designing perfect absorption sandwich panel varies with the change of frequencies.

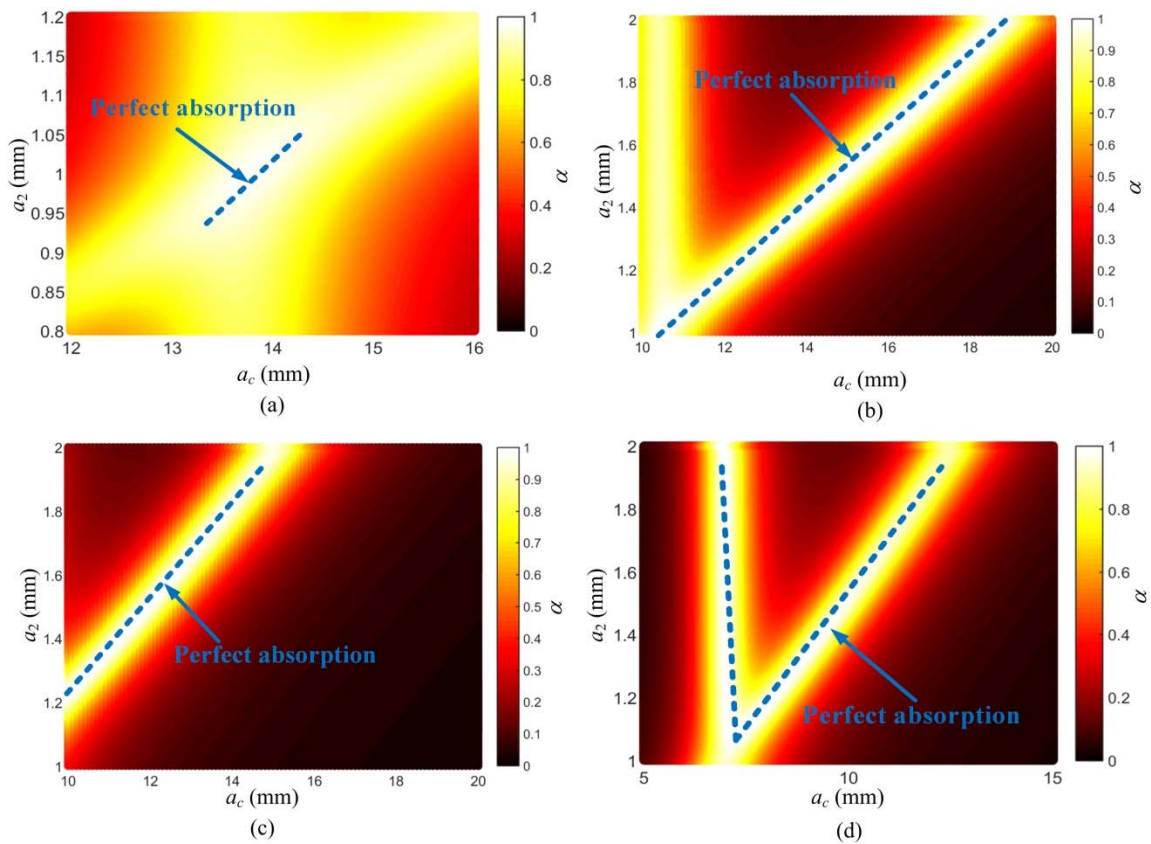


Figure 5.14 Absorption spectrum as a function of neck radius a_2 and cavity radius a_c : (a)

300 Hz; (b) 400 Hz; (c) 500 Hz; (d) 600 Hz.

To further investigate the bandwidth of the sound absorber sandwich panel, the neck radius a_2 is chosen as a variable with 1.1 mm, 1.2 mm, 1.3 mm and 1.45 mm while other parameters are kept constant. Figure 5.15 show the absorption coefficient of the sandwich panel with different neck radius a_2 . The ‘half-absorption’ bandwidth increases as the neck radius increases.

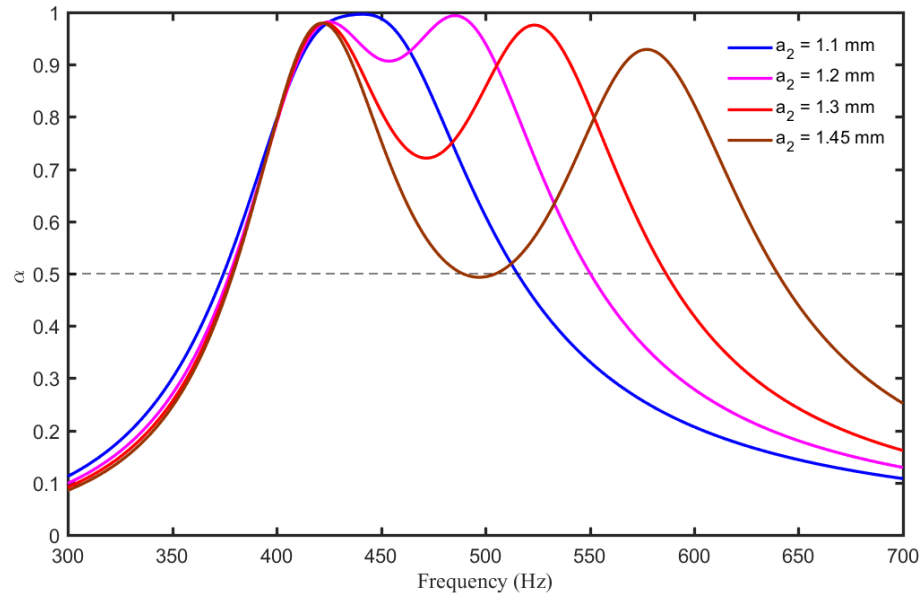


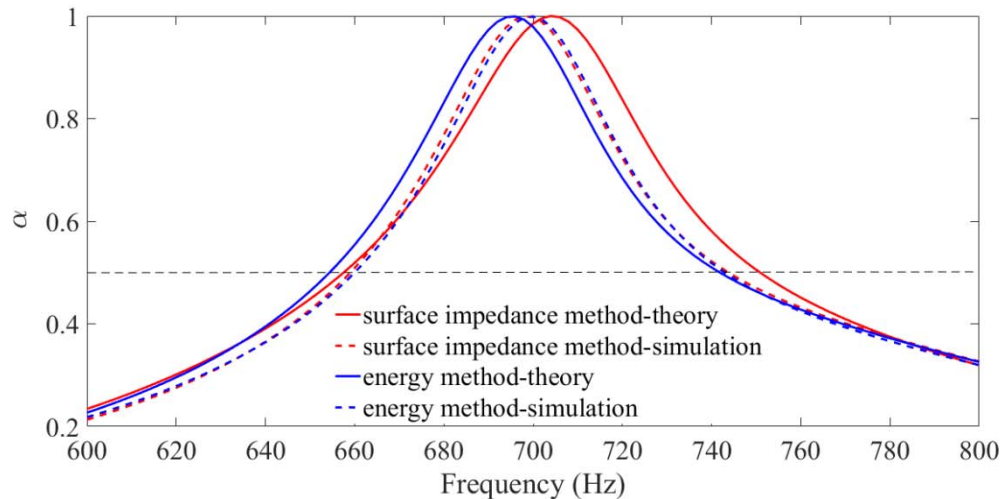
Figure 5.15 Absorption coefficient of the sandwich panel with different neck radius a_2

5.2.4 Finite element simulation for numerical analysis

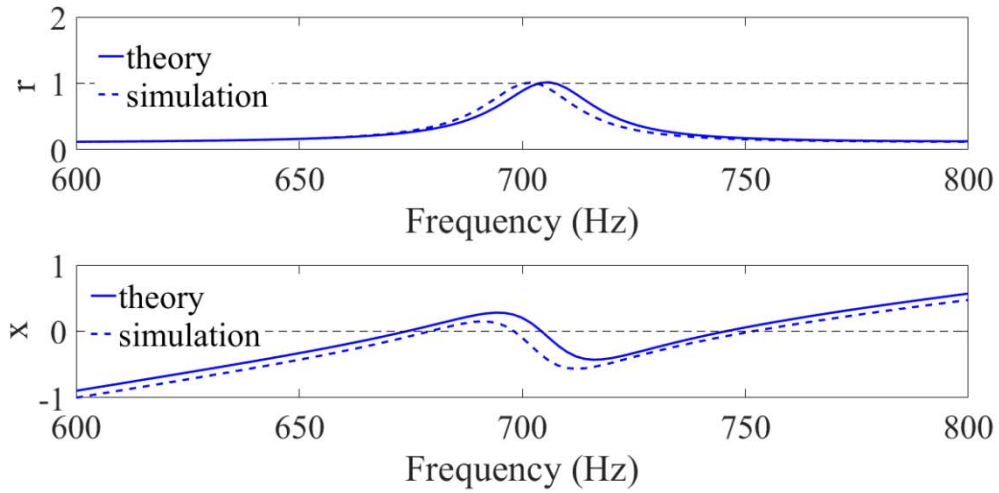
Thermoacoustic module in Comsol Multiphysics 5.2a is utilized for finite element analysis. In the numerical simulations, the perfect sound absorber sandwich panels are categorized into three typical kinds and designed to study the coupling between the HRs in the unit cell. For each case, the absorption coefficient and the impedance of the perfect absorber sandwich panel are analyzed and the corresponding theoretical and numerical

results are compared. The theories of energy method and impedance method in solving the absorption coefficient are also compared with the numerical results. The dissipated energy power that is totally absorbed by the absorber sandwich panel can be obtained by simulation.

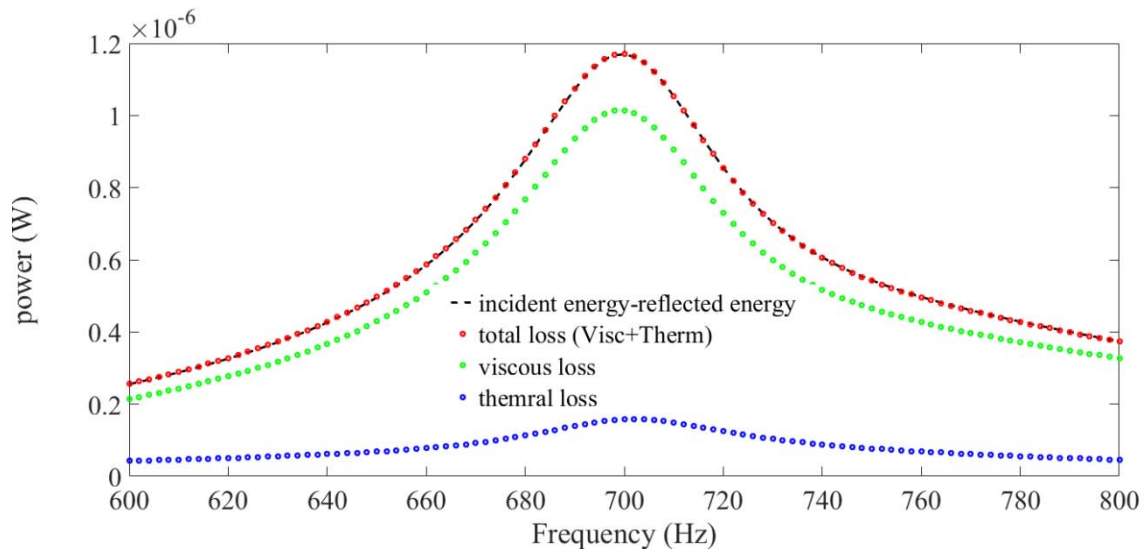
In the absorption coefficient plot shown in Figure 5.16 (a), only one peak appears around 700 Hz which is neither the resonance frequency of HR1 (680 Hz) nor HR2 (750 Hz) in the unit cell. A new hybrid resonant mode comes out, which is clearly found in both resistance and reactance plots in Figure 5.16 (b). The difference between the theoretical based impedance method and the energy method is due to the inaccurate estimation of the end correction for each HR in the unit cell. In other words, the coupling between the two HRs is very strong which significantly impacts the actual value of end correction of each HR. The deviation of the numerical and theoretical results of both absorption coefficient and impedance is also attributed to the end correction. The energy balance is calculated in Figure 5.16 (c) to confirm the validity of the simulation.



(a)



(b)

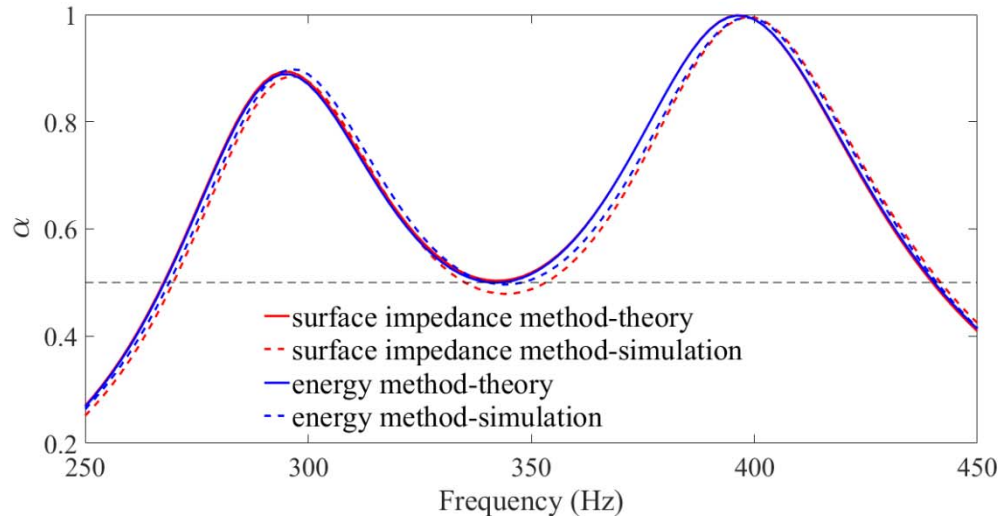


(c)

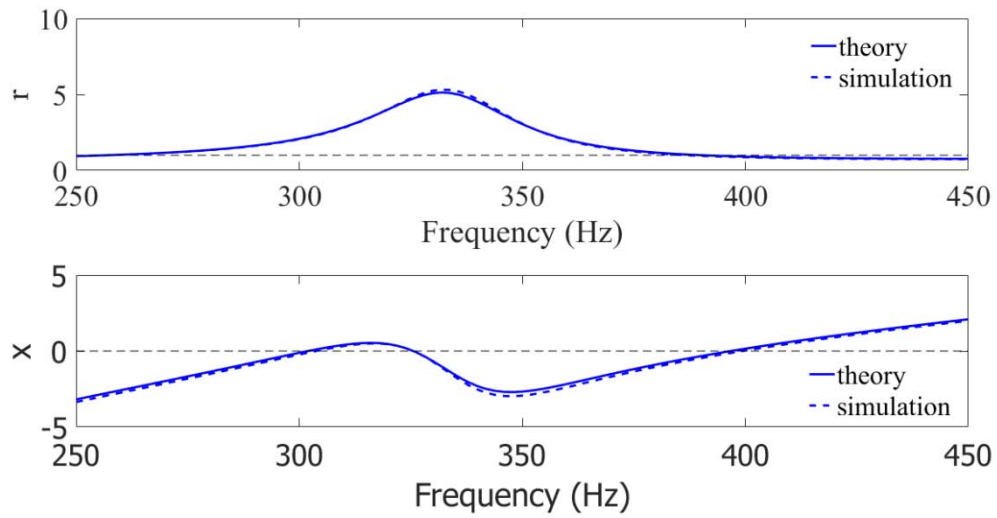
Figure 5.16 The perfect absorber sandwich panel I: (a) Absorption coefficient where $a_1=2.5$ mm, $a_2=2.85$ mm, $l=6$ mm, $l_{c1}=l_{c2}=40$ mm, $d=7$ mm, and the panel size is $l_x=44$ mm and $l_y=22$ mm; (b)The impedance with respect to the resistance and reactance
(c) Energy balance verification

In case I, the strong coupling appears between the two HR resonance frequency where a hybrid mode is generated and the perfect sound absorption is achieved. In the second design for perfect absorber sandwich panel II, the resonance frequencies for single periodic HRs of type 1 and type 2 are around 304 Hz and 400 Hz, which are obviously found at two peaks in sound absorption coefficient plot, shown in Figure 5.17 (a). However, it is noticed that there is another hybrid mode appears at 326 Hz between the two intrinsic resonance frequencies, where the absorption coefficient drops to 0.5 between 304 Hz and 400 Hz. The two resonance peaks are quite similar to the identical periodic HRs sandwich panel due to the weak interaction between the two HRs.

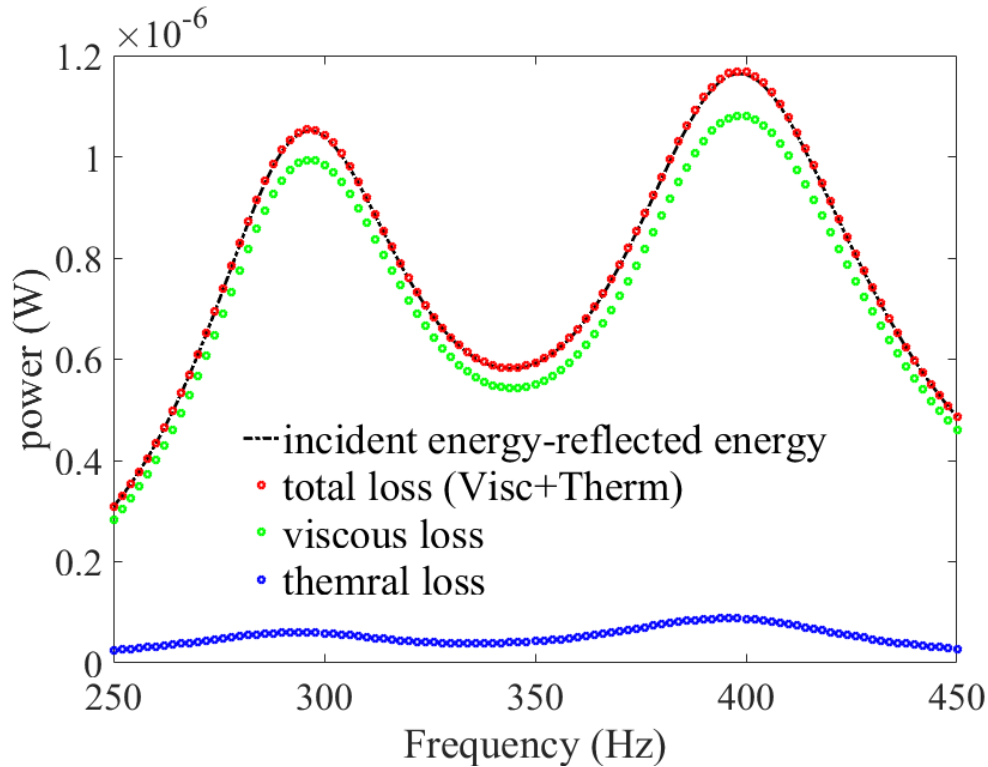
Theoretical predictions on sound absorption coefficient based on two methods and the impedance of the sandwich panel match perfectly with the numerical simulations, as shown in Figure 5.17 (a) and (b). The perfect match is attributed to the accurate estimation of the end correction of both types of HRs with $\frac{8a_1}{3\pi}$ and $\frac{8a_2}{3\pi}$, respectively and the accurate expression of the equivalent surface impedance. The accurate estimation of end correction that works well in such panel II is also result from the weak coupling between two HRs.



(a)



(b)



(c)

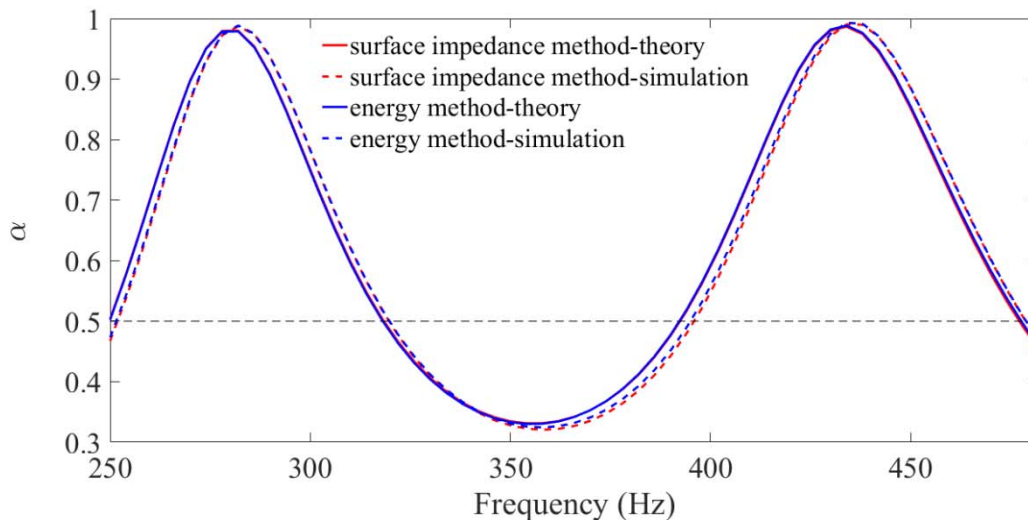
Figure 5.17 The perfect absorber sandwich panel II: (a) Absorption coefficient where $a_1=1$ mm, $a_2=1.38$ mm, $l=6$ mm, $l_{c1}=l_{c2}=10$ mm, $d=22$ mm, and the panel size is $l_x=44$ mm and $l_y=22$ mm; (b)The impedance with respect to the resistance and reactance
(c) Energy balance verification

At 304 Hz, the sandwich panel is dominated by the first resonate mode yielding by HR1 due to the negligible coupling from HR2. Although the reactance at 304 Hz goes to zero, the resistance at this frequency does not match the background. This is because the velocity is extremely larger around 304 Hz near the orifice of HR1 than that of HR2 and the velocity gradient in the boundary layer increases which causes a larger viscous dissipation. Similarly,

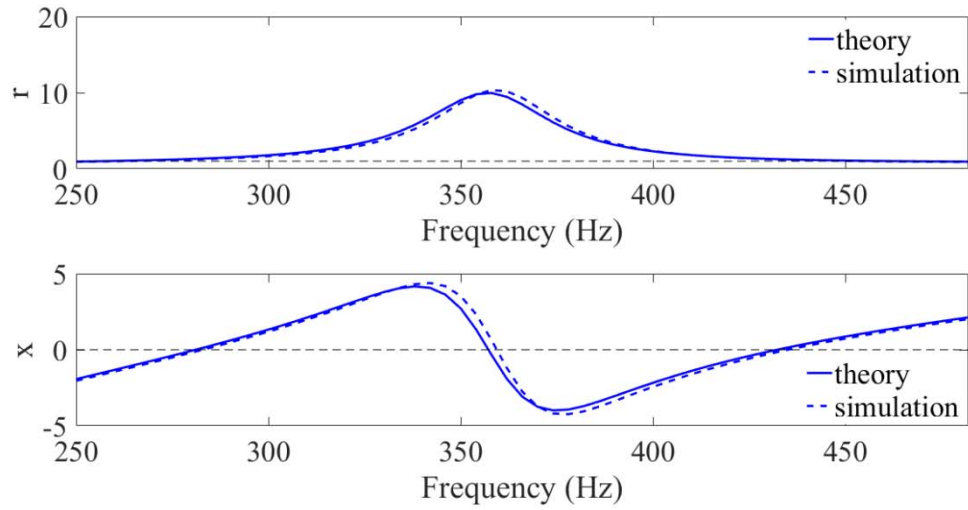
at resonance frequency near 400 Hz, only HR2 is excited and HR1 behaves like a rigid wall with almost zero velocity and little air flow through the orifice of the HR1. At this frequency, the impedance of the panel matches the background fluid, e.g., the reactance goes to zero and the corresponding resistance reaches to 1. Thus total sound absorption can be obtained at this frequency. However, at the frequency 326Hz between the two resonant frequencies, the mechanism is quite different from those at 304 Hz and 400 Hz which only one type of the HR is excited. At this frequency, both types of the HRs in the unit cell are excited with one HR compresses the air into the cavity while the other one inflates the air out of the cavity. Figure 5.17 (c) shows the energy balance of sandwich panel II.

In contrary to the hybrid mode at 700 Hz in sandwich panel I which generate a perfect absorption mode, the hybrid mode in sandwich panel II result in poor sound absorption. The resonant frequency discrepancy between two types of periodic HRs increases from 70 Hz for sandwich panel I to 96 Hz for sandwich panel II, e.g., the strong coupling between two HRs becomes weak as increasing the discrepancy of resonance frequencies. However, in both cases, the mechanisms are quite the same as one HR compresses the air while the other one inflates the air at the coupling mode. The perfect sound absorption performance at the hybrid mode in sandwich panel I is due to the large viscous loss in the HRs to dissipate all the input energy so that no propagating wave reflects from and the panel surface and forms a non-radiation bound surface mode which is discussed by Li et al. ^[149]. The hybrid mode in sandwich panel II is another type of hybrid resonance which brings in smaller absorption coefficient.

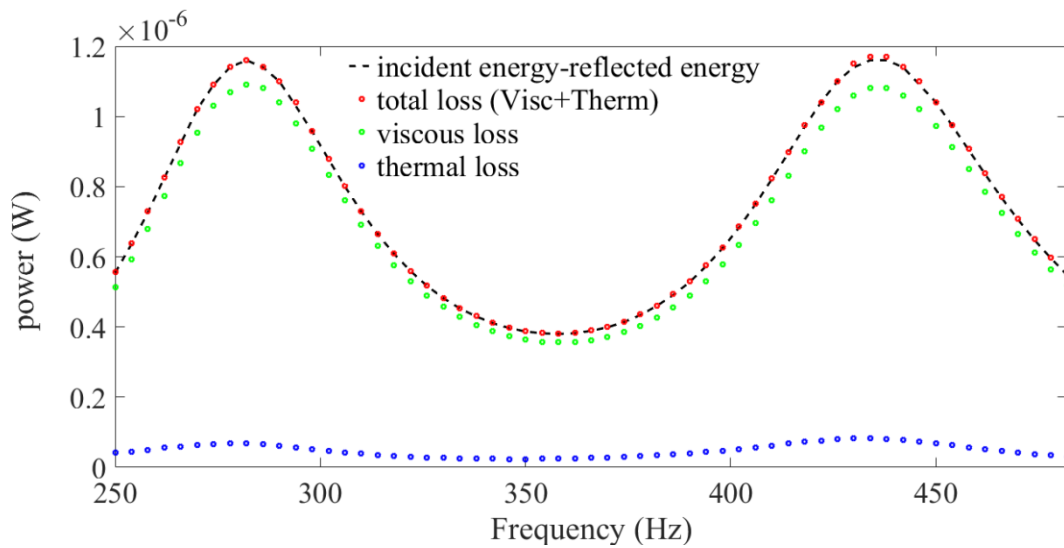
For perfect sound absorber sandwich panel III, there are also two absorption peaks in the absorption coefficient plot, shown in Figure 5.18 (a) and the absorption coefficient drops dramatically between two peaks. At frequencies close to 280 Hz and 430 Hz, the simulation results of the sandwich panel impedance in Figure 5.18 (b) match well with the theory results. This is because the fact that the difference between the resonant frequencies of single HR1 and HR2 are large and both HRs can be excited separately so that the estimation of the end corrections is accurate. The perfect sound absorption can be achieved at both resonances due the large viscous loss. Between the two resonant frequencies, the hybrid mode of the sandwich panel caused by coupling yields the inaccurate end correction. However, from the comparison between theoretical and numerical results, the discrepancy is very small and the theoretical model can still provide a good prediction on absorption coefficient.



(a)



(b)



(c)

Figure 5.18 The perfect absorber sandwich panel III: (a) Absorption coefficient where $a_1=1.1$ mm, $a_2=1.2$ mm, $l=5$ mm, $l_{c1}=l_{c2}=30$ mm, $d=22$ mm, and the panel size is $l_x=44$ mm and $l_y=22$ mm; (b)The impedance with respect to the resistance and reactance
(c) Energy balance verification

Compared with sandwich panel I and II, panel III has the largest value of resonant frequency discrepancy, which has the weakest coupling between the two HRs. At the resonance of each HR, panel III can achieve the perfect sound absorption respectively while only one of the HRs dominates the perfect sound absorption for panel II. The velocity gradient due to the two intrinsic resonance modes of two HRs results in larger viscous loss dissipation that enable them to absorb sound energy as much as possible. The bandwidth of the sound absorber sandwich panel can be tuned by carefully designing proper coupling mode. Therefore, by incorporating more HRs with proper coupling can induce a wider bandwidth at low frequencies.

5.3 Summary

In this chapter, two types of perfect sound absorber sandwich panels that can absorb sound in low frequency below 1000 Hz are designed and the sound pressure, acoustic impedance and velocity for the sandwich panel can be obtained to calculate the absorption coefficient by solving the Kirchhoff-Helmholtz integral. Two theoretical methods that are the average power flow method and the equivalent surface impedance method are used to predict the ability of sound absorption for the two types of sandwich panels. The perfect sound absorption can be achieved when the HRs are at resonance state and the surface impedance of the sandwich panel matches the air impedance. Based on the theory, the perfect sound absorber sandwich panel can be geometrically obtained. For the first type of sandwich panel which is composed of identical HRs, the total sound absorption can be achieved at peak frequency and the bandwidth mainly relies on the orifice radius. The bandwidth can achieve 59.95 Hz with approximated $1/62^{\text{th}}$ of the corresponding wavelength at 500 Hz and by

increasing the thickness of the sandwich panel, the bandwidth can be as large as 97.23 Hz with about $1/26^{\text{th}}$ of the wavelength. However for the other type of sandwich panel which is composed of dual HRs, three modes are analyzed due to the coupling effect. The theoretical results can be verified by the numerical results using finite element simulation, but it is still affected by the coupling. The bandwidth can be tuned by the coupling of more HRs. Therefore, the HRs based perfect sound absorber has an excellent sound absorptive performance at low frequency regime with deep sub-wavelength size.

Chapter 6

Conclusions and Future Work

6.1 Conclusions and Contributions beyond Previous Work

6.1.1 Conclusions

The following conclusions can be drawn from this dissertation

Two kinds of sound-proof sandwich panel are designed under the same mechanism-metamaterial. Both can reduce noise at low frequency regime with sub-wavelength size and an extremely low weight penalty. The two methods for such two panels on manipulating sound wave are based on wave propagation as sound impinges on the panel: The first kind of panel is devoted to less sound transmission loss if assuming putting a receiver on the other side of the panel; the other panel exerts on less or even no the sound reflection if assuming putting a receiver on the incident side of the panel. However, around the target frequency, both panels are at resonance state and impedance match between panel surface and the air at that frequency is critical for reducing sound in both cases. For sound absorber panel, not only the sound energy can totally absorbed, but it can achieve wideband attenuation. The configuration design is also more complicated but flexible.

The following conclusions can be drawn from each sandwich panel design:

- Honeycomb acoustic metamaterial design
1. A lightweight yet sound-proof honeycomb acoustic metamaterial is designed, theoretically proven and experimentally demonstrated. The use of no-mass-attached membrane-type acoustic metamaterials leads to excellent acoustic performance with minimum weight-penalty.
 2. The proposed metamaterials focus on the core structure design but can be used to build the core material of the sandwich panels which are experimentally verified to be significantly more sound-proof particularly at low frequencies with little add-on mass.
 3. The proposed metamaterial process simultaneously strong, lightweight and sound-proof as constructing structures.

4. The glass fiber can be inserted into the honeycomb acoustic metamaterial and can improve the acoustic performance at high frequencies.
 - The Helmholtz resonators based perfect sound absorber sandwich panel design
1. The Helmholtz resonators based perfect sound absorber sandwich panel is theoretically designed under two theories and numerically proved. The induced Helmholtz resonators don't apply any mass on the panel and can absorb sound energy by thermal-viscous friction between the orifice and the air particles.
2. Analyzing the radiation property of the sandwich panel, which is the most important theory to understand the mechanism of sound absorption, is derived by Kirchhoff-Helmholtz integral with respect to the Green's function.
3. The perfect sound absorption of identical appears at one frequency peak due to a single type of Helmholtz resonator with only one resonance. The bandwidth can be tuned by geometrical parameters such as the orifice radius, panel thickness etc.
4. A new hybrid mode is generated between the resonance frequencies of two Helmholtz resonators with different orifice radius in the sandwich panel because the coupling induces the inaccurate estimation of end correction. The strong coupling can achieve one total absorption peak while it drops gradually as the coupling becomes weaker by gradually increasing the discrepancy between two Helmholtz resonator resonance frequencies.
5. At the weaker coupling state, two Helmholtz resonators are excited on their own resonance where two perfect or near perfect absorption peaks appear. The wide bandwidth can be accomplished by sacrificing the absorption dip between two peak frequencies.

6.1.2 Future work

To further explore sound-proof sandwich panel design via metamaterial concept, based on the present dissertation work, some recommendations are proposed for future investigation:

1. Incorporate the proposed honeycomb type acoustic membrane metamaterial with other sound absorbing techniques, to realize a sound-proofing honeycomb panel in large scale which can be used in practical transportation applications.
2. Optimize the unit cell design by using multiple Helmholtz resonators, e.g., 4 HRs, 6 HRs, and 9 HRs etc., to further investigate the sound absorbing capabilities of the sandwich panel at low frequencies and its bandwidth.
3. Propose a theoretical model that can describe the end corrections accurately when coupling getting stronger among different HRs.
4. Further investigate the physical mechanisms that causes the hybrid modes with strong or weak couplings among HRs.
5. Combine the acoustic metamaterial with the Helmholtz based sandwich panels, to study the sound-proof competency of the sandwich panels at low frequencies.
6. Extend the current Helmholtz based sandwich panel to the honeycomb type sandwich panel and investigate the sound absorbing property of a honeycomb type sandwich panel and study its feasibility for low frequency noise control in transportation applications.

REFERENCES

- [1] Zheng, X., Lee, H., Weisgraber, T. H., Shusteff, M., DeOtte, J., Duoss, E. B., ... & Kucheyev, S. O. (2014). Ultralight, ultrastiff mechanical metamaterials. *Science*, 344(6190), 1373-1377.
- [2] Meza, L. R., Das, S., & Greer, J. R. (2014). Strong, lightweight, and recoverable three-dimensional ceramic nanolattices. *Science*, 345(6202), 1322-1326.
- [3] Kinsler, L. E., Frey, A. R., Coppens, A. B., & Sanders, J. V. (1999). Fundamentals of acoustics. *Fundamentals of Acoustics, 4th Edition, by Lawrence E. Kinsler, Austin R. Frey, Alan B. Coppens, James V. Sanders, pp. 560. ISBN 0-471-84789-5. Wiley-VCH, December 1999., 560.*
- [4] He, M., & Hu, W. (2008). A study on composite honeycomb sandwich panel structure. *Materials & Design*, 29(3), 709-713.
- [5] Paik, J. K., Thayamballi, A. K., & Kim, G. S. (1999). The strength characteristics of aluminum honeycomb sandwich panels. *Thin-walled structures*, 35(3), 205-231.
- [6] Herrmann, A. S., Zahlen, P. C., & Zuardy, I. (2005). Sandwich structures technology in commercial aviation. In *Sandwich structures 7: Advancing with sandwich structures and materials* (pp. 13-26). Springer, Dordrecht.
- [7] Dongmei, W. (2009). Cushioning properties of multi-layer corrugated sandwich structures. *Journal of Sandwich Structures & Materials*, 11(1), 57-66.
- [8] Honeycomb, P. A. G. A. F. (2012). Plascore Inc. *Zeeland, USA.*
- [9] Gibbs, B. M., & Maluski, S. (2004). Airborne sound level difference between dwellings at low frequencies. *Building Acoustics*, 11(1), 61-78.
- [10] Tinnsten, M. (2000). Optimization of acoustic response—a numerical and experimental comparison. *Structural and Multidisciplinary Optimization*, 19(2), 122-129.
- [11] Denli, H., & Sun, J. Q. (2005). Minimization of acoustic radiation from composite sandwich structures. *Sandwich Structures 7: Advancing with Sandwich Structures and Materials*, 587-596.
- [12] Thamburaj, P., & Sun, J. Q. (2002). Optimization of anisotropic sandwich beams for higher sound transmission loss. *Journal of Sound and Vibration*, 254(1), 23-36.
- [13] Rajaram, S., Wang, T., & Nutt, S. (2006). Sound transmission loss of honeycomb sandwich panels. *Noise control engineering journal*, 54(2).
- [14] Ruzzene, M. (2004). Vibration and sound radiation of sandwich beams with honeycomb truss core. *Journal of sound and vibration*, 277(4), 741-763.
- [15] Denli, H., & Sun, J. Q. (2007). Structural-acoustic optimization of sandwich structures with cellular cores for minimum sound radiation. *Journal of Sound and Vibration*, 301(1), 93-105.
- [16] Wen-chao, H., & Chung-fai, N. (1998). Sound insulation improvement using honeycomb

- sandwich panels. *Applied Acoustics*, 53(1-3), 163-177.
- [17] Ng, C. F., & Hui, C. K. (2008). Low frequency sound insulation using stiffness control with honeycomb panels. *Applied Acoustics*, 69(4), 293-301.
- [18] Makris, S. E., Dym, C. L., & Smith, J. M. (1986). Transmission loss optimization in acoustic sandwich panels. *The Journal of the Acoustical Society of America*, 79(6), 1833-1843.
- [19] Bolton, J. S., Shiau, N. M., & Kang, Y. J. (1996). Sound transmission through multi-panel structures lined with elastic porous materials. *Journal of sound and vibration*, 191(3), 317-347.
- [20] Wang, J., Lu, T. J., Woodhouse, J., Langley, R. S., & Evans, J. (2005). Sound transmission through lightweight double-leaf partitions: theoretical modelling. *Journal of sound and vibration*, 286(4), 817-847.
- [21] Palumbo, D., & Klos, J. (2011). The effects of voids and recesses on the transmission loss of honeycomb sandwich panels. *Noise Control Engineering Journal*, 59(6), 631-640.
- [22] Kidner, M. R. F., Fuller, C. R., & Gardner, B. (2006). Increase in transmission loss of single panels by addition of mass inclusions to a poro-elastic layer: Experimental investigation. *Journal of Sound and Vibration*, 294(3), 466-472.
- [23] Zhou, R., & Crocker, M. J. (2010). Sound transmission loss of foam-filled honeycomb sandwich panels using statistical energy analysis and theoretical and measured dynamic properties. *Journal of Sound and Vibration*, 329(6), 673-686.
- [24] Palumbo, D. L., & Klos, J. (2010). Quiet honeycomb panels.
- [25] Ramanathan, S. K. (2012). *Sound transmission properties of honeycomb panels and double-walled structures* (Doctoral dissertation, KTH Royal Institute of Technology).
- [26] Pedersen, P. C., Tretiak, O., & He, P. (1982). Impedance - matching properties of an inhomogeneous matching layer with continuously changing acoustic impedance. *The Journal of the Acoustical Society of America*, 72(2), 327-336.
- [27] Godin, O. A. (2008). Low-frequency sound transmission through a gas-liquid interface. *The Journal of the Acoustical Society of America*, 123(4), 1866-1879.
- [28] Kim, S. M., & Brennan, M. J. (1999). A compact matrix formulation using the impedance and mobility approach for the analysis of structural-acoustic systems. *Journal of Sound and Vibration*, 223(1), 97-113.
- [29] Raju, P. K., & Crocker, M. J. (1985). Prediction of sound transmission through double - walled systems containing helium. *The Journal of the Acoustical Society of America*, 78(S1), S59-S59.
- [30] Mohanty, A. K., Oliver, C. C., & Purdy, K. R. (1975). Acoustic measurements in low-density gases. *Journal of Physics D: Applied Physics*, 8(10), 1198.
- [31] Peters, P. R., Rajaram, S., & Nutt, S. (2006). Sound transmission loss of damped honeycomb sandwich panels. *InterNoise06*.

- [32] Naify, C. J., Huang, C., Sneddon, M., & Nutt, S. (2011). Transmission loss of honeycomb sandwich structures with attached gas layers. *Applied Acoustics*, 72(2), 71-77.
- [33] Naify, C., Sneddon, M., & Nutt, S. (2009, October). Noise Reduction of honeycomb sandwich panels with acoustic mesh caps. In *Proceedings of Meetings on Acoustics 158ASA* (Vol. 8, No. 1, p. 065002). ASA.
- [34] Herrin, D. W., Hua, X., & Liu, J. MICROPERFORATED PANEL ABSORBER DESIGN: A TUTORIAL.
- [35] Maa, D. Y. (1998). Potential of microperforated panel absorber. *the Journal of the Acoustical Society of America*, 104(5), 2861-2866.
- [36] Jung, S. S., Kim, Y. T., Lee, D. H., Kim, H. C., Cho, S. I., & Lee, J. K. (2007). Sound absorption of micro-perforated panel. *Journal-Korean Physical Society*, 50(4), 1044.
- [37] Zhao, X. D., Yu, Y. J., & Wu, Y. J. (2016). Improving low-frequency sound absorption of micro-perforated panel absorbers by using mechanical impedance plate combined with Helmholtz resonators. *Applied Acoustics*, 114, 92-98.
- [38] Dah-You, M. A. A. (1975). Theory and design of microperforated panel sound-absorbing constructions. *Scientia Sinica*, 18(1), 55-71.
- [39] Maa, D. Y. (1984, December). Wide-band sound absorber based on microperforated panels. In *INTER-NOISE and NOISE-CON Congress and Conference Proceedings* (Vol. 1984, No. 3, pp. 415-420). Institute of Noise Control Engineering.
- [40] MAA, D. Y. (1987). Microperforated panel wideband absorber. *Noise control engineering journal*, 77-84.
- [41] Qian, Y. J., Kong, D. Y., Liu, S. M., Sun, S. M., & Zhao, Z. (2013). Investigation on micro-perforated panel absorber with ultra-micro perforations. *Applied Acoustics*, 74(7), 931-935.
- [42] Liu, J., & Herrin, D. W. (2010). Enhancing micro-perforated panel attenuation by partitioning the adjoining cavity. *Applied Acoustics*, 71(2), 120-127.
- [43] Fan, L., Chen, Z., Zhang, S. Y., Ding, J., Li, X. J., & Zhang, H. (2015). An acoustic metamaterial composed of multi-layer membrane-coated perforated plates for low-frequency sound insulation. *Applied Physics Letters*, 106(15), 151908.
- [44] Zhao, X., & Fan, X. (2015). Enhancing low frequency sound absorption of micro-perforated panel absorbers by using mechanical impedance plates. *Applied Acoustics*, 88, 123-128.
- [45] Gai, X. L., Xing, T., Li, X. H., Zhang, B., & Wang, W. J. (2016). Sound absorption of microperforated panel mounted with helmholtz resonators. *Applied Acoustics*, 114, 260-265.
- [46] Park, S. H. (2013). Acoustic properties of micro-perforated panel absorbers backed by Helmholtz resonators for the improvement of low-frequency sound absorption. *Journal*

of Sound and Vibration, 332(20), 4895-4911.

- [47] Regniez, M., Gautier, F., Pézerat, C., & Pelat, A. (2013). ACOUSTIC IMPEDANCE OF MICROPERFORATED HONEYCOMB PANELS.
- [48] Pan, J., Guo, J., & Ayres, C. (2005, November). Improvement of sound absorption of honeycomb panels. In *Proceedings of Acoustics* (p. 9).
- [49] Sakagami, K., Yamashita, I., Yairi, M., & Morimoto, M. (2010). Sound absorption characteristics of a honeycomb-backed microperforated panel absorber: Revised theory and experimental validation. *Noise Control Engineering Journal*, 58(2), 157-162.
- [50] Guo, J., & Pan, J. (2013). Turning honeycomb panels into sound absorbers. *ICSV20*, 15-21.
- [51] Tang, Y., Ren, S., Meng, H., Xin, F., Huang, L., Chen, T., ... & Lu, T. J. (2017). Hybrid acoustic metamaterial as super absorber for broadband low-frequency sound. *Scientific Reports*, 7, 43340.
- [52] Veselago, V. G. (1968). The electrodynamics of substances with simultaneously negative values of ϵ and μ . *Soviet physics uspekhi*, 10(4), 509.
- [53] Veselago, V. G. (1968). Electrodynamics of substances with simultaneously negative electrical and magnetic permeabilities. *Physics-Uspekhi*, 10(4), 504-509.
- [54] Pendry, J. B., Holden, A. J., Stewart, W. J., & Youngs, I. (1996). Extremely low frequency plasmons in metallic mesostructures. *Physical review letters*, 76(25), 4773.
- [55] Pendry, J. B., Holden, A. J., Robbins, D. J., & Stewart, W. J. (1999). Magnetism from conductors and enhanced nonlinear phenomena. *IEEE transactions on microwave theory and techniques*, 47(11), 2075-2084.
- [56] Smith, D. R., Padilla, W. J., Vier, D. C., Nemat-Nasser, S. C., & Schultz, S. (2000). Composite medium with simultaneously negative permeability and permittivity. *Physical review letters*, 84(18), 4184.
- [57] Liu, Z., Zhang, X., Mao, Y., Zhu, Y. Y., Yang, Z., Chan, C. T., & Sheng, P. (2000). Locally resonant sonic materials. *Science*, 289(5485), 1734-1736.
- [58] Martinezsala, R., Sancho, J., Sánchez, J. V., Gómez, V., Llinares, J., & Meseguer, F. (1995). Sound-attenuation by sculpture. *nature*, 378(6554), 241-241.
- [59] Sheng, P., Zhang, X. X., Liu, Z., & Chan, C. T. (2003). Locally resonant sonic materials. *Physica B: Condensed Matter*, 338(1), 201-205.
- [60] Ho, K. M., Yang, Z., Zhang, X. X., & Sheng, P. (2005). Measurements of sound transmission through panels of locally resonant materials between impedance tubes. *Applied acoustics*, 66(7), 751-765.
- [61] Li, J., & Chan, C. T. (2004). Double-negative acoustic metamaterial. *Physical Review E*, 70(5), 055602.
- [62] Wu, Y., Lai, Y., & Zhang, Z. Q. (2011). Elastic metamaterials with simultaneously negative effective shear modulus and mass density. *Physical review letters*, 107(10),

105506.

- [63] Ding, Y., Liu, Z., Qiu, C., & Shi, J. (2007). Metamaterial with simultaneously negative bulk modulus and mass density. *Physical review letters*, *99*(9), 093904.
- [64] Lu, M. H., Feng, L., & Chen, Y. F. (2009). Phononic crystals and acoustic metamaterials. *Materials Today*, *12*(12), 34-42.
- [65] Zhang, S., Yin, L., & Fang, N. (2009). Focusing ultrasound with an acoustic metamaterial network. *Physical review letters*, *102*(19), 194301.
- [66] Li, J., Fok, L., Yin, X., Bartal, G., & Zhang, X. (2009). *Experimental demonstration of an acoustic magnifying hyperlens*. CALIFORNIA UNIV BERKELEY NANOSCALE SCIENCE AND ENGINEERING CENTER.
- [67] Zheng, L. Y., Wu, Y., Ni, X., Chen, Z. G., Lu, M. H., & Chen, Y. F. (2014). Acoustic cloaking by a near-zero-index phononic crystal. *Applied Physics Letters*, *104*(16), 161904.
- [68] Garcia-Chocano, V. M., Graciá-Salgado, R., Torrent, D., Cervera, F., & Sánchez-Dehesa, J. (2012). Quasi-two-dimensional acoustic metamaterial with negative bulk modulus. *Physical Review B*, *85*(18), 184102.
- [69] Fleury, R., & Alù, A. (2013). Extraordinary sound transmission through density-near-zero ultranarrow channels. *Physical review letters*, *111*(5), 055501.
- [70] Jing, Y., Xu, J., & Fang, N. X. (2012). Numerical study of a near-zero-index acoustic metamaterial. *Physics Letters A*, *376*(45), 2834-2837.
- [71] Lee, S. H., Park, C. M., Seo, Y. M., Wang, Z. G., & Kim, C. K. (2009). Acoustic metamaterial with negative density. *Physics letters A*, *373*(48), 4464-4469.
- [72] Shen, C. (2016). Design of Acoustic Metamaterials and Metasurfaces.
- [73] Fang, N., Xi, D., Xu, J., Ambati, M., Srituravanich, W., Sun, C., & Zhang, X. (2006). Ultrasonic metamaterials with negative modulus. *Nature materials*, *5*(6), 452.
- [74] Lee, S. H., Park, C. M., Seo, Y. M., Wang, Z. G., & Kim, C. K. (2009). Acoustic metamaterial with negative modulus. *Journal of Physics: Condensed Matter*, *21*(17), 175704.
- [75] Yang, Z., Mei, J., Yang, M., Chan, N. H., & Sheng, P. (2008). Membrane-type acoustic metamaterial with negative dynamic mass. *Physical review letters*, *101*(20), 204301.
- [76] Yang, Z., Dai, H. M., Chan, N. H., Ma, G. C., & Sheng, P. (2010). Acoustic metamaterial panels for sound attenuation in the 50–1000 Hz regime. *Applied Physics Letters*, *96*(4), 041906.
- [77] Naify, C. J., Chang, C. M., McKnight, G., & Nutt, S. (2010). Transmission loss and dynamic response of membrane-type locally resonant acoustic metamaterials. *Journal of Applied Physics*, *108*(11), 114905.
- [78] Naify, C. J., Chang, C. M., McKnight, G., Scheulen, F., & Nutt, S. (2011). Membrane-type metamaterials: Transmission loss of multi-celled arrays. *Journal of applied*

- physics*, 109(10), 104902.
- [79] Naify, C. J., Chang, C. M., McKnight, G., & Nutt, S. (2011). Transmission loss of membrane-type acoustic metamaterials with coaxial ring masses. *Journal of Applied Physics*, 110(12), 124903.
- [80] Naify, C. J., Chang, C. M., McKnight, G., & Nutt, S. R. (2012). Scaling of membrane-type locally resonant acoustic metamaterial arrays. *The Journal of the Acoustical Society of America*, 132(4), 2784-2792.
- [81] Zhang, Y., Wen, J., Zhao, H., Yu, D., Cai, L., & Wen, X. (2013). Sound insulation property of membrane-type acoustic metamaterials carrying different masses at adjacent cells. *Journal of Applied Physics*, 114(6), 063515.
- [82] Zhang, Y., Wen, J., Xiao, Y., Wen, X., & Wang, J. (2012). Theoretical investigation of the sound attenuation of membrane-type acoustic metamaterials. *Physics Letters A*, 376(17), 1489-1494.
- [83] Tian, H., Wang, X., & Zhou, Y. H. (2014). Theoretical model and analytical approach for a circular membrane-ring structure of locally resonant acoustic metamaterial. *Applied Physics A*, 114(3), 985-990.
- [84] Chen, Y., Huang, G., Zhou, X., Hu, G., & Sun, C. T. (2014). Analytical coupled vibroacoustic modeling of membrane-type acoustic metamaterials: Membrane model. *The Journal of the Acoustical Society of America*, 136(3), 969-979.
- [85] Langfeldt, F., Gleine, W. V., & von Estorff, O. (2015). Analytical model for low-frequency transmission loss calculation of membranes loaded with arbitrarily shaped masses. *Journal of Sound and Vibration*, 349, 315-329.
- [86] Chen, Y., Huang, G., Zhou, X., Hu, G., & Sun, C. T. (2014). Analytical coupled vibroacoustic modeling of membrane-type acoustic metamaterials: Plate model. *The Journal of the Acoustical Society of America*, 136(6), 2926-2934.
- [87] Ma, F., Wu, J. H., Huang, M., Zhang, W., & Zhang, S. (2015). A purely flexible lightweight membrane-type acoustic metamaterial. *Journal of Physics D: Applied Physics*, 48(17), 175105.
- [88] Ma, G., Yang, M., Yang, Z., & Sheng, P. (2013). Low-frequency narrow-band acoustic filter with large orifice. *Applied Physics Letters*, 103(1), 011903.
- [89] Mei, J., Ma, G., Yang, M., Yang, Z., Wen, W., & Sheng, P. (2012). Dark acoustic metamaterials as super absorbers for low-frequency sound. *Nature communications*, 3, 756.
- [90] Yang, M., Li, Y., Meng, C., Fu, C., Mei, J., Yang, Z., & Sheng, P. (2015). Sound absorption by subwavelength membrane structures: A geometric perspective. *Comptes Rendus Mécanique*, 343(12), 635-644.
- [91] Yang, M., Meng, C., Fu, C., Li, Y., Yang, Z., & Sheng, P. (2015). Subwavelength total acoustic absorption with degenerate resonators. *Applied Physics Letters*, 107(10),

104104.

- [92] Ma, G., Yang, M., Xiao, S., Yang, Z., & Sheng, P. (2014). Acoustic metasurface with hybrid resonances. *Nature materials*, 13(9), 873.
- [93] Huang, T. Y., Shen, C., & Jing, Y. (2016). Membrane-and plate-type acoustic metamaterials. *The Journal of the Acoustical Society of America*, 139(6), 3240-3250.
- [94] Jiang, P., Wang, X. P., Chen, T. N., & Zhu, J. (2015). Band gap and defect state engineering in a multi-stub phononic crystal plate. *Journal of Applied Physics*, 117(15), 154301.
- [95] Badreddine Assouar, M., Senesi, M., Oudich, M., Ruzzene, M., & Hou, Z. (2012). Broadband plate-type acoustic metamaterial for low-frequency sound attenuation. *Applied Physics Letters*, 101(17), 173505.
- [96] Oudich, M., Djafari-Rouhani, B., Pennec, Y., Assouar, M. B., & Bonello, B. (2014). Negative effective mass density of acoustic metamaterial plate decorated with low frequency resonant pillars. *Journal of Applied Physics*, 116(18), 184504.
- [97] Xiao, Y., Wen, J., & Wen, X. (2012). Sound transmission loss of metamaterial-based thin plates with multiple subwavelength arrays of attached resonators. *Journal of Sound and Vibration*, 331(25), 5408-5423.
- [98] Oudich, M., Zhou, X., & Badreddine Assouar, M. (2014). General analytical approach for sound transmission loss analysis through a thick metamaterial plate. *Journal of Applied Physics*, 116(19), 193509.
- [99] Badreddine Assouar, M., & Oudich, M. (2012). Enlargement of a locally resonant sonic band gap by using double-sides stubbed phononic plates. *Applied Physics Letters*, 100(12), 123506.
- [100] Li, Y., Chen, T., Wang, X., Xi, Y., & Liang, Q. (2015). Enlargement of locally resonant sonic band gap by using composite plate-type acoustic metamaterial. *Physics Letters A*, 379(5), 412-416.
- [101] Huang, H. H., & Sun, C. T. (2009). Wave attenuation mechanism in an acoustic metamaterial with negative effective mass density. *New Journal of Physics*, 11(1), 013003.
- [102] Mei, J., Liu, Z., Wen, W., & Sheng, P. (2007). Effective dynamic mass density of composites. *Physical Review B*, 76(13), 134205.
- [103] Li, P., Yao, S., Zhou, X., Huang, G., & Hu, G. (2014). Effective medium theory of thin-plate acoustic metamaterials. *The Journal of the Acoustical Society of America*, 135(4), 1844-1852.
- [104] Zhou, X., & Hu, G. (2009). Analytic model of elastic metamaterials with local resonances. *Physical Review B*, 79(19), 195109.
- [105] Gusev, V. E., & Wright, O. B. (2014). Double-negative flexural acoustic metamaterial. *New Journal of Physics*, 16(12), 123053.

- [106] Liu, Z. Q., Zhang, H., Zhang, S. Y., & Fan, L. (2014). An acoustic dual filter in the audio frequencies with two local resonant systems. *Applied Physics Letters*, *105*(5), 053501.
- [107] Mahesh, N. R., & Nair, P. (2014). Design and analysis of an acoustic demultiplexer exploiting negative density, negative bulk modulus and extra-ordinary transmission of membrane-based acoustic metamaterial. *Applied Physics A*, *116*(3), 1495-1500.
- [108] Fan, L., Chen, Z., Zhang, S. Y., Ding, J., Li, X. J., & Zhang, H. (2015). An acoustic metamaterial composed of multi-layer membrane-coated perforated plates for low-frequency sound insulation. *Applied Physics Letters*, *106*(15), 151908.
- [109] Cselyuszka, N., Sečujski, M., & Crnojević-Bengin, V. (2015). Novel negative mass density resonant metamaterial unit cell. *Physics Letters A*, *379*(1), 33-36.
- [110] Varanasi, S., Bolton, J. S., Siegmund, T. H., & Cipra, R. J. (2013). The low frequency performance of metamaterial barriers based on cellular structures. *Applied Acoustics*, *74*(4), 485-495.
- [111] Yao, S., Zhou, X., & Hu, G. (2010). Investigation of the negative-mass behaviors occurring below a cut-off frequency. *New Journal of Physics*, *12*(10), 103025.
- [112] Akl, W., Elsabbagh, A., & Baz, A. (2012). Acoustic metamaterials with circular sector cavities and programmable densities. *The Journal of the Acoustical Society of America*, *132*(4), 2857-2865.
- [113] Akl, W., & Baz, A. (2013). Active acoustic metamaterial with simultaneously programmable density and bulk modulus. *Journal of Vibration and Acoustics*, *135*(3), 031001.
- [114] Akl, W., & Baz, A. (2011). Stability analysis of active acoustic metamaterial with programmable bulk modulus. *Smart Materials and Structures*, *20*(12), 125010.
- [115] Mokry, P., Steiger, K., Vaclavik, J., Psota, P., Dolecek, R., Marton, P., ... & Cernik, M. (2014, October). Noise shielding using active acoustic metamaterials with electronically tunable acoustic impedance. In *INTER-NOISE and NOISE-CON Congress and Conference Proceedings* (Vol. 249, No. 2, pp. 5414-5422). Institute of Noise Control Engineering.
- [116] Zhang, H., Wen, J., Xiao, Y., Wang, G., & Wen, X. (2015). Sound transmission loss of metamaterial thin plates with periodic subwavelength arrays of shunted piezoelectric patches. *Journal of Sound and Vibration*, *343*, 104-120.
- [117] Yang, M., Meng, C., Fu, C., Li, Y., Yang, Z., & Sheng, P. (2015). Subwavelength total acoustic absorption with degenerate resonators. *Applied Physics Letters*, *107*(10), 104104.
- [118] Groby, J. P., Lagarrigue, C., Brouard, B., Dazel, O., Tournat, V., & Nennig, B. (2015). Enhancing the absorption properties of acoustic porous plates by periodically embedding Helmholtz resonators. *The Journal of the Acoustical Society of America*, *137*(1), 273-280.

- [119] Groby, J. P., Lagarrigue, C., Brouard, B., Dazel, O., Tournat, V., & Nennig, B. (2014). Using simple shape three-dimensional rigid inclusions to enhance porous layer absorption. *The Journal of the Acoustical Society of America*, 136(3), 1139-1148.
- [120] Chong, Y. D., Ge, L., Cao, H., & Stone, A. D. (2010). Coherent perfect absorbers: time-reversed lasers. *Physical review letters*, 105(5), 053901.
- [121] Wei, P., Croënne, C., Tak Chu, S., & Li, J. (2014). Symmetrical and anti-symmetrical coherent perfect absorption for acoustic waves. *Applied Physics Letters*, 104(12), 121902.
- [122] Merkel, A., Theocharis, G., Richoux, O., Romero-García, V., & Pagneux, V. (2015). Control of acoustic absorption in one-dimensional scattering by resonant scatterers. *Applied Physics Letters*, 107(24), 244102.
- [123] Cai, X., Guo, Q., Hu, G., & Yang, J. (2014). Ultrathin low-frequency sound absorbing panels based on coplanar spiral tubes or coplanar Helmholtz resonators. *Applied Physics Letters*, 105(12), 121901.
- [124] Li, Y., & Assouar, B. M. (2016). Acoustic metasurface-based perfect absorber with deep subwavelength thickness. *Applied Physics Letters*, 108(6), 063502.
- [125] Liang, Z., & Li, J. (2012). Extreme acoustic metamaterial by coiling up space. *Physical review letters*, 108(11), 114301.
- [126] Xie, Y., Popa, B. I., Zigoneanu, L., & Cummer, S. A. (2013). Measurement of a broadband negative index with space-coiling acoustic metamaterials. *Physical review letters*, 110(17), 175501.
- [127] Tang, K., Qiu, C., Ke, M., Lu, J., Ye, Y., & Liu, Z. (2014). Anomalous refraction of airborne sound through ultrathin metasurfaces. *Scientific reports*, 4.
- [128] Zhang, C., & Hu, X. (2016). Three-Dimensional Single-Port Labyrinthine Acoustic Metamaterial: Perfect Absorption with Large Bandwidth and Tunability. *Physical Review Applied*, 6(6), 064025.
- [129] Long, H., Cheng, Y., Tao, J., & Liu, X. (2017). Perfect absorption of low-frequency sound waves by critically coupled subwavelength resonant system. *Applied Physics Letters*, 110(2), 023502.
- [130] Starkey, T. A., Smith, J. D., Hibbins, A. P., Sambles, J. R., & Rance, H. J. (2017). Thin structured rigid body for acoustic absorption. *Applied Physics Letters*, 110(4), 041902.
- [131] Meissner, M. (2004). The response of Helmholtz resonator to external excitation. Part I: Acoustically induced resonance. *Archives of Acoustics*, 29(1).
- [132] Yu, G. (2009). *Acoustic resonators for noise control in enclosures: modelling, design and optimization* (Doctoral dissertation, The Hong Kong Polytechnic University).
- [133] Monkewitz, P. A., & Nguyen-Vo, N. M. (1985). The response of Helmholtz resonators to external excitation. Part 1. Single resonators. *Journal of Fluid Mechanics*, 151, 477-497.

- [134] Dickey, N. S., & Selamet, A. (1996). Helmholtz resonators: one-dimensional limit for small cavity length-to-diameter ratios.
- [135] Selamet, A., & Ji, Z. L. (2000). Circular asymmetric Helmholtz resonators. *The Journal of the Acoustical Society of America*, 107(5), 2360-2369.
- [136] Ingard, U. (1953). On the theory and design of acoustic resonators. *The Journal of the acoustical society of America*, 25(6), 1037-1061.
- [137] Chanaud, R. C. (1994). Effects of geometry on the resonance frequency of Helmholtz resonators. *Journal of Sound and Vibration*, 178(3), 337-348.
- [138] Cai, C., Mak, C. M., & Shi, X. (2017). An extended neck versus a spiral neck of the Helmholtz resonator. *Applied Acoustics*, 115, 74-80.
- [139] Dean, L. W. (1977, January). Increase in effectiveness of low frequency acoustic liners by use of coupled Helmholtz resonators. In *AIAA, Aerospace Sciences Meeting*.
- [140] Lu, J. H., Kuo, C. C., Hsiao, F. L., & Chen, C. C. (2012). Acoustic filter based on Helmholtz resonator array. *Applied Physics Letters*, 101(5), 051907.
- [141] Johansson, T. A., & Kleiner, M. (2001). Theory and experiments on the coupling of two Helmholtz resonators. *The Journal of the Acoustical Society of America*, 110(3), 1315-1328.
- [142] Kim, S., Kim, M. S., Kim, Y. H., & Kim, Y. W. (2003). Absorptive characteristics of resonator panel for low frequency noise control, and its applications. *한국소음진동공학회 국제학술발표논문집*, 3909-3916.
- [143] Kim, S. R., & Kim, Y. H. (2004, August). Broadband sound absorption by Helmholtz array panel; its physical phenomena and theory. In *INTER-NOISE and NOISE-CON Congress and Conference Proceedings* (Vol. 2004, No. 7, pp. 1100-1107). Institute of Noise Control Engineering.
- [144] Leroy, V., Strybulevych, A., Lanoy, M., Lemoult, F., Tourin, A., & Page, J. H. (2015). Superabsorption of acoustic waves with bubble metascreens. *Physical Review B*, 91(2), 020301.
- [145] Pritchard, R. L. (1960). Mutual acoustic impedance between radiators in an infinite rigid plane. *The Journal of the Acoustical Society of America*, 32(6), 730-737.
- [146] Lane, S. A., & Huybrechts, S. (2001). Coupled Helmholtz resonators for acoustic attenuation.
- [147] Jiménez, N., Huang, W., Romero-García, V., Pagneux, V., & Groby, J. P. (2016). Ultra-thin metamaterial for perfect and quasi-omnidirectional sound absorption. *Applied Physics Letters*, 109(12), 121902.
- [148] Jiménez, N., Romero-García, V., Pagneux, V., & Groby, J. P. (2017). Quasiperfect absorption by subwavelength acoustic panels in transmission using accumulation of resonances due to slow sound. *Physical Review B*, 95(1), 014205.
- [149] Li, J., Wang, W., Xie, Y., Popa, B. I., & Cummer, S. A. (2016). A sound absorbing

metasurface with coupled resonators. *Applied Physics Letters*, 109(9), 091908.